

AD-A184 754 DEFECT CHARACTERIZATION IN QUARTZ AND RELATED MATERIALS 1/2

(U) OKLAHOMA STATE UNIV STILLWATER DEPT OF PHYSICS

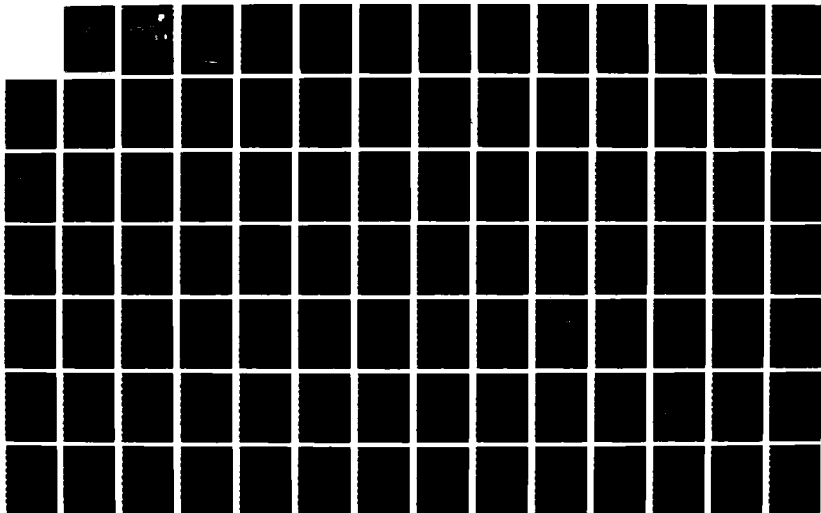
L E HALLIBURTON ET AL JUN 87 RADC-TR-87-66

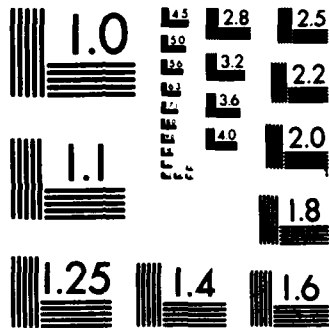
UNCLASSIFIED

F19628-83-K-0007

F/G 20/3

NL





MICROCOPY RESOLUTION TEST CHART  
NATIONAL BUREAU OF STANDARDS-1963-A

**TIC FILE COPY**

12

**AD-A184 754**

**RADC-TR-87-66**  
**Final Technical Report**  
**June 1987**



# **DEFECT CHARACTERIZATION IN QUARTZ AND RELATED MATERIALS**

**Oklahoma State University**

**DTIC**  
**ELECTE**  
**SEP 16 1987**  
**S D**

**Larry E. Halliburton, Joel J. Martin, William A. Sibley  
and Richard C. Powell**

**APPROVED FOR PUBLIC RELEASE; DISTRIBUTION UNLIMITED**

**AIR DEVELOPMENT CENTER**  
**Air Force Systems Command**  
**Griffiss Air Force Base, NY 13441-5700**

**87 9 16 002**

This report has been reviewed by the RADC Public Affairs Office (PA) and is releasable to the National Technical Information Service (NTIS). At NTIS it will be releasable to the general public, including foreign nations.

RADC TR-87-66 has been reviewed and is approved for publication.

APPROVED:



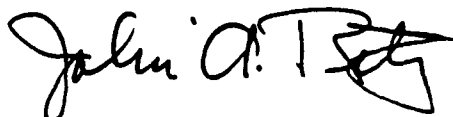
JOHN J. LARKIN  
Project Engineer

APPROVED:



HAROLD ROTH  
Director of Solid State Sciences

FOR THE COMMANDER:



JOHN A. RITZ  
Directorate of Plans and Programs

If your address has changed or if you wish to be removed from the RADC mailing list, or if the addressee is no longer employed by your organization, please notify RADC (ESM) Hanscom AFB, MA 01731-5000. This will assist us in maintaining a current mailing list.

Do not return copies of \_\_\_\_\_ tions or notices on a specific document require

## **DISCLAIMER NOTICE**

**THIS DOCUMENT IS BEST QUALITY PRACTICABLE. THE COPY FURNISHED TO DTIC CONTAINED A SIGNIFICANT NUMBER OF PAGES WHICH DO NOT REPRODUCE LEGIBLY.**

11-137 754

REPORT DOCUMENTATION PAGE

1a. REPORT SECURITY CLASSIFICATION UNCLASSIFIED		1b. RESTRICTIVE MARKINGS N/A	
2a. SECURITY CLASSIFICATION AUTHORITY N/A		3. DISTRIBUTION / AVAILABILITY OF REPORT Approved for public release; distribution unlimited.	
2b. DECLASSIFICATION / DOWNGRADING SCHEDULE N/A		4. PERFORMING ORGANIZATION REPORT NUMBER(S) N/A	
6a. NAME OF PERFORMING ORGANIZATION Oklahoma State University		6b. OFFICE SYMBOL (if applicable)	
6c. ADDRESS (City, State, and ZIP Code) Department of Physics Stillwater OK 74078		7a. NAME OF MONITORING ORGANIZATION Rome Air Development Center (ESM)	
7b. ADDRESS (City, State, and ZIP Code) Hanscom AFB MA 01731-5000		5. MONITORING ORGANIZATION REPORT NUMBER(S) RADC-TR-87-66	
8a. NAME OF FUNDING / SPONSORING ORGANIZATION Rome Air Development Center		8b. OFFICE SYMBOL (if applicable) ESM	
8c. ADDRESS (City, State, and ZIP Code) Hanscom AFB MA 01731-5000		9. PROCUREMENT INSTRUMENT IDENTIFICATION NUMBER F19628-83-K-0007	
10. SOURCE OF FUNDING NUMBERS		11. TITLE (include Security Classification) DEFECT CHARACTERIZATION IN QUARTZ AND RELATED MATERIALS	
PROGRAM ELEMENT NO 61102F		PROJECT NO 2306	
TASK NO JT		WORK UNIT ACCESSION NO. 42	
12. PERSONAL AUTHOR(S) Larry E. Halliburton, Joel J. Martin, William A. Sibley, Richard C. Powell			
13a. TYPE OF REPORT Final		13b. TIME COVERED FROM Apr 83 to Dec 83	
14. DATE OF REPORT (Year, Month, Day) June 1987		15. PAGE COUNT 142	
16. SUPPLEMENTARY NOTATION N/A			
17. COSATI CODES			18. SUBJECT TERMS (Continue on reverse if necessary and identify by block number) Interstitial alkalis Quartz Lithium
FIELD	GROUP	SUB-GROUP	
09	01		
19. ABSTRACT (Continue on reverse if necessary and identify by block number) The substitutional aluminum ions present in all quartz require charge compensation. In as-grown synthetic quartz, interstitial alkalis serve as the charge compensators. Irradiation at temperatures above 200-K replaces the alkali with either a proton or a hole trapped on an adjacent oxygen. Electrodiffusion (sweeping) can be used to replace the alkali with either a proton or another specific alkali. A study of the acoustic loss of a series of 5-MHz fifth overtone AT-cut resonator blanks as a function of sweeping and irradiation has been completed. No acoustic loss peaks were observed at temperatures less than 100°C which could be attributed to either the ALi or ALOH centers. Naswept samples showed the expected large loss peak at 53 K while unswept samples had only very small 53 K peaks. This result shows that in as-grown quartz, lithium is the primary charge compensating ion. Irradiation removed the 53 K peak and introduced new peaks at 23, 100 and 135 K. During anneal, these peaks were found to track with the AL-hole center. However, preliminary production study results show that the defect responsible for the 23 K peak grows in more slowly (Cont'd)			
20. DISTRIBUTION / AVAILABILITY OF ABSTRACT <input type="checkbox"/> UNCLASSIFIED/UNLIMITED <input checked="" type="checkbox"/> SAME AS RPT <input type="checkbox"/> DTIC USERS		21. ABSTRACT SECURITY CLASSIFICATION UNCLASSIFIED	
22a. NAME OF RESPONSIBLE INDIVIDUAL JOHN LARKIN		22b. TELEPHONE (include Area Code) (617) 478-5176	
		22c. OFFICE SYMBOL RADC (ESM)	

UNCLASSIFIED

19. (Cont'd). than the Al-hole center. The anneal study also showed that the decay of the Al-hole center is matched by the return of the alkali to the aluminum site.

Electrodifusion is a post-growth treatment which allows the selective exchange of charge compensating interstitial ions in quartz. This technique is employed commercially to enhance the radiation hardness of the material used for precision oscillator crystals. Most as-grown quartz contains substitutional aluminum with an interstitial alkali providing the charge compensation. Additional unidentified sites also trap protons to form the OH growth defects responsible for several IR absorption bands. When thermally released from their trapping sites, the interstitials can migrate along the large Z-axis channels. Therefore, if the sample is heated with an electric field applied along the Z direction, the ions can be swept out and replaced either by protons from the surrounding atmosphere or by the desired alkali from a salt electrode. To better understand electrodifusion, we are systematically investigating various aspects of the process. The apparent ionic conductivity data taken as the swept sample is slowly cooled usually show a curved  $\log(T)$  vs  $1000/T$  plot. The conductivity of  $H^+$  is much less than that of sodium or lithium. The activation energies at high temperatures tend to be lower than those found from the low temperature data. The exponential prefactors are considerably larger than the values predicted for a given aluminum content and reasonable estimates of the attack frequency and jump distance. Additional sources of mobile ions may be present. The peak or plateau observed during the warm-up period for air or hydrogen sweeping appears to be caused by the transition from conduction primarily by alkalis to conduction by protons.

UNCLASSIFIED

TABLE OF CONTENTS

I. DEFECT CHARACTERIZATION IN QUARTZ AND RELATED MATERIALS

	Page
A. INTRODUCTION AND SUMMARY .....	1
B. ALUMINUM-RELATED ACOUSTIC LOSS IN AT-CUT QUARTZ CRYSTALS .....	6
C. ELECTRODIFFUSION OF IONS IN ALPHA-QUARTZ.....	26
D. POINT DEFECTS IN NEUTRON IRRADIATED QUARTZ.....	41
E. OBSERVATION OF A SIMPLE LITHIUM-ASSOCIATED ELECTRON TRAP IN CRYSTALLINE SiO <sub>2</sub> .....	62
F. EVALUATION OF RADG GROWN MATERIAL.....	75
G. LIST OF PAPERS, PRESENTATIONS AND THESES.....	80

II. OPTICAL PROPERTIES OF FLUORIDE GLASS MATERIALS USEFUL FOR  
FIBERS AND LASER HOSTS

	Page
A. INTRODUCTION.....	82
B. HEAVY METAL FLUORIDE GLASSES.....	82
C. FRACTON LINEBROADENING IN DOPED GLASSES.....	101
D. FOUR-WAVE MIXING IN DOPED GLASSES.....	122

[References, Tables, and Figures are numbered separately for each section.]



# I. DEFECT CHARACTERIZATION IN QUARTZ AND RELATED MATERIALS

by

Larry E. Halliburton and Joel J. Martin

## A. INTRODUCTION AND SUMMARY

The structure of defects in alpha-quartz and in related materials continue to be of considerable interest. Alpha-quartz, which is piezoelectric, is used in a number of high technology applications such as precision oscillators, accelerometers and clocks where stability is a crucial operating criterion. However, a number of problems confront the systems designer when attempting to incorporate precision frequency control devices into operational units. For example, long term stability or aging can disable an entire system. Often of equal importance, quartz oscillators used in aerospace applications may be exposed to ionizing radiation which can cause frequency shifts and may alter the aging characteristics. Much of the radiation response and, possibly, the aging of quartz crystals is related to the defects produced during crystal growth or subsequent processing.

The main objectives of this project are to characterize defects in quartz crystals and in fluoride glasses, and to investigate the effects of various treatments, such as electrolysis and irradiation on these materials. This study is directed towards improving the performance of quartz oscillators and fluoride glass optical materials. The work on fluoride glasses is discussed in Part. II of this report.

The substitutional aluminum ions present in all quartz requires charge compensation, In as-grown synthetic quartz, interstitial alkalis serve as the charge compensators.

Irradiation at temperatures above 200 K replaces the alkali with either a proton or a hole trapped on an adjacent oxygen. Electrodiffusion (sweeping) can be used to replace the alkali with either a proton or another specific alkali. A study of the acoustic loss of a series of 5-MHz fifth overtone AT-cut resonator blanks as a function of sweeping and irradiation has been completed. No acoustic loss peaks were observed at temperatures less than 100°C which could be attributed to either the Al-Li or Al-OH centers. Na-swept samples showed the expected large loss peak at 53 K, while unswept samples had only very small 53 K peaks. This result shows that in as-grown quartz lithium is the primary charge compensating ion. Irradiation removed the 53 K peak and introduced new peaks at 23, 100 and 135 K. During anneal, these peaks were found to track with the Al-hole center. However, preliminary production study results show that the defect responsible for the 23 K peak grows in more slowly than the Al-hole center. The anneal study also showed that the decay of the Al-hole center is matched by the return of the alkali to the aluminum site.

Electrodiffusion is a post-growth treatment which allows the selective exchange of charge compensating interstitial ions in quartz. This technique is employed commercially to enhance the radiation hardness of the material used for precision oscillator crystals. Most as-grown quartz contains substitutional aluminum with an interstitial alkali providing the charge compensation. Additional unidentified sites also trap protons to form the OH<sup>-</sup> growth defects responsible for several IR absorption bands. When

thermally released from their trapping sites, the interstitials can migrate along the large Z-axis channels. Therefore, if the sample is heated with an electric field applied along the Z direction, the ions can be swept out and replaced either by protons from the surrounding atmosphere or by the desired alkali from a salt electrode. In order to better understand electrodiffusion, we are systematically investigating various aspects of the process. The apparent ionic conductivity data taken as the swept sample is slowly cooled usually shows a curved  $\log(\sigma)$  vs  $1000/T$  plot. The conductivity of  $H^+$  is much less than that of sodium or lithium. The activation energies at high temperatures tend to be lower than those found from the low temperature data. The exponential prefactors are considerably larger than the values predicted for a given aluminum content and reasonable estimates of the attack frequency and jump distance. Additional sources of mobile ions may be present. The peak or plateau observed during the warm-up period for air or hydrogen sweeping appears to be caused by the transition from conduction primarily by alkalis to conduction by protons.

Point defects formed by irradiation with fast neutrons have been characterized in high-quality quartz using spin resonance and optical absorption techniques. Among the paramagnetic defects generated are the  $E'_1$  center, the  $[AlO_4]^{\circ}$  center, and two previously unreported  $S=1$  centers. Production and thermal annealing characteristics of these more prominent defects are described. The two  $S=1$  defects have  $g_c$  values of 2.0205 and 2.0158 and thermally decay near 250 and 470°C respectively. They each consist of a pair of unpaired spins (i.e., holes) separated

oy approximately 5 Angstroms, and either vacancies or interstitials are a part of their models. These latter two centers, along with the  $E'_1$  centers, result from direct displacements during the neutron irradiation. An optical absorption band at 210 nm grows at the same rate as the  $E'_1$  and S=1 centers but cannot be definitely assigned to particular defects.

A defect consisting of an extra electron trapped at a four-coordinated silicon and stabilized by an adjacent interstitial lithium ion has been observed in quartz. It is formed by a double irradiation, first between 150 and 300 K to release the lithium ion from its associated  $Al^{3+}$  and then at 77 K to trap the electron at the free lithium ion. The c-axis ESR spectrum shows a splitting of 0.9 G from  $^7Li$  and 404.7 G from a  $^{29}Si$  (thus, the defect does not resemble a lithium atom). Pairs of these defects may be responsible for the lack of electronic paramagnetism in quartz after room temperature irradiation.

The mechanical Q of a series of quartz crystals grown for RADC by Motorola has been determined. We were supplied with unfinished AT-cut disks from a series of 6 stones and one additional set of disks from a stone that had been swept. These disks were sent out for fabrication into Warner design 5th overtone blanks. The lowest mechanical Q we observed was a value of  $1.2 \times 10^6$  at 5.67 MHz for blanks from stone GC9-21. The highest mechanical Q was  $2.32 \times 10^6$  at 5.63 MHz for blanks from GC24S which were the swept blanks. All of the finished blanks had frequencies above 5 MHz which means that their Q values will be somewhat lower than those for an actual 5 MHz blank. Low

temperature IR spectra were taken on one blank from each set; the spectra are included in this report. As expected samples with the higher mechanical Q also showed "cleaner" IR spectra.

Accession for	
NTIS CRAGI	<input checked="" type="checkbox"/>
DTIC TAB	<input type="checkbox"/>
Unannounced	<input type="checkbox"/>
Justification	
By	
Distribution/	
Availability Codes	
Dist	Avail and/or number
A-1	23

PROPERTY  
NOT RELECTED  
2

## B. ALUMINUM-RELATED ACOUSTIC LOSS IN AT-CUT QUARTZ CRYSTALS

### 1. Introduction

Alpha-quartz is used in a wide variety of precision electronic devices where aging and radiation-induced instabilities are undesirable. It is now well-known that quartz-controlled oscillators may exhibit transient and steady-state frequency and Q shifts when exposed to ionizing radiation.<sup>1-4</sup> Early results obtained by King<sup>5</sup> and other investigators<sup>6-9</sup> suggested that these effects were associated with the presence of impurities.

Substitutional  $\text{Al}^{3+}$  is present in all quartz<sup>10</sup> and requires charge compensation. Examples of such charge compensators are interstitial  $\text{Li}^+$  or  $\text{Na}^+$  ions, or holes or protons at an oxygen ion adjacent to the aluminum. The proton forms an  $\text{OH}^-$  molecule which is infrared active.<sup>10,11</sup> The  $\text{Al-Na}^+$  defect is responsible for the acoustic loss peak observed near 53 K in 5 MHz 5th overtone AT-cut crystals.<sup>12</sup> Irradiation at room temperature destroys the  $\text{Al-Na}^+$  centers;<sup>5,13</sup> this destruction being responsible for much of the steady state frequency offset. Recent work at Oklahoma State University has shown that the alkali ions become mobile under irradiation only if the temperature is greater than 200 K.<sup>13-15</sup> Following a room temperature irradiation, either a hole which can be observed by ESR techniques or a proton is found trapped on an oxygen adjacent to the  $\text{Al}^{3+}$ . The interstitial alkali ions are usually in the relatively large c-axis channels and at high temperatures can move along the channel under an applied electric field. King,<sup>5</sup> and later Kats<sup>11</sup> and Fraser,<sup>12</sup> used this technique to "sweep" hydrogen and specific alkalis into

the sample. Sweeping hydrogen in to replace the alkalis has been shown to improve the radiation hardness of quartz oscillators.<sup>8</sup>

The identification of both growth- and radiation-induced defects which affect the performance of quartz resonators is an important part of our project. Recently, using sweeping, IR absorption, and acoustic loss measurements, Martin and Doherty<sup>16</sup> reported that the Al-OH<sup>-</sup> center does not have an acoustic loss peak at temperatures below 370 K. They also reported that irradiation of both unswept and H<sub>2</sub>-swept Premium Q quartz resonator blanks produced acoustic loss peaks at 23 K and 100 K and a broad loss peak between 125 K and 165 K. King and Sander<sup>1</sup> had earlier reported the two higher temperature peaks and had suggested that they were caused by the Al-hole center. The 23 K peak had also been observed earlier and was attributed to changes in the interaction between the resonant vibrations of the blank and the thermal phonons.<sup>17</sup> We report here a comparison of the acoustic loss spectra of as-received and Li<sup>+</sup>, Na<sup>+</sup>, and H<sup>+</sup> swept resonators fabricated from the same bar of Premium Q grade quartz. We also report an isochronal anneal study of the three peaks induced by a room temperature irradiation which shows that they are associated with the Al-hole center. An isochronal anneal study was also made on an irradiated Na-swept resonator to directly compare the decay of the Al-hole and Al-OH<sup>-</sup> centers with the recovery of the Al-Na<sup>+</sup> centers.

## 2. Experimental Procedure

Samples for this study were cut from an unswept pure Z growth Sawyer Premium Q bar of cultured quartz that has been

given an in-house designation PQ-E. Samples from this bar have been extensively studied at Oklahoma State University using ESR,<sup>10,14</sup> IR, and acoustic loss techniques. All of these investigations show that the bar is of high quality but that it contains somewhat more aluminum (10-15 ppm) than the average Premium Q material (5-8 ppm). Consequently, aluminum-related effects are more readily observed. Confirming measurements were made on samples from a Toyo Supreme Q labeled bar SQ-B.

Five MHz 5th overtone AT-cut plano convex resonator blanks of the Warner design<sup>18</sup> were fabricated for this study by K&W Mfg., Prague, OK. The acoustic loss,  $Q^{-1}$ , of the resonator blanks was measured by the log decrement method from 5 to 300 K. The measurements were made in a variable temperature helium Dewar with the blanks mounted in a gap holder. The blank was driven for 10 to 40 ms at its series resonant frequency and then allowed to freely decay. The decaying rf signal was detected with a superheterodyne detector and displayed on a variable persistence storage oscilloscope. The exponential decay times were measured by using a digital timer gated by a window detector.

Electrolysis, or sweeping, was carried out at temperatures of 470-480°C in a controlled atmosphere system. This system allowed the use of H<sub>2</sub>, D<sub>2</sub>, or gettered-N<sub>2</sub> atmospheres, or a diffusion pumped vacuum. For the acoustic loss studies, the AT-cut resonator blanks were directly swept. Vapor-deposited Au electrodes were used. For the Li or Na sweeping runs, LiCl or NaCl was vapor deposited on the sample surface and then an Au electrode was deposited over the salt layer. The Li and Na sweeps were carried out in a vacuum better than  $5 \times 10^{-6}$  Torr.



Infrared absorption scans show that Al-OH<sup>-</sup> centers are present in the H<sup>2</sup>-swept sample but not in the alkali-swept samples.

### 3. Results and Discussion

Figure 1 compares the acoustic loss,  $Q^{-1}$ , spectra for unswept, Li-swept, and Na-swept PQ-E series resonator blanks. The unswept blank shows a small Al-Na<sup>+</sup> loss peak at 53 K with a height  $dQ^{-1}$  of approximately  $5 \times 10^{-7}$ . The Li sweep removed this peak and did not introduce any new peaks. The Na-swept blank showed a very large 53 K peak with  $\delta Q^{-1} = 2 \times 10^{-4}$  as shown in Figure 1. The results for the Toyo blanks were similar except that the unswept blank showed a 53 K Al-Na<sup>+</sup> peak with a height of  $\delta Q = 5 \times 10^{-5}$ . Since the material from which these blanks were fabricated contains 10 to 15 ppm aluminum, we conclude that the concentration, C, of Al-Na<sup>+</sup> centers is given by

$$C = [5(20\%) \times 10^4] \delta Q^{-1} \quad (1)$$

where C is in ppm and  $\delta Q^{-1}$  is the height of the 53 K Al-Na<sup>+</sup> loss peak. Thus, the unswept PQ-E blank probably contains about 0.3 ppm Al-Na<sup>+</sup> centers; the remaining 10 to 15 ppm of aluminum must be compensated by Li<sup>+</sup>. Since the mineralizer used in growing Premium Q quartz is predominantly Na<sub>2</sub>CO<sub>3</sub>, the essentially total exclusion of Na<sup>+</sup> from the aluminum sites by the addition of a small amount of Li<sub>2</sub>CO<sub>3</sub> to the solution is remarkable.<sup>19,20</sup> The as-grown Toyo Supreme Q blank contains substantial amounts of Na<sup>+</sup> but Li<sup>+</sup> must still be the majority charge compensator because the 53 K peak increased by a factor of four when the sample was Na-swept. An additional, much smaller, loss peak related to the Al-

$\text{Na}^+$  center was observed at approximately 135 K in the Na-swept blanks. Park and Nowick<sup>21</sup> have also observed two Na-related peaks in their dielectric loss measurements.

In contrast to earlier work<sup>12</sup> which reported a  $\text{Li}^+$  related loss peak near 105 K, the results shown in Fig. 1 for the Premium Q blanks and similar results for the Toyo samples show no evidence of a Al- $\text{Li}^+$  acoustic loss at temperatures below 100°C. Toulouse, Green and Nowick<sup>22</sup> have recently reported the absence of  $\text{Li}^+$  related dielectric loss peaks in both Sawyer Premium Q and Toyo Supreme Q samples. They suggest that because of the small size of the  $\text{Li}^+$  ion the double well  $\text{Na}^+$  sites have collapsed into a single well for the  $\text{Li}^+$ . The resulting Al- $\text{Li}^+$  pair then probably lies along the x-axis. Such a single well model would show neither acoustic nor dielectric loss peaks.

Figure 2 compares the acoustic loss spectra for the unswept, Li-swept, and H-swept blanks. The results for the Li and H-sweeps are essentially identical, as were the results for a D-sweep which have been omitted from Fig. 2 for clarity. Infrared absorption measurements made at liquid nitrogen temperature show that the H-swept blank contains 10-15 ppm Al- $\text{OH}^-$  centers. Thus, it appears that neither the Al- $\text{OH}^-$  or the Al- $\text{OD}^-$  centers show significant acoustic loss peaks at temperatures below about 370 K. It should be noted that at higher temperatures, the interstitial alkali ions become thermally liberated from the  $\text{Al}^{3+}$  trapping site and diffuse along the c-axis channels. This diffusion causes an acoustic loss which increases exponentially with temperature.<sup>17</sup> Lipson *et al.*<sup>23</sup> and Koehler<sup>24</sup> have shown

that this high temperature loss is not present in H-swept quartz which contains no alkali ions and, therefore, must be caused by the alkali diffusion. Infrared absorption studies of the Al-OH<sup>-</sup> center<sup>11,25</sup> show that it is strongly polarized with the electric dipole perpendicular to the c-axis. This orientation would probably not have a double well structure that would give rise to an acoustic loss.

Recently, Martin and Doherty<sup>16</sup> reported that irradiation of unswept and H<sub>2</sub>-swept PQ-E resonator blanks at room temperature produced loss peaks at 23 K and 100 K and a broad loss between 125 and 165 K. The peaks were much larger in the unswept material than in the H<sub>2</sub>-swept blank. The room temperature irradiation also removed the small Al-Na<sup>+</sup> loss peak which was present initially in the unswept blank. King and Sander<sup>1</sup> have previously observed the peak at 100 K and the broad loss between 125 K and 165 K. They attributed these loss peaks to the Al-hole center. Martin and Doherty suggested that the 23 K peak is also due to the Al-hole center. Martin *et al.*<sup>26</sup> were able to describe the broad loss as a single peak centered at about 135 K.

Figure 3 shows the acoustic loss,  $Q^{-1}$ , versus temperature spectrum for the Na-swept blank in the as-swept condition and after a room temperature irradiation. The irradiation has removed the large 53 K and 135 K Al-Na<sup>+</sup> loss peak while introducing the 23 K peak and the overlapping 100 K and 135 K peaks. The post-irradiation acoustic loss spectra for the unswept and Li-swept blanks are essentially the same as for the Na-swept sample. These three loss peaks are also observed in irradiated H-swept resonators fabricated from this same bar.

However, their strength is reduced by approximately a factor of five. An inspection of the results reported by Doherty *et al.*<sup>13</sup> for the acoustic loss of their Na-swept resonator D14-45DC shows that the 23 K peak is small but present in their results. D14-45 series quartz is Premium Q grade material with an aluminum content less than 1 ppm, so we would expect aluminum-related loss peaks to be much smaller. Their Na loss peak is about 0.035 times that of our Na-swept PQ-E resonator blank. It should also be noted that their resonator was partially H-swept. Thus, it appears that these three peaks, and the Na peak as well, scale with the aluminum content.

The thermal anneal behavior of the Al-hole and Al-OH<sup>-</sup> centers in unswept quartz has been studied by Jani, Bossoli and Halliburton<sup>27</sup> and by Sibley *et al.*,<sup>15</sup> respectively. The Al-hole centers, as observed by ESR techniques, anneal out slightly below 550 K while the Al-OH<sup>-</sup> center anneals out between 620 K and 670 K. If the three radiation-induced loss peaks are due to the Al-hole center, they should show the same annealing pattern as the Al-hole center ESR spectrum. We have carried out an isochronal anneal study on the unswept blank and on the Li-swept blank. The results for the unswept blank show that the 23 K, 100 K, and 135 K loss peaks all anneal out between 500 and 550 K, as shown in Fig. 4. A recent production study by Martin, Hwang and Bahadur<sup>28</sup> shows that the defect responsible for the 23 K loss peak grows in more slowly with radiation dose than either the Al-hole center or the Al-OH center. As expected, the decay of the Al-Na center with radiation dose nearly matches the production of the Al-hole and

Al-OH centers. Thus, while the defect responsible for the 23 K loss peak anneals with the Al-hole center it most likely is a different defect. At the present time we do not have production data on the smaller loss peaks at 100 K and 135 K. When the anneal of the unswept blank is continued to higher temperatures, the Al-Na<sup>+</sup> center loss peak recovers between 600 and 650 K as shown in Fig. 4. The isochronal anneal study also showed that after a room temperature irradiation and subsequent 670 K anneal, the 53 K Al-Na<sup>+</sup> peak in the unswept blank increased from an initial value of  $5 \times 10^{-7}$  to  $2.2 \times 10^{-6}$  after the anneal. The Al-Na<sup>+</sup> loss peak also appeared in the Li-swept sample as a result of annealing although it was absent in the as-Li-swept sample. These latter results suggest that sodium is trapped at sites other than aluminum during growth. The irradiation and anneal treatment just described evidently rearranged the alkalis within the sample. It is conceivable that this process would take place at the 50 to 80°C operating temperature of a crystal oscillator (although very slowly) and contribute to the long term aging of the crystal.

The decay of the radiation induced Al-hole center should be matched by the corresponding growth of the Al-OH<sup>-</sup> and/or Al-M<sup>+</sup> centers. Sibley *et al.*<sup>15</sup> have measured the high temperature annealing behavior of the radiation-induced Al-OH<sup>-</sup> centers. Their results do not show any changes in the Al-OH<sup>-</sup> concentration for the 500-550 K temperature range where the Al-hole center decays. This result suggests that the anneal of the Al-hole center is matched by the return of an alkali ion to the Al site. Since our unswept samples contain mostly Li<sup>+</sup> ions and the Al-Li<sup>+</sup>

center does not have an acoustic loss peak, Fig. 4 does not show the expected lower temperature return of the alkali ions to the aluminum site. We have repeated the isochronal anneal study using the Na-swept blank. In this case, acoustic loss measurements of the 23 K and 53 K Al-Na<sup>+</sup> peak were used to track the behavior of the hole and the alkali centers. Polarized infrared absorption measurements of the 3367 cm<sup>-1</sup> band were also made on the Na-swept blank in order to track the Al-OH<sup>-</sup> center. Figure 5 shows that the decay of the 23 K Al-hole center acoustic loss peak in the 500 K to 550 K range is matched by an approximately 25% growth in the 53 K Al-Na<sup>+</sup> acoustic loss peak. The remaining growth of the 53 K peak closely matches the decay of Al-OH<sup>-</sup> as measured by infrared absorption. The increase in the Al-OH<sup>-</sup> center observed near 350 K does not have a corresponding change in either the Al-hole centers or Al-Na<sup>+</sup> centers. Subramaniam, Halliburton and Martin<sup>29</sup> have also observed this lower temperature anneal step of the Al-OH<sup>-</sup> centers. The annealing results shown in Fig. 5 suggest that the room temperature irradiation converted approximately 25% of the Al sites into Al-hole centers with the remaining 75% becoming Al-OH<sup>-</sup> centers. In the irradiation process, the Na<sup>+</sup> leaves the Al site and is subsequently trapped at an as yet unknown site in the crystal. Figure 6 shows the results plotted with the intensities of the centers converted to their aluminum content. When the Al-hole centers anneal out the 500 K to 550 K temperature range the Na<sup>+</sup> ion returns to the Al site. In unswept material the decay of the Al-hole centers must be accompanied by the return of Li<sup>+</sup> ions since no corresponding increase in the

Al-OH<sup>-</sup> centers is seen.

Often defect-related acoustic loss peaks can be described by

$$\delta Q^{-1} = D\omega\tau[1 + \omega^2\tau^2]^{-1} \quad (2)$$

where  $\delta Q^{-1}$  is the loss above the intrinsic background,  $D$  is the strength factor,  $\omega$  is the angular frequency, and  $\tau$  is the relaxation time for reorientation of the defect. The relaxation is usually thermally activated as the defect must go over an energy barrier to reach the other equivalent sites.<sup>17</sup> Thus,

$$\tau = \tau_0 \exp(E/kT) \quad (3)$$

where  $E$  is the barrier height and  $\tau_0$  contains the number of equivalent orientations and the attack rate. We have fit Eq. 2, with the relaxation time given by Eq. 3, to the 53 K and 135 K Al-Na<sup>+</sup> center loss peaks and to the three radiation-induced Al-hole loss peaks. The calculated parameters are given in Table I. Our activation energies and relaxation times for the Al-Na<sup>+</sup> center are in good agreement with Park and Nowick's dielectric loss results,<sup>21</sup> as well as those of Stevels and Volger.<sup>30</sup>

Stevels and Volger have also reported a radiation-induced dielectric loss peak with  $E = 7.5$  meV and  $\tau_0 = 5 \times 10^{-7}$  sec. This activation energy is in reasonable agreement with our 23 K peak, but the relaxation time is much longer. Taylor and Farnell<sup>31</sup> have also made dielectric loss measurements on irradiated quartz; they found a loss peak near  $E = 7.5$  meV in agreement with Stevels and Volger and an additional peak at low temperature with  $E = 1.2$  meV and  $\tau_0 = 6.2 \times 10^{-5}$  s.

#### 4. Conclusions

Sweeping  $\text{Li}^+$ ,  $\text{H}^+$ , or  $\text{D}^+$  into high-aluminum-content Premium Q grade quartz AT-cut resonators removes the small  $\text{Al-Na}^+$  loss peak at 53 K but does not introduce any new loss peaks at temperatures below 370 K. Therefore, we conclude that the  $\text{Al-Li}^+$  and  $\text{Al-OH}^-$  centers do not have anelastic loss peaks in this temperature region. Na-swept samples exhibit a very large 53 K loss peak. This shows that in as-grown quartz most of the Al sites are compensated by  $\text{Li}^+$ . Irradiation at room temperature replaces the interstitial alkali at the Al sites with a mixture of Al-hole and  $\text{Al-OH}^-$  centers. The radiation induced acoustic loss peaks at 23 K, 100 K and 135 K have the same anneal behavior as the Al-hole center. The thermal decay of the Al-hole center is accompanied by a corresponding return of the alkali ions to the Al sites. The higher temperature decay of the  $\text{Al-OH}^-$  center is also matched by the growth of the  $\text{Al-M}^+$  centers.

## 5. References

1. J. C. King and H. H. Sander. IEEE Trans. Nucl. Sci. NS-19, 23 (1972).
2. P. Pelligrini, F. Euler, A. Kahan, T. M. Flanagan, and T. F. Wrobel. IEEE Trans. Nucl. Sci. NS-25, 1267 (1978).
3. T. J. Young, D. R. Koehler, and R. A. Adams, Proceedings of the 32nd Annual Symposium on Frequency Control, 34 (1978). Copies available from the Electronic Industries Association, 2001 Eye Street, N.W., Washington, D.C. 20006.
4. D. R. Koehler and J. J. Martin, Proceedings of the 37th Annual Symposium on Frequency Control, pp.130-135 (1984). Copies Available from Systematics General Corporation,



Brinley Plaza, Route 38, Wall Township, NJ 07719.

5. J. C. King, Bell System Technical J. 38, 573 (1959).
6. R. A. Poll and S. L. Ridgway, IEEE Trans. Nucl. Sci. NS-13, 130 (December, 1966).
7. T. M. Flanagan and T. F. Wrobel, IEEE Trans. Nucl. Sci. NS-16, 130 (December, 1969).
8. B. R. Capone, A. Kahan, R. N. Brown, and J. R. Buckmelter, IEEE Trans. Nucl. Sci. NS-17, 217 (December, 1970).
9. T. M. Flanagan, IEEE Trans. Nucl. Sci. NS-21, 390 (December, 1974).
10. L. E. Halliburton, N. Koumvakalis, M. E. Markes, and J. J. Martin, J. Appl. Phys. 52, 3565 (1981).
11. A. Kats, Philips Res. Repts. 17, 133 (1962).
12. D. B. Fraser, J. Appl. Phys. 35, 2913 (1964).
13. S. P. Doherty, J. J. Martin, A. F. Armington, and R. N. Brown, J. Appl. Phys. 51, 4164 (1980).
14. M. E. Markes and L. E. Halliburton, J. Appl. Phys. 50, 8172 (1979).
15. W. A. Sibley, J. J. Martin, M. C. Wintersgill, and J. D. Brown, J. Appl. Phys. 50, 5449 (1979).
16. J. J. Martin and S. P. Doherty, Proceedings of the 34th Annual Symposium on Frequency Control, U.S. Army Electronics Command, Fort Monmouth, NJ, pp. 81-84 (1980). Copies available from Electronic Industries Association, 2001 Eye Street, Washington, D. C. 20006.
17. D. B. Fraser, Physical Acoustics, (W. P. Mason, ed.) Vol. V, Chap. 2, Academic Press, New York (1968).

18. A. W. Warner, Bell System Technical J. 40, 1193 (1960).
19. J. C. King, A. A. Ballman and R. A. Laudise, J. Phys. Chem. Solids 23, 1019 (1962).
20. B. Capone, A. Kahan and B. Sawyer, Proceedings of the 25th Annual Symposium on Frequency Control, pp. 109-112 (1971). Copies available from Electronic Industries Association, 2001 Eye Street, Washington, D. C. 20006.
21. S. Park and A. S. Nowick, Phys. Stat. Sol. (a) 26, 617 (1979).
22. J. Toulouse, E. R. Green and A. S. Nowick, Proceedings of the 37th Annual Symposium on Frequency Control, pp. 125-129 (1983). Copies available from Systematics General Corporation, Brinley Plaza, Route 38, Wall Township, NJ 07719.
23. H. G. Lipson, A. Kahan, R. N. Brown and F. Euler, Proceedings of the 35th Annual Symposium on Frequency Control pp.329-334 (1981). Copies available from Electronic Industries Association, 2001 Eye Street, Washington, D. C. 20006.
24. D. R. Koehler, Proceedings of the 35th Annual Symposium on Frequency Control, pp. 327-328 (1981). Copies available from Electronic Industries Association, 2001 Eye Street, Washington, D. C. 20006.
25. H. G. Lipson, F. Euler and A. F. Armington, Proceedings of the 32nd Annual Symposium on Frequency Control, pp.11-23 (1978). Copies available from Electronic Industries Association, 2001 Eye Street, Washington, D. C. 20006.

26. J. J. Martin, L. E. Halliburton and R. B. Bossoli, Proceedings of the 35th Annual Symposium on Frequency Control, pp. 317-320 (1981). Copies available from Electronic Industries Association, 2001 Eye Street, Washington, D. C. 20006.
27. M. G. Jani, R. B. Bossoli and L. E. Halliburton, Phys. Rev. B. 27, 2285 (1983)
28. J. J. Martin, Ho B. Hwang, and H. Bahadur, Proceedings of the 39th Annual Symposium on Frequency Control, p266 (1985).
29. B. Subramaniam, L. E. Halliburton and J. J. Martin, J. Phys. Chem. Solids, 45, 575(1984).
30. J. M. Stevels and J. Volger, Philips Res. Repts. 17, 284 (1962).
31. A. L. Taylor and G. W. Farnell, Can. J. Phys. 42, 595 (1964)

Table I. Acoustic-loss peak parameters

Defect	T (K)	E (meV)	$\tau$ ( $10^{-12}$ sec)
Al-Na <sup>+</sup>	53	57	0.165
Al-Na <sup>+</sup>	135	130	0.44
23K defect	23	8	830
Al-hole	100	90	1.0
Al-hole	135	110	2.7

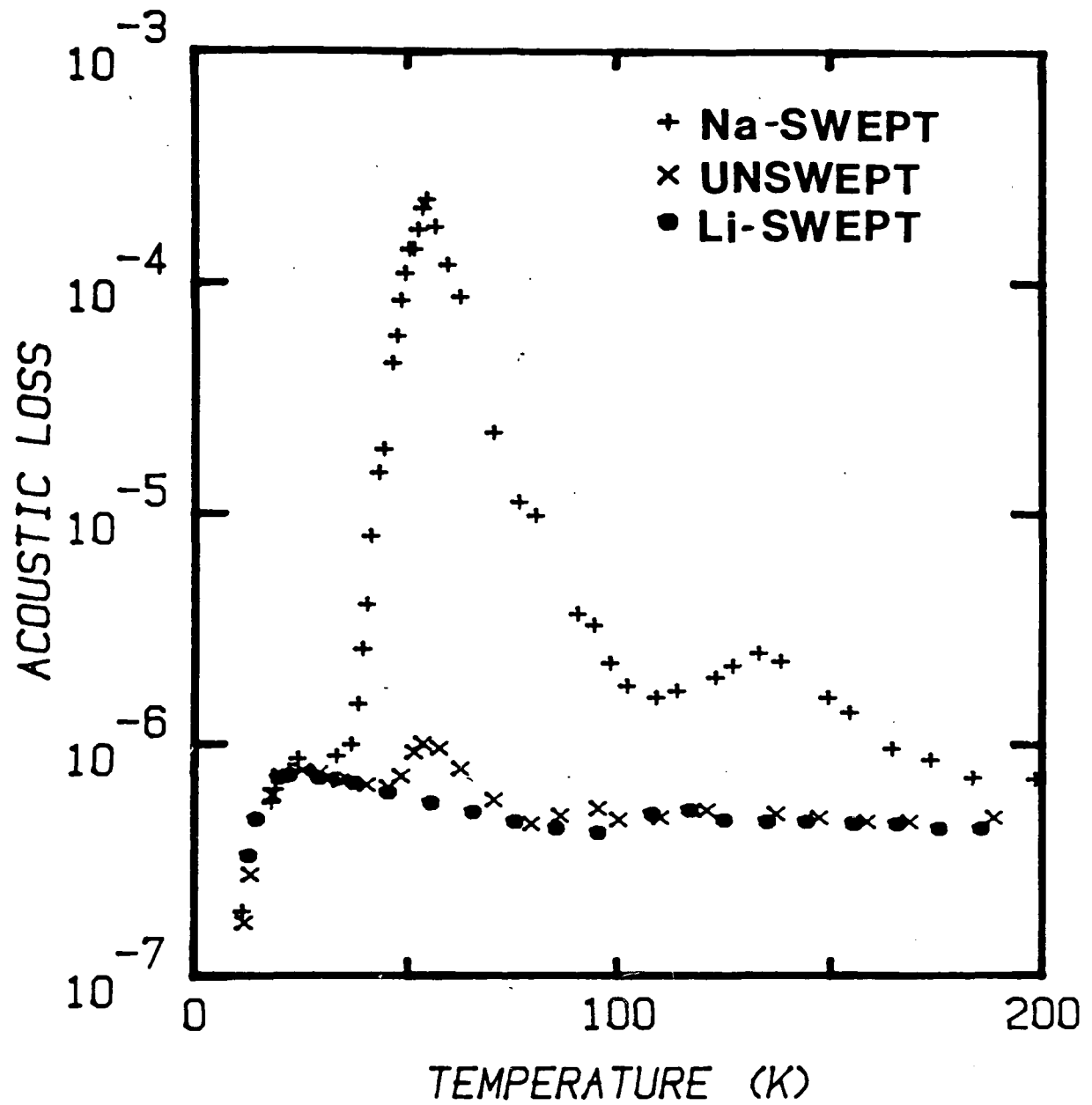


Fig. 1. The acoustic loss spectra of unswept, Na-swept and Li-swept resonator blanks all fabricated from the same bar of Sawyer Premium Q quartz are shown. The Al-Na<sup>+</sup> center is responsible for the peak at 53 K.

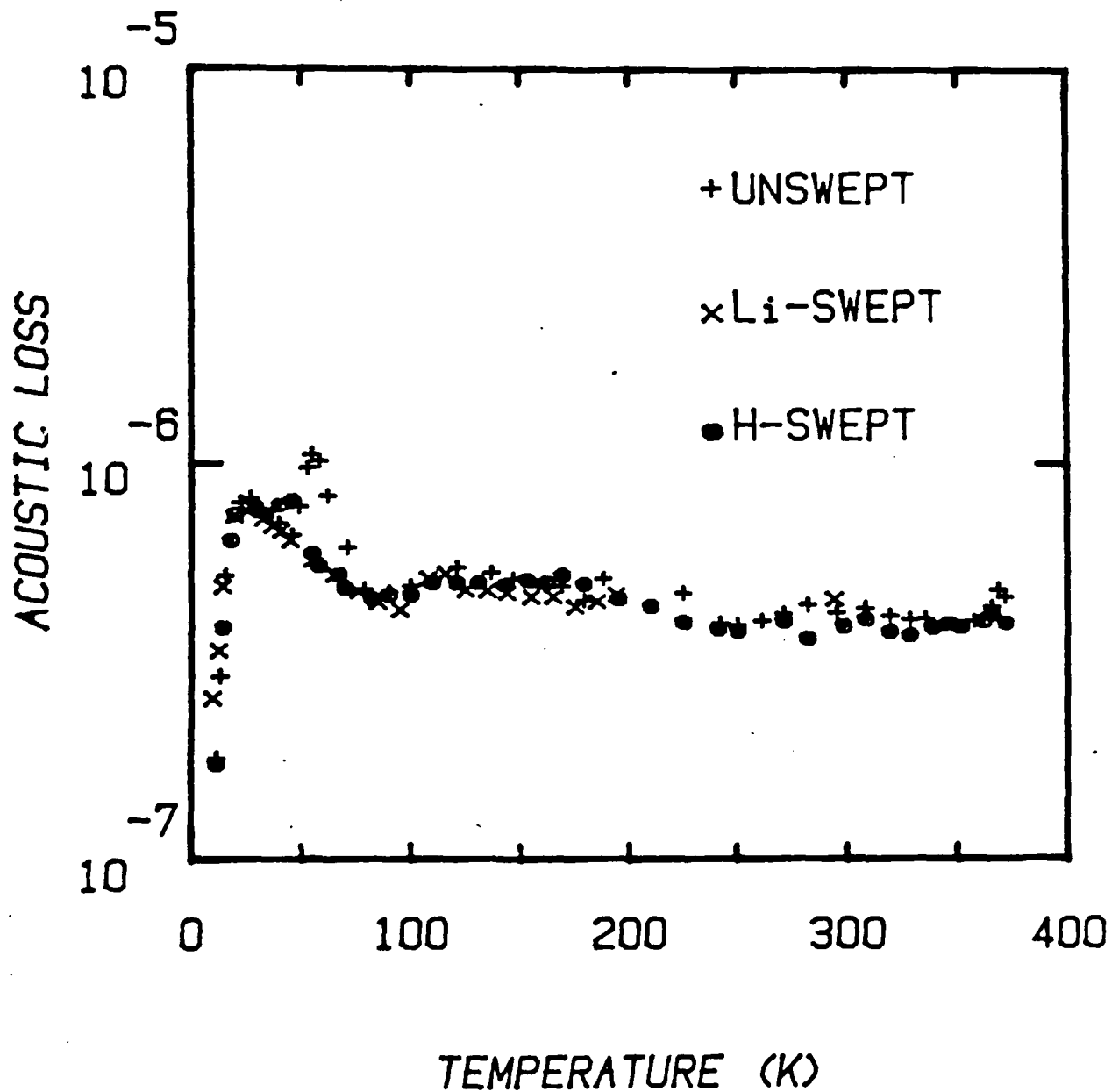


Fig. 2. The acoustic loss spectra of unswept, Li-swept and H-swept resonator blanks fabricated from a single bar of Premium Q quartz are shown. No loss peaks are observed that can be attributed to either the Al-Li<sup>+</sup> or Al-OH<sup>-</sup> centers.

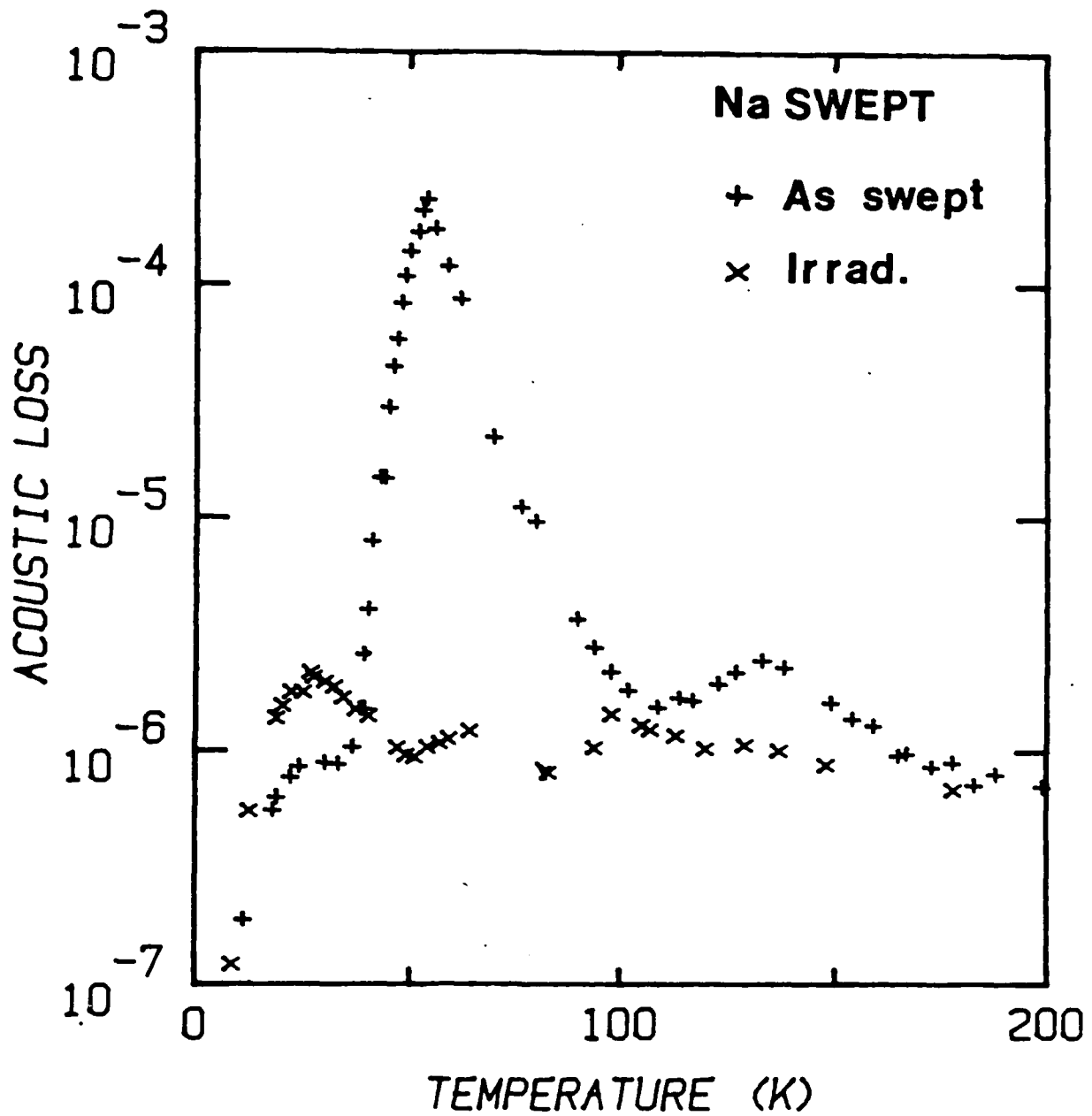


Fig. 3. The acoustic loss spectrum of the Na-swept blank is shown in the as-swept condition and after a room temperature irradiation. The irradiation removed the large 53 K peak due to the Al-Na<sup>+</sup> center and introduced a peak at 23 K and overlapping peaks at 100 K and 135 K which are related to the presence of the Al-hole center.

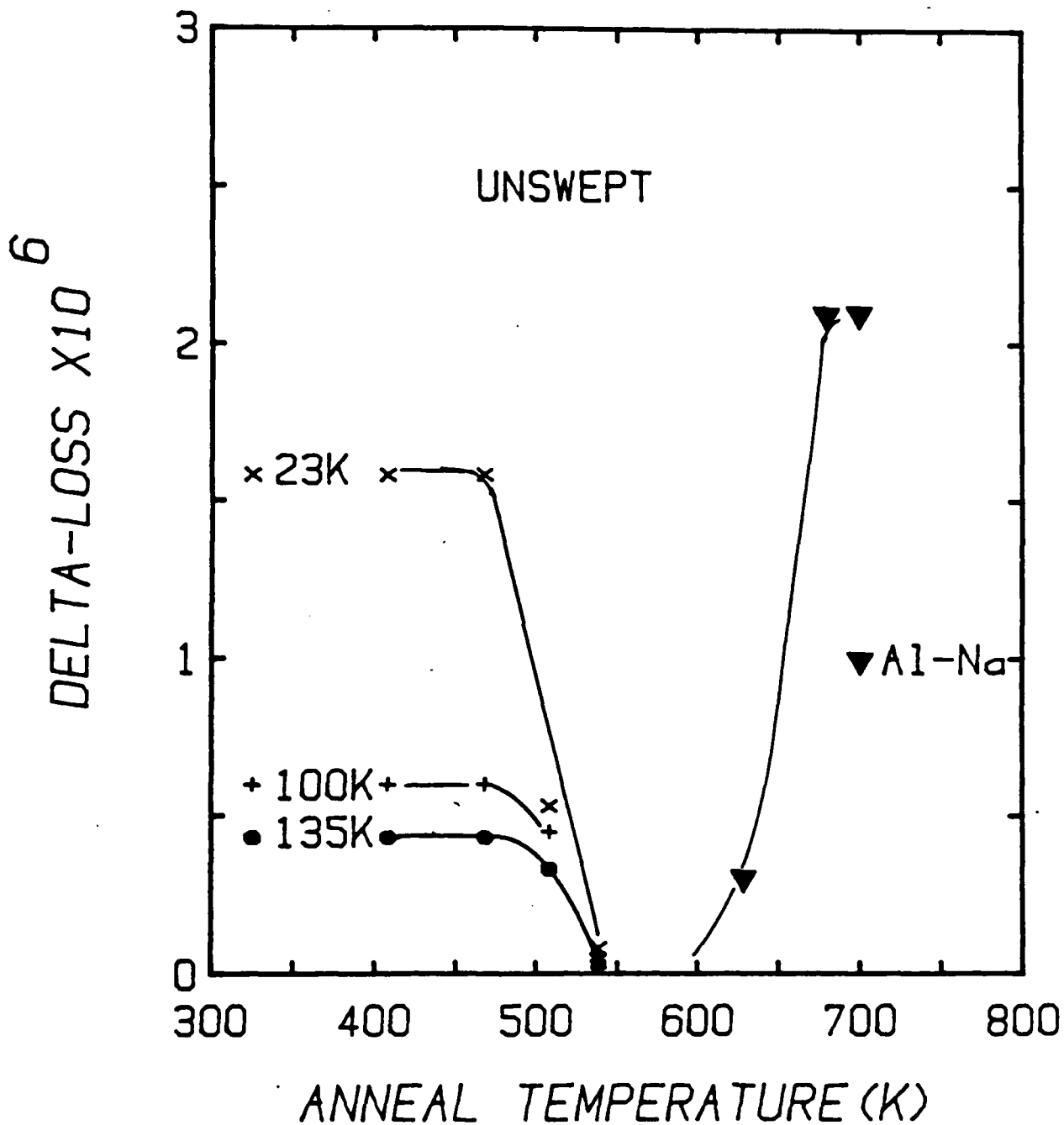


Fig. 4. The isochronal anneal behavior of the radiation induced peaks at 23 K , 100 K and 135 K shows that the three peaks go out together and at the same temperature as the Al-hole centers. These data were taken on the unswept blank. The Al-Na<sup>+</sup> center grows to four times its original concentration after the irradiation and anneal.

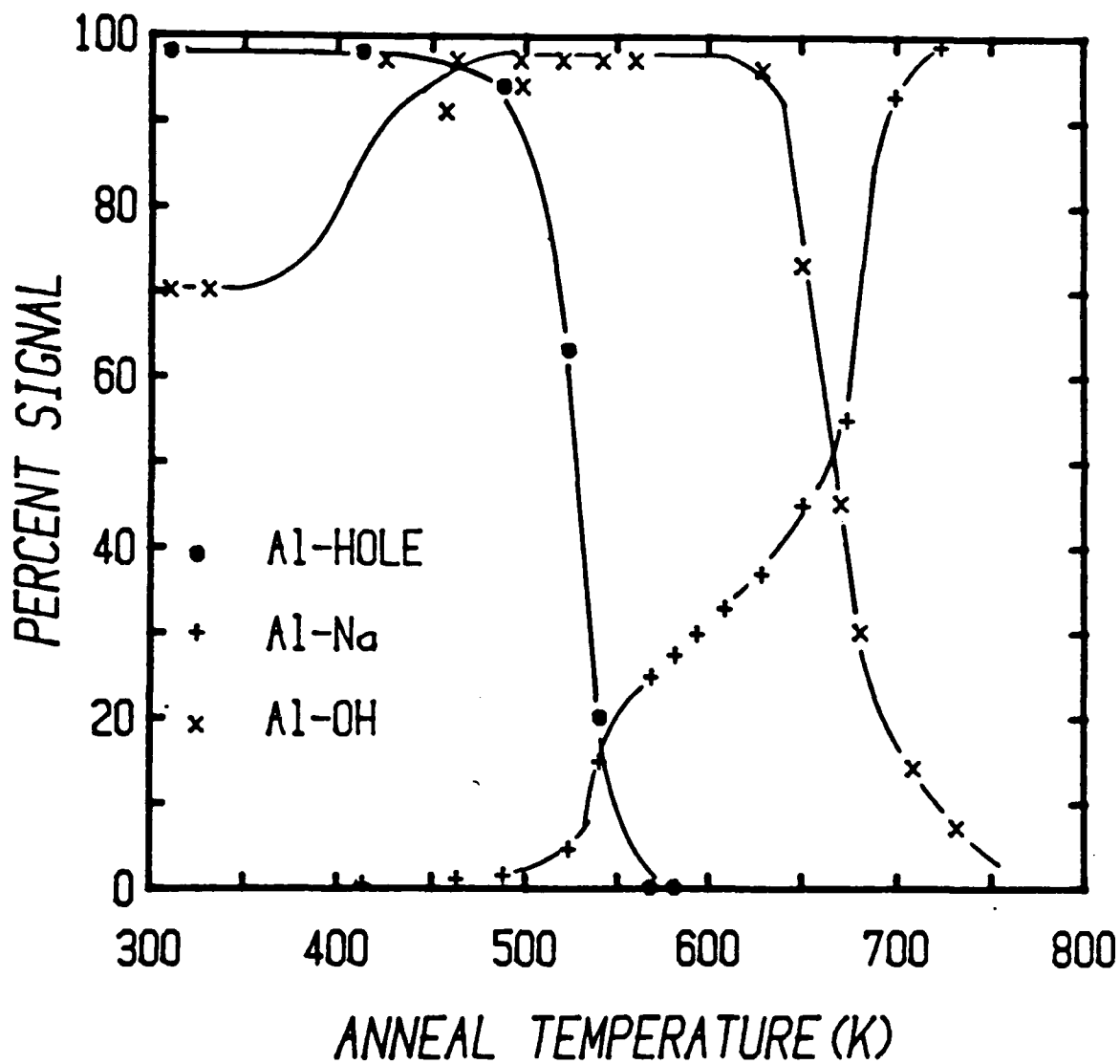


Fig. 5. The isochronal anneal of the 23 K Al-hole center peak and the Al-OH<sup>-</sup> infrared band which were produced by a room temperature irradiation of the Na-swept blank are shown. The decay of the Al-hole centers between 500 and 550 K is matched by a 25% recovery of the Al-Na<sup>+</sup> centers. The higher temperature decay of the Al-OH<sup>-</sup> centers is matched by the final recovery of the Al-Na<sup>+</sup> centers.



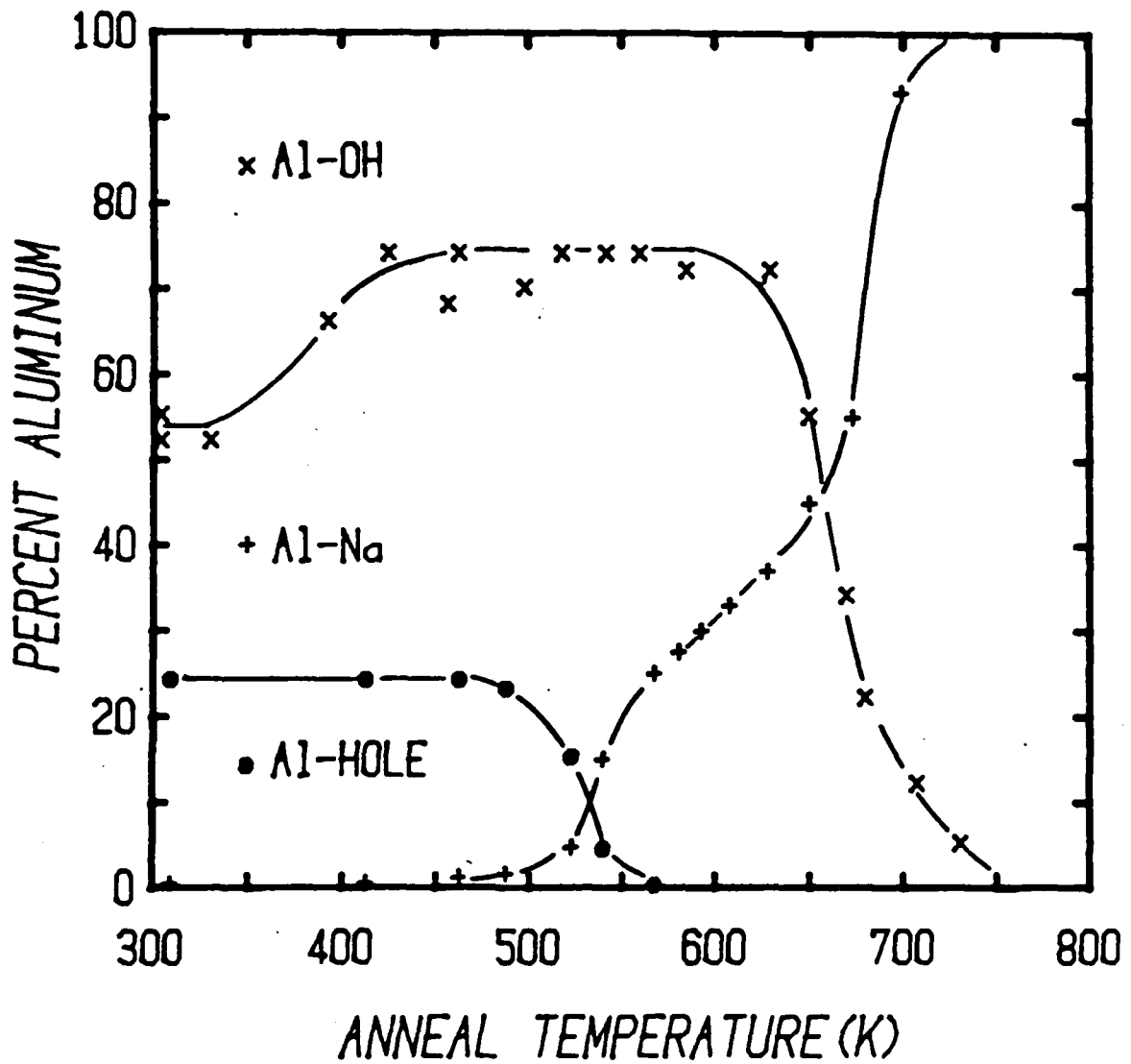


Fig. 6. The isochronal anneal for the room temperature irradiated Na-swept blank is shown with the intensities of the centers converted to the aluminum content.

## C. ELECTRODIFFUSION OF IONS IN ALPHA-QUARTZ

### 1. Introduction

Most as-grown quartz contains substitutional  $\text{Al}^{3+}$  with an interstitial alkali ion providing the charge compensation<sup>1</sup>. Additional unidentified point defects are known to trap protons forming the  $\text{OH}^-$  related growth defects<sup>2,3</sup> responsible for several IR absorption bands. These interstitial ions when either thermally or by radiation liberated from their traps can drift along the relatively large c-axis channels. This interstitial diffusion is responsible for the radiation induced transient acoustic loss<sup>4,5</sup>, the increasing acoustic loss observed at high temperatures<sup>6,7,8</sup>, and the annealing of radiation-induced defects. An electric field applied parallel to the c-axis can be used to electrodiffuse (i.e. sweep) the interstitial ions out of the sample while replacing them with specific ions. King<sup>9</sup> was among the first to exploit this process as a method of doping quartz with specific interstitial ions. Kats<sup>2</sup>, in his extensive infrared study of natural and synthetic quartz, used the process to sweep specific alkalis and protons into and out of quartz. Fraser<sup>10</sup> has described the basic process for the selective electrodiffusion of alkalis and Kreft<sup>11</sup> has shown that holes can be swept into quartz if the process is carried out in vacuum above the phase transition. Brown, O'Conner, and Armington<sup>12</sup> have investigated alkali sweeping and the use of inert gas atmospheres. A number of studies have shown that the radiation hardness of oscillators is significantly improved if the alkalis in the quartz have been replaced by protons<sup>5,13,14</sup>. A preliminary study by Martin *et al.*<sup>15</sup> showed that alkali ions were

much more mobile than protons during the sweeping process. They found that the activation energies ranged from 0.76 to 1.24 eV for alkalis and from 1.5 to 1.9 eV for hydrogen. Martinet al. brought the sample up to the 500°C sweeping temperature and then applied the E-field. They then observed current-versus-time curves which showed an initial rapid decay followed by a steady current which was interpreted as the motion of only one species of ion. Hansen<sup>16</sup> reported current peaks or plateaus in the 200-300°C range when the field was applied at room temperature. Gualtieri<sup>17</sup> has reported similar current peaks or plateaus; he also studied the sweeping conditions as a function of the reduction of etch channel density. Arnold<sup>18</sup> has reported that etching quartz produces very deep tunnels while Nielson and Foster<sup>19</sup> have observed that these tunnels tend to lie along the general growth direction (c-axis). The tunnels are apparently caused by dislocation networks which trap impurities<sup>20</sup>. Vig et al.<sup>21</sup> found that swept material showed fewer of these etch tunnels than unswept quartz.

Electrodifffusion is closely related to ionic conductivity. The main difference is the exchange of ions that takes place in the sweeping process, i.e., specific ions (protons or alkalis) are brought into the sample to replace interstitial alkalis that have been trapped at defects during the crystal growth process. Since the ions can only move along the c-axis channels ionic conductivity in quartz is a one-dimensional process. The number of mobile ionic charge carriers is governed by the number of traps and the depth of their trapping wells. If we assume that

only one kind of ion is mobile, the conductivity,  $\sigma$ , can be written as  $\sigma = ne\mu$  where  $n$  is the density of ions,  $e$  is the electronic charge, and  $\mu$  is their mobility. The mobility which is related to the diffusion coefficient is given by

$$\mu = (e/kT)\nu a^2 \exp(-E_m/kT) \quad (1)$$

where  $\nu$  is the attack frequency,  $a$  is the jump distance and  $E_m$  is the activation energy for interstitial migration<sup>22</sup>. If there is only one kind of trap present, say aluminum, the number per unit volume of mobile ions can be found from the law of mass action to be

$$n = (c/2)^{1/2} N_0 \exp(-E_a/2kT) \quad (2)$$

where  $c$  is the mole fraction of traps,  $N_0$  is the number of  $\text{SiO}_2$ 's per unit volume and  $E_a$  is the association energy between the ion and the trap<sup>24</sup>. Equation 2 assumes that only a small fraction of the interstitial ions have been thermally liberated from the traps. Thus, the conductivity can be expressed as

$$T = A \exp(-E/kT) \quad (3)$$

where  $E = E_a/2 + E_m$  and

$$A = N_0 (ea)^2 \nu (c/2)^{1/2} / k. \quad (4)$$

According to this analysis a plot of  $\log(\sigma T)$  versus  $T^{-1}$  should yield a straight line. Jain and Nowick<sup>24</sup> and, later, Green *et al.*<sup>25</sup> have reported such behavior except for some curvature at the higher temperatures for a number of alkali and hydrogen swept synthetic and natural quartz samples. They found activation energies ranging from 1.1 to 1.45 eV and values for the exponential prefactor,  $A$ , much larger than one would predict from Eq. 4 with reasonable values for  $\nu$  and  $a$ . Martin, *et al.* found similar behavior but with somewhat lower activation energies for their

ionic conductivity data which were collected during electrodiffusion runs<sup>15</sup>. We report here a continuation of their investigation.

## 2. Experimental Procedure

Most of the samples used in this study were cut from pure Z-growth lumbered bars of synthetic quartz obtained from Thermodynamics (TD-A) and Sawyer Research Products Premium Q (PQ-J) grades. Samples were also taken from an aluminum doped R-growth synthetic bar (HA-A). The various samples were identified according to the notation established by Markes and Halliburton [26]. Most of the samples were 3 mm thick by 15 mm x 17 mm Z-plates. Some measurements were also made on AT-cut plates. Prior to sweeping all samples were given an optical polish. The sweeping system and electrode deposition have been described previously [15]. The electric field was set up using a programmable power supply, and the sample current and temperature were measured using a digital multimeter and laboratory computer. Most of the runs used in this study were carried out by first applying the field at room temperature and then bringing the sample up to the nominal 500°C sweeping temperature at a rate of 2.2°C/min. The sample current was monitored during the entire run. This allowed the observation of the current peaks and plateaus reported by Hansen [16] while the sample was warmed to the operating temperature and the collection of apparent ionic conductivity data during cool-down. For alkali electrodiffusion the sample was held at the operating temperature for times ranging from 30 minutes to 2 hours; hydrogen sweeps were usually

carried out over a 24 hour period. For most of our tests on a given sample we first carried out a lithium run, then a sodium run and, finally, one or more hydrogen runs.

### 3. Results and Discussion

Figure 1 shows a typical current and temperature versus time curve for a hydrogen electrodiffusion run. For this run the sample (HA-A3) was brought up to the 500°C temperature at a rate of 2.2°C/min, held for approximately 24 hours at temperature, and then cooled at -2.2°C/min. The current trace in Fig. 1 shows a peak or plateau near 270°C similar to those reported by Hansen [16]. All of our hydrogen runs on samples that had not previously been H-swept show this structure. Once the sample reaches the fixed operating temperature we usually observe a current decay as shown in Fig. 1 when carrying out a H-sweep. Martin et al. reported a large initial current decay in their H-sweep data when the field was initially applied after the sample was at temperature. They interpreted their large initial current and its subsequent decrease as the replacement of the very mobile alkali ions with H<sup>+</sup>. The temperature versus time program for an alkali sweep is essentially the same except that the time at temperature is reduced. For alkali runs no significant peak or plateau is observed during warmup nor do we usually observe a large current decay after the sample reaches temperature. This second result is consistent with the small decay reported by Martin et al. for their alkali electrodiffusion runs.

Figure 2 shows the set of apparent ionic conductivity data taken during the cool-down portion of electrodiffusion runs on sample HA-A3. As described above the alkali electrodiffusion

runs were made before the hydrogen run. The low temperature end of our results for the lithium and sodium runs are in reasonable agreement with the high temperature end of the ionic conductivity data obtained by Green et al. [25] on Li- and Na-swept samples taken from the same high aluminum content stone. The agreement is encouraging because in our measurements ions are introduced into the sample from the source electrode, then moved through the sample and leave the sample at the negative electrode. Figure 3 compares the apparent ionic conductivity for lithium and hydrogen runs on samples taken from stones HA-A, PQ-J and TD-A. The curves for the sodium runs which fall slightly below the lithium data were omitted from Fig. 3 for purposes of clarity. Our Premium Q sample PQ-J has a comparable aluminum content and infrared spectrum to sample SQ-A of Green et al. and our ionic conductivities for the alkali runs are in reasonable agreement for the region of temperature overlap. The conductivity that we see for hydrogen in sample PQ-J is much lower than their results. Nearly all of our  $\log(T)$  versus  $1000/T$  plots show a tendency towards a lower slope at the higher temperatures. If there is only one dominant source for the mobile ion such as the substitutional aluminum this curvature would suggest that we are approaching saturation of the number of carriers and Eq. 2 must be replaced with a more complicated expression. While we cannot rule saturation out the high aluminum sample HA-A should show less curvature than the low concentration samples such as TD-A and that is not the case. Table I gives the activation energies and exponential prefactors for the curves shown in Fig. 3 and

the corresponding sodium runs. Because of the curvature, E and A were found for both the high and low temperature portions of the curves.

TABLE I. Activation Energies and Pre-exponential Factors.

Sample	Al(ppm)	Ion	High Temperature		Low Temperature	
			E(eV)	A( $10^6$ K/ohm.m)	E(eV)	A( $10^6$ K/ohm.m)
HA-A3	70	Li	0.95	0.29	1.06	1.7
		Na	1.02	0.32	1.08	0.84
		H	1.6	6.2	1.7	81
PQ-J4	10	Li	0.99	0.27	1.2	7.5
		Na	1.15	0.69	1.2	1.6
		H	1.72	3.2	---	---
TD-A18	5	Li	1.04	0.61	0.97	0.2
		Na	1.15	0.69	1.17	1.8
TD-A19	5	H	2.14	5600	----	---

The high temperature activation energies listed in Table I agree with the values reported by Martin *et al.* The low temperature alkali activation energies for sample HA-A and PQ-J are somewhat lower than the values given by Green *et al.*<sup>25</sup> for their HA-A and SQ-A samples. The prefactor is very sensitive to the choice of E. It is interesting to note that the prefactor, A, is one to two orders of magnitude larger than predicted when reasonable values of the jump distance and attack frequency are used in Eq. 4. This was noted earlier by Jain and Nowick<sup>24</sup>. They suggested that some of the aluminum was not charge compensated by monovalent ions and, thus, the law of mass action would yield a more complex expression than Eq. 2 for the number of mobile ions. The aluminum content of our samples was measured by the EPR technique of Markes and Halliburton<sup>26</sup>. Armington and Balascio<sup>27</sup> have compared the various analytical techniques for determining the aluminum content in quartz. They found that the EPR



technique gave excellent agreement with the more traditional chemical methods which would pick up all of the aluminum. We feel that there is not a large amount of "excess" aluminum present in most synthetic quartz samples; however, even a few percent of excess aluminum would change the law of mass action. While the exponential prefactor,  $A$ , is generally larger for the dirtier samples it does not scale directly with either  $c^{1/2}$  or  $c$  where  $c$  is the aluminum concentration. It may also be that there is an additional source of mobile ions. The  $\text{OH}^-$ -related growth-defects may be the source for extra protons but not for alkalis since no changes in their IR spectra are observed upon alkali or hydrogen electrodiffusion. One plausible source is the extended defects that are responsible for the etch tunnels. It is known that air<sup>17,21</sup> or hydrogen<sup>15</sup> sweeping reduces or eliminates the formation of the tunnels during etching. These extended defects are oriented along the growth direction and probably contain alkali impurities which are removed during air or hydrogen sweeping. Therefore, they must contribute to the conductivity. Another possibility is the alkali-related defect responsible for the acoustic loss peaks at 305 K and 340 K recently reported by Martin, Hwang and Bahadur<sup>28</sup>. They found that the 340 K peak was present in as-Na-swept samples. While the Li-related 305 K peak is weaker both defects may be present in as-grown material.

Figure 4 shows the conductivities versus temperature taken during the warm up period for a sodium electrodiffusion run and for two subsequent hydrogen runs on sample TD-A20. Similar curves were obtained for the other samples. The warm-up curves for the alkali runs do not show any structure in the 200-350°C

temperature range while the first H-sweep always shows a drop or plateau in the conductivity for the same temperature range. A second or third H-sweep on a previously H-swept sample results in curves like the dotted one in Fig. 4. Since, the ionic conductivity of hydrogen is several orders of magnitude lower than that of the alkalis as shown in Figs. 2 and 3 it seems reasonable to propose that the peak or plateau region observed by Hansen<sup>16</sup> during warm-up is caused primarily by the transition from conduction by the highly mobile alkali ions to conduction by the less mobile protons. Not all of the alkalis are removed at this step as shown by the peak and decay once the operating temperature is reached as shown in Fig. 1 and by the dotted curve in Fig. 4 for the third H-sweep on this sample.

#### 4. Summary

The apparent ionic conductivity data taken as the swept sample is cooled usually shows a curved  $\log(T)$  vs  $1000/T$  plot. The mobility of  $H^+$  in the electrodiffusion is much less than that of the lithium or sodium. The activation energies at high temperatures tend to be lower than those found from the low temperature data. The exponential prefactors are considerably larger than the values predicted for the aluminum content and reasonable estimates of the attack frequency and jump distance. It seems likely that an additional source of mobile ions must be present. The peak or plateau observed during the warm-up period for air or hydrogen sweeping appears to be caused by the transition from conduction primarily by alkalis to conduction by protons.

## 5. Acknowledgements

Augusto R. Lopez made many of the measurements while on leave from the Universidad Industrial de Santander, Bucaramanga, Colombia. C. Y. Chen measured the aluminum concentration of our samples.

## 6. REFERENCES

1. L. E. Halliburton, N. Koumvakalis, M. E. Markes and J. J. Martin, J. Appl. Phys. 52, 3565 (1981).
2. A. Kats, Phillips Res. Rpts. 17, 133 (1962).
3. J. J. Martin and A. F. Armington, J. Crystal Growth, 62, 203 (1983).
4. D. R. Koehler and J. J. Martin, J. Appl. Phys. 57, 5205 (1985).
5. J. C. King and H. H. Sanders, IEEE Trans Nucl. Sci. NS-19, 23 (1972).
6. D. B. Fraser, In Physical Acoustics, W. P. Mason, ed. Vol. V. PP54-110, Academic Press, NY (1968).
7. D. R. Koehler, Proc. 35th Ann. Freq. Control Symposium, USERADCOM, Ft. Monmouth, NJ, p.322, May 1981.
8. H. G. Lipson, A. Kahan, R. N. Brown and F. K. Euler, Proc. 35th Ann. Freq. Control Symposium, USERADCOM, Ft. Monmouth, NJ, p. 329, May 1981.
9. J. C. King, Bell System Tech. J. 38, 583 (1959).
10. D. B. Fraser, J. Appl. Phys. 35, 2913 (1964).
11. G. Kreft, Rad. Effects. 26, 249 (1975).
12. R. N. Brown, J. O'Conner and A. F. Armington, Mat. Res. Bull. 15, 1063 (1980).
13. T. M. Flanagan and T. F. Wrobel, IEEE Trans. Nucl. Sci. NS-

- 16, 130 Dec. (1969).
14. P. Pellegrini, F. Euler, A Kahan, J. M. Flanagan and T. F. Wrobel, IEEE Trans Nucl. Sci. NS-25, 1267 (1978).
  15. J. J. Martin, R. B. Bossoli, L. E. Halliburton, Brinda Subramaniam and J. D. West, Proc. 37th Ann. Freq. Control Symposium, USAERADCOM, Ft. Monmouth, NJ, p. 164 June 1983.
  16. W. P. Hansen, Proc. 38th Ann. Freq. Control Symposium, IEEE, p.38 May 1984.
  17. J. G. Gualtieri, Proc. 39th Ann. Freq. Control Symposium, IEEE, p. 247, May 1985.
  18. G. W. Arnold, Proc. 11th Ann. Freq. Control Symposium, p. 119 (1957).
  19. J. W. Nielsen and F. G. Foster, Am. Mineral, 45, 299 (1960).
  20. W. J. Spencer and K. Haruta, J. Appl. Phys. 35, 2368 (1964).
  21. J. R. Vig, J. W. LeBus and R. L. Filler, Proc. 31st Ann. Freq. Control Symposium, USAERADCOM, Ft. Monmouth, NJ, p. 113, May 1977.
  22. A. B. Lidiard, Hand. of Physik, 20, 246 (1957).
  23. A. D. Franklin, in Point Defects in Solids, J. H. Crawford and L. M. Slifkin, eds., Plenum, NY, Vol. 1, Ch. 1, (1972).
  24. H. Jain and A. S. Nowick, J. Appl. Phys. 53, 477 (1982).
  25. E. R. Green, J. Toulouse, J. Wacks and A. S. Nowick, Proc. 38th Ann. Freq. Control Symposium, IEEE, p.32, May 1984.
  26. M. E. Markes and L. E. Halliburton, J. Appl. Phys. 50, 8172 (1979).
  27. A. F. Armington and J. Balascio, Proc. 39th Ann. Freq Control Symposium, IEEE, p. 230, May 1985.

28. J. J. Martin, Ho B. Hwang and H. Bahadur, Proc. 39th. Ann. Freq. Control Symposium, IEEE, p. 266, May 1985.

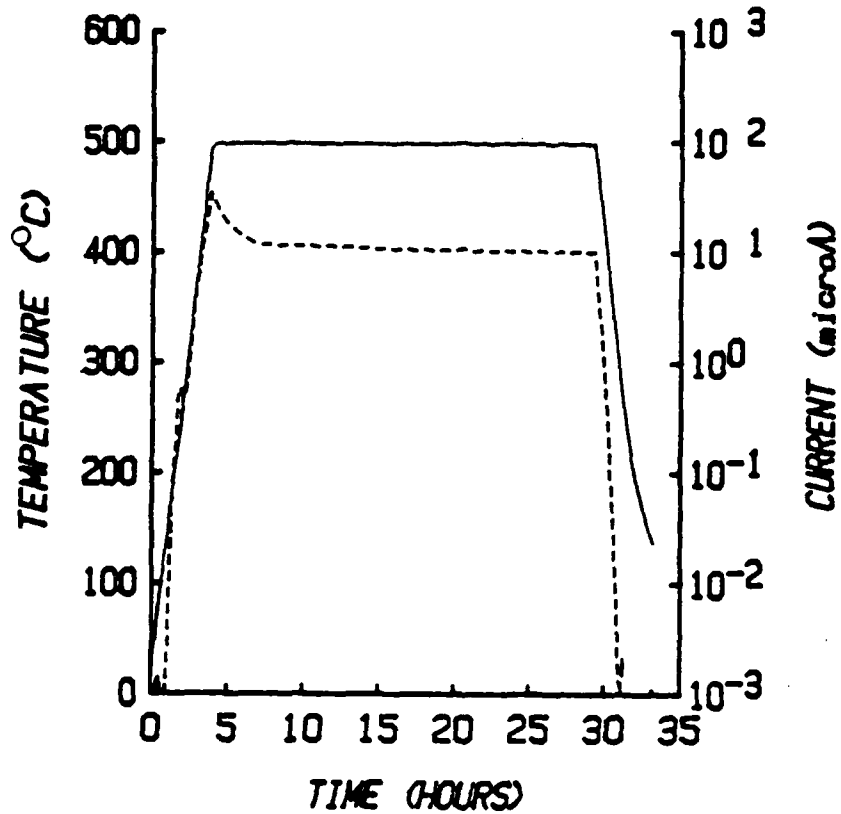


Fig. 1. The temperature and current profiles are shown for a hydrogen electrodiffusion run. The electric field was applied at room temperature.

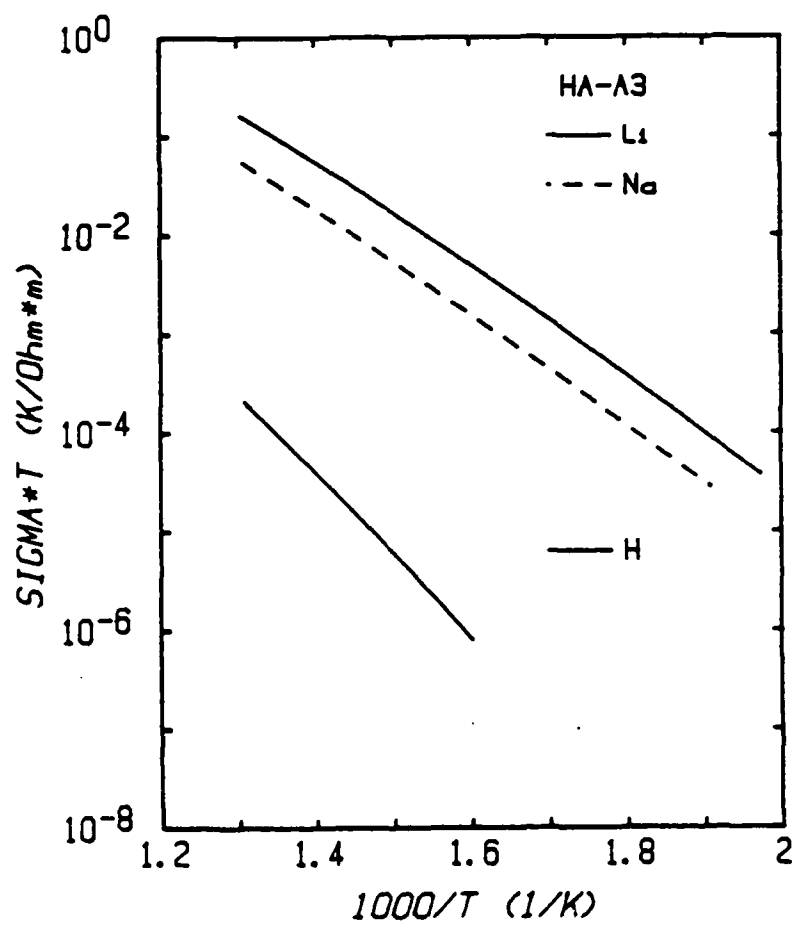


Fig. 2. The apparent ionic conductivities for  $\text{Li}^+$ ,  $\text{Na}^+$  and  $\text{H}^+$  in the high aluminum content sample are shown. The data were collected during cool-down at the end of the electrodiffusion run.

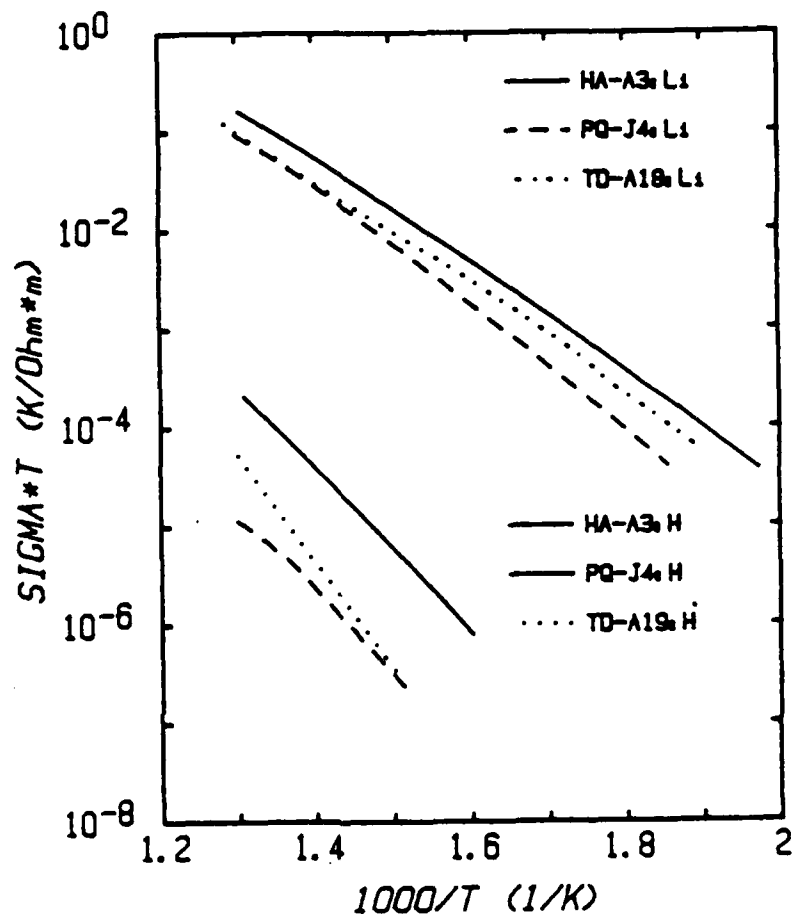


Fig. 3. The upper set of curves compare the conductivity of  $\text{Li}^+$  in three different samples; the lower curves compare the conductivity of  $\text{H}^+$  in the same samples.

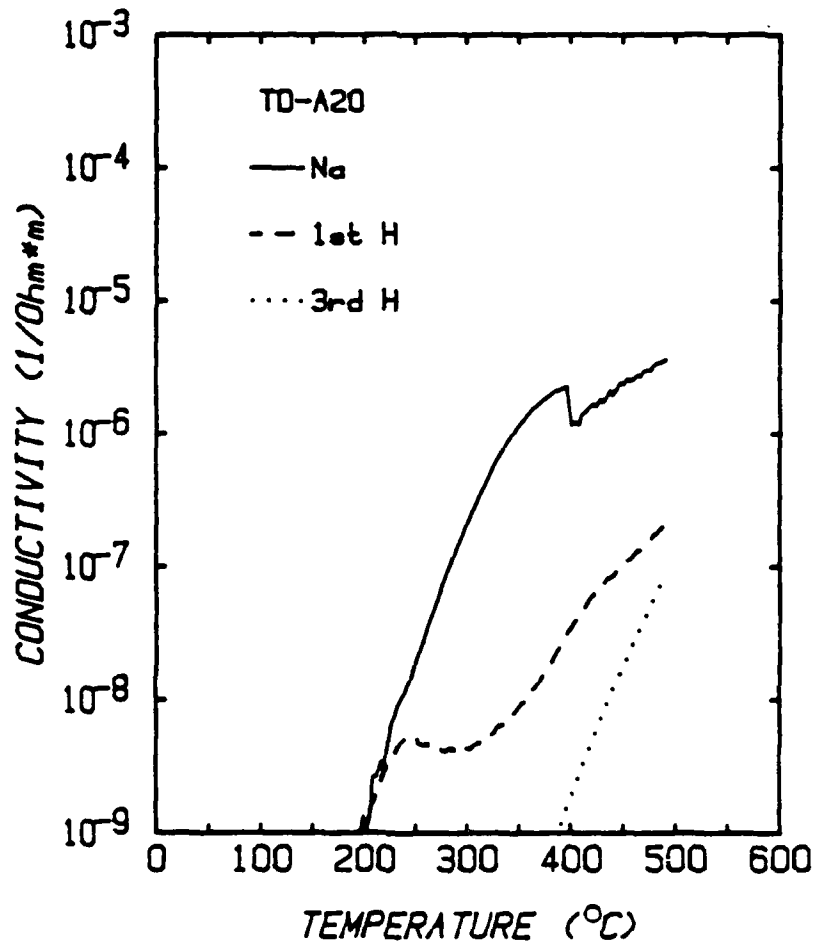


Fig. 4. The conductivity data taken during the warm-up period is shown for a Na-sweep and for subsequent H-sweeps on the same sample. The drop in conductivity near 250°C for hydrogen probably represents the transition to H<sup>+</sup> as the primary charge carrier.



## D. POINT DEFECTS IN NEUTRON-IRRADIATED QUARTZ

### 1. Introduction

Over the past three decades, much attention has been given to the point defects created in crystalline  $\text{SiO}_2$  by x-ray, electron, or heavy particle irradiation. Among the reasons for this interest are the applications of quartz-stabilized oscillators in navigation and communication satellites. Since these satellites may encounter a variety of radiations, it is necessary to understand how each specific component of the radiation spectrum affects their operation. Such knowledge will help, in the future, to anticipate and interpret radiation-induced variations in the performance of quartz oscillators.

A number of point defects have been identified in quartz; these include oxygen-vacancy-associated centers,<sup>1-7</sup> aluminum-associated trapped hole centers,<sup>8-11</sup> and the hydrogen atom.<sup>12</sup> Additional defects such as  $\text{OH}^-$  molecules trapped adjacent to various imperfections have been observed but not identified in detail.<sup>13-16</sup> The family of oxygen-vacancy-associated defects are usually referred to as E centers and they are present in silica<sup>17</sup> and the  $\text{SiO}_2$  interface region of MOS devices,<sup>18</sup> as well as in quartz. These oxygen vacancies are introduced either during the preparation, i.e., growth, of these materials or during subsequent irradiation. Vacancy formation by irradiation usually implies ionic displacement as a result of "knock-on" damage;<sup>19</sup> however, recent studies<sup>17,20-23</sup> have suggested that electronic excitations produced by ionizing radiation lead to transient displacement of oxygen ions in crystalline  $\text{SiO}_2$ .

Several studies of the effects of neutron irradiation on the frequency and Q of quartz resonators have been reported.<sup>24-26</sup> These investigators are in general agreement that the resonator frequency increases linearly with neutron dose, provided the effects of any simultaneous gamma-ray irradiation are accounted for separately. The neutron irradiation studies of quartz resonators have led to some unexpected results. Specifically, King and Fraser<sup>24</sup> found that the Q of an air-swept synthetic quartz resonator was reduced by the neutron irradiation but that subsequent thermal annealing caused the Q to increase above its value prior to the irradiation. Thus, the implication is that the properties of a resonator can be improved if the quartz blank is first neutron irradiated and then annealed near the  $\alpha$ - $\beta$  phase transition before final assembly of the resonator.

In the present paper we have used neutron irradiation to produce point defects in synthetic quartz. Electron spin resonance (ESR) and optical absorption (visible and infrared) spectra were obtained from a series of five samples, each subjected to a different neutron dose. Production and thermal anneal characteristics were determined for the  $E_1$  centers, the  $[AlO_4]^\ominus$  centers, a 210-nm absorption peak, and two previously unreported  $S = 1$  centers.

## 2. Experimental Procedure

A lumbered bar of high quality synthetic quartz (Premium Q grade, pure Z growth, right hand) was obtained from Sawyer Research Products, Eastlake, Ohio. The aluminum content of this bar was 3.5 ppm (atomic Si) as determined by the ESR technique.<sup>27</sup> Six samples, each having dimensions of 18 X 18 X 3 mm<sup>3</sup> in the X,

Y, and Z directions, respectively, were cut from the bar and then polished. Five of these six samples were neutron irradiated in the Research Reactor Facility at the University of Missouri-Columbia. The sixth sample was kept as a control for later comparison with the neutron-irradiated crystals.

Before the neutron irradiations, each sample was sealed inside a separate perforated aluminum capsule. These were then lowered into the reactor pool and left for a specified time (ranging from 0.14 to 27.8 hours). The temperature of the pool water, which was in direct contact with the crystals, was estimated to be between 100-150°C. Radiation doses (neutron flux  $> 1$  Mev) received by the five crystals were estimated to be  $3 \times 10^{15}$ ,  $1 \times 10^{16}$ ,  $6 \times 10^{16}$ ,  $2 \times 10^{17}$ , and  $7.5 \times 10^{17}$  neutrons/cm<sup>2</sup>. After removing the crystals from the reactor and waiting several weeks or more for their radioactivity to drop to safe levels, two smaller samples with dimensions  $8 \times 3 \times 3$  mm<sup>3</sup> and  $18 \times 10 \times 3$  mm<sup>3</sup> in the X, Y, and Z directions, respectively, were cut from each of the initial crystals for use in the ESR and the optical absorption experiments.

Optical absorption measurements in the visible and ultraviolet were done at room temperature using a Perkin-Elmer 330 spectrophotometer, while the infrared spectra were taken at 80 K with a Beckman 4240 spectrophotometer. Our homodyne ESR spectrometer operated at X-band with a Varian V-4531 rectangular cavity and a 100-kHz static field modulation frequency. Magnetic fields and microwave frequencies were measured with a Varian E-500 digital gaussmeter and a Hewlett Packard 5340A counter.

respectively. Thermal anneals were done using a small bench-top furnace. Once the furnace attained a desired temperature, the sample was placed inside and then removed after 15 minutes.

### 3. Results

Our ESR study of five neutron-irradiated synthetic quartz crystals indicates that various new (i.e., previously unreported) paramagnetic defects are present in addition to the familiar  $E_1$  centers and  $[AlO_4]^0$  centers. Figure 1 shows a room-temperature ESR spectrum obtained from the sample that received the highest neutron dose. The magnetic field, in this case, is parallel to the crystal's c axis and a single intense line representing the  $E_1$  centers easily dominates the spectrum. Additional holelike ESR lines appear on the low-field side of the  $E_1$  center spectrum and the defects responsible for them remain unidentified. These latter spectra will not be discussed in this paper.

Earlier studies<sup>7,28,29</sup> have shown that  $E_1$  centers have long spin-lattice relaxation times even at room temperature and that they are best observed when the microwave power is reduced and the spectrometer's phase sensitive detector is set "out-of-phase." Operating the spectrometer in this latter mode, along with a very small modulation amplitude, allowed us to demonstrate that the  $E_1$  ESR spectrum, including the 8 and 9 G hyperfine lines, obtained from this high-dose sample was identical in appearance to the usual  $E_1$  center spectrum produced by ionizing radiation (See, for example, Fig. 1 in Reference 7).

The ESR results shown in Figs. 2 and 3 were obtained at 77 K from this same high-dose sample. In Fig. 2, the 400-G region about "g = 2" contains two spectra, each consisting of a doublet

for this c-axis orientation of the magnetic field. The inner pair is labeled Doublet I and has a separation of 98.7 G while the outer pair is labeled Doublet II and has a separation of 246.5 G. Their  $g_c$  values are 2.0158 and 2.0205, respectively. Also, two less intense lines are observed at the equivalent half-field values of each doublet. No clear indication of hyperfine lines associated with these doublets was found. For clarity, the central portion of the spectrum is omitted from Fig. 2 and is then shown separately in Fig. 3 in an expanded view. This central region contains the  $E_1$  center signal along with additional holelike spectra which are unidentified. It is reasonable to expect that some of these holelike spectra in Fig. 3 are from  $O_2^-$  molecules, similar to ESR spectra observed in silica.<sup>30</sup>

As the magnetic field is rotated from the c axis in the plane perpendicular to the X-axis (i.e., a twofold axis), each doublet is observed to split equally into three less intense doublets. The maximum doublet separation achieved during rotation is approximately 465 G for Doublet I. A similar value is found for Doublet II. Such large angular dependences of the doublet separations suggest that these centers are  $S = 1$  spin systems. The alternative would be  $S = 1/2$ ,  $I = 1/2$  (100% abundant) spin systems, but our observation of the half-field  $M_S = 2$  transitions eliminates this latter possibility and confirms the  $S = 1$  nature of these defects.

Some of the neutron-irradiated samples had a slight smoky coloration which prompted our study of optical absorption in the visible and ultraviolet spectral range. The absorption bands in

the visible were extremely weak and were assumed to arise from  $[\text{AlO}_4]^\circ$  centers.<sup>31</sup> However, an intense absorption peak was found to occur near 210 nm in all five irradiated samples. This band, obtained at room temperature in the high-dose sample, is shown in trace b of Fig. 4 and the corresponding absorption in the unirradiated control sample is shown in trace a. Additional absorption bands may be present in the vacuum-UV region but we were unable to observe them because our commercial spectrophotometer was restricted to wavelengths greater than 185 nm.

The intensity of the optical absorption peak at 210 nm and the intensities of the ESR spectra for the  $E_1$  centers, the  $[\text{AlO}_4]^\circ$  centers, and the two new  $S=1$  defects are shown in Fig. 5 as a function of neutron dose. Each dose level corresponds to one of the five irradiated samples. All of the defect concentrations increase with dose except for the  $[\text{AlO}_4]^\circ$  center.

The results of thermally annealing the high-dose sample from room temperature to 500°C are shown in Fig. 6. After each anneal step, the  $E_1$  centers and the ultraviolet absorption band at 210 nm were monitored at room temperature and the two  $S = 1$  centers were monitored at 77 K. The major step in the thermal decay of the  $E_1$  centers occurs in the 300-400°C region in this study, which is consistent with previous observations in electron-irradiated synthetic quartz crystals.<sup>7</sup> A small decrease in the  $E_1$  centers was observed near 100°C and is associated, perhaps, with the defects that give rise to thermoluminescence peaks in this temperature range.<sup>32</sup> Between 200 and 300°C, the  $E_1$  center concentration increases slightly and this is believed to possibly correlate with the thermal decay of  $[\text{AlO}_4]^\circ$  centers.<sup>7</sup> Doublet II

thermally decays sharply in the 230-265°C range, whereas Doublet I initially grows in the 375-425°C range and then thermally decays in the 425-500°C region.

A final observation about the neutron-irradiated quartz samples concerns their infrared spectra. There are three infrared bands, at 3400, 3437, and 3585  $\text{cm}^{-1}$ , normally encountered in synthetic quartz when examined at 77 K.<sup>14,15</sup> They are attributed to  $\text{OH}^-$  molecules trapped adjacent to unidentified imperfections in the quartz. Although present in our control sample, these three bands were not observed in our neutron-irradiated samples. Instead, a single very broad and very low intensity band was observed over the entire 3400 to 3600  $\text{cm}^{-1}$  region. Presumably, the neutrons have significantly disrupted the lattice, causing a shifting of the protons into more poorly defined trapping sites with a resultant "smearing" of the infrared spectrum.

#### 4. Discussion

Many of the recent studies of paramagnetic point defects in quartz have used x-rays, gamma rays, or high-energy electrons as a means of production. In general, these "ionizing" radiations create defects as a result of electronic excitation mechanisms,<sup>19</sup> i.e., formation of electron-hole pairs followed (1) by stabilization of the electrons and holes at separate trapping sites or (2) by the conversion of this excitation energy to kinetic energy of ion displacement. In contrast, a primary mechanism involved during neutron irradiation is ionic displacement due to momentum transfer. This involves direct

collisions of the heavier neutrons with the lattice ions. Electron irradiation also can cause these direct displacements (via momentum transfer) in most oxides but the cross-section for such events is relatively low compared to neutrons. We have found that direct displacement events have been negligible in previous studies from our laboratory<sup>7</sup> that used electron irradiations for production (i.e., saturation effects were observed in the growth curves of all defects).

The  $E_1$  center involves an oxygen vacancy and, thus, provides a convenient monitor of possible differences between the effects of ionizing radiation and neutrons. Weeks<sup>1</sup> was the first to describe the  $E_1$  center and Silsbee<sup>2</sup> later characterized its spin-Hamiltonian parameters. Both of these investigators used fast neutron irradiation to produce the  $E_1$  centers and it has been assumed that ionic displacements were responsible for the defect formation as opposed to electronic excitations associated with the accompanying gamma-ray flux from the reactor.

More recently, Jani et al.<sup>7</sup> used 1.7-MeV electrons from a Van de Graaff accelerator to create  $E_1$  centers in synthetic quartz. They found that performing the irradiations at room temperature did not directly create  $E_1$  centers, but that an additional step of warming the crystal to 300°C was necessary. Also, they observed a saturation in the  $E_1$  growth curves for doses approaching 10 Mrads(Si). These results were interpreted to mean (1) a significant number of oxygen vacancies were initially present as a result of the crystal growth process and (2) the room-temperature irradiation created stably trapped electrons and holes which then were redistributed during the



subsequent 300°C thermal anneal to form the E<sub>1</sub> centers.

Our results shown in Fig. 5 verify that vacancies are produced in quartz by neutron irradiation. The concentrations of vacancy-associated defects begin to increase rapidly with neutron dose above approximately  $5 \times 10^{16}$  neutrons/cm<sup>2</sup>. At doses below this level, growth-induced vacancies appear to dominate, with the gamma rays from the reactor serving to convert them into observable paramagnetic defects. For reference, the concentration of E<sub>1</sub> centers found in the sample receiving the highest neutron dose was a factor of 40 greater than the maximum concentration of E<sub>1</sub> centers produced by electron irradiation in our control sample. The E<sub>1</sub> centers created by the electron irradiation are presumably a measure of the number of growth-induced oxygen vacancies initially present, and neutron-induced oxygen-vacancy formation is suggested as the reason for this subsequent factor of 40 increase.

Similar rapid growths of the 210-nm absorption peak and Doublets I and II for doses above  $5 \times 10^{16}$  neutron/cm<sup>2</sup> also are explained by neutron-induced vacancy and/or interstitial production. However, the [AlO<sub>4</sub>]<sup>o</sup> center does not include a vacancy; thus its production, as shown in Fig. 5, is quite different from the other defects. The [AlO<sub>4</sub>]<sup>o</sup> centers grow with increasing dose at the lower levels of radiation, but a decrease in concentration of these centers occurs when the number of neutron-induced vacancies starts to dominate over the growth-induced vacancies. This latter observation suggests that the neutron irradiation produces additional hole trapping sites which then compete with the substitutional aluminum ions for available

holes. One possibility for these additional hole traps are the  $E_1$  centers.

We are unable to make a unique correlation of the 210-nm absorption peak with a particular ESR spectrum. A number of paramagnetic defects have approximately the same growth characteristics, including the  $E_1$  center, Doublets I and II, and many of the other defects whose spectra are shown in Figs. 1 and 3. The 210-nm peak gradually disappears over the anneal range from about 175 to 500°C, as described in Fig. 6, and does not exhibit well-defined steps that coincide with decays of the paramagnetic defects. This gradual decay suggests that perhaps the 210-nm peak contains contributions from more than one defect. During the 1950s and 1960s, many experimental studies were done on ultraviolet absorption bands in quartz.<sup>33-38</sup> In particular, Mitchell and Paige<sup>33,34</sup> observed two major bands at 217.5 and 163.1 nm in their study of neutron and x-ray irradiated material. These were labeled the C and E bands, respectively, and it was suggested that the C band might be due to an electron trapped at an oxygen vacancy and the E band might be the related interstitial oxygen ion. Our present study was limited to wavelengths greater than 185 nm, but even it strongly suggests that an extension of the work of Mitchell and Paige and others in the vacuum ultraviolet is needed. Such an investigation should be directly combined with a study of the many oxygen-vacancy ESR spectra that have now been fully characterized in quartz.

An important feature of our present study has been the discovery of the two new  $S = 1$  defects. These centers have never been observed in any of our electron-irradiated samples, and this

supports our previous conclusion that neutron-induced ionic displacements must be a critical step in their formation. Thermal annealing showed that Doublets I and II decay near 470°C and 250°C, respectively. After the sample had been annealed to 500°C, an electron irradiation at room temperature and another at 77 K failed to repopulate these  $S = 1$  defects. The positive  $g$ -shifts exhibited by Doublets I and II suggest that they each consist of a pair of trapped holes. These hole-trapping sites in the  $\text{SiO}_2$  lattice are, most likely, associated with oxygen either in the form of substitutional  $\text{O}^-$  ions or as  $\text{O}_2^-$  molecules. Our preliminary angular dependence study revealed a maximum splitting of 465 G for Doublet I and a similar value for Doublet II. Assuming a simple dipole-dipole interaction between the two unpaired spins, this splitting can be used to estimate the separation of the two unpaired spins. This gives a value of approximately 5 Å for Doublet I.

A detailed model can not yet be presented for the two  $S = 1$  centers. Neutron irradiation results in the formation of both vacancies and interstitial ions and these  $S = 1$  centers could be associated with either type of defect. For example, a pair of separated holes in the form of  $\text{O}^-$  ions might be stabilized by an intervening silicon vacancy (possibly combined with other neighboring defects). In fact, Nuttall and Weil<sup>39</sup> have suggested that silicon vacancies can act as traps for hydrogen ions and for radiation-induced holes. However, because of the estimated 5-Å separation of the two spins in our case, it is unlikely that the  $\text{O}^-$  ions could both be within a single  $\text{SiO}_4$  structural unit (where

2.7 Å is the expected separation). Insight to possible models for our two defects may be obtained from consideration of similar holelike  $S = 1$  defects in quartz that have been assigned by Weil and coworkers<sup>11,40</sup> to pairs of  $O^-$  ions.

Another possibility for the origin of these  $S = 1$  centers is oxygen interstitials. When created by the neutron irradiation, these interstitials are expected to bond to substitutional oxygen ions and form diatomic oxygen molecules. Two of these molecules could be stabilized near each other, and trapping of holes could convert them to paramagnetic forms (e.g.,  $O_2^-$  molecules).

#### 5. Acknowledgement

The authors wish to thank Mr. Stephen L. Gunn of the Research Reactor Facility at the University of Missouri-Columbia for his assistance in performing the neutron irradiations. This work was supported in part by the DOE Reactor Sharing Program.

#### 6. References

1. R. A. Weeks, J. Appl. Phys. 27, 1376 (1956).
2. R. H. Silsbee, J. Appl. Phys. 32, 1459 (1961).
3. R. A. Weeks and C. M. Nelson, J. Am. Ceram. Soc. 43, 399 (1960).
4. R. A. Weeks, Phys. Rev. 130, 570 (1963).
5. J. Isoya, J. A. Weil, and L. E. Halliburton, J. Chem. Phys. 74, 5436 (1981).
6. R. B. Bossoli, M. G. Jani, and L. E. Halliburton, Solid State Commun. 44, 213 (1982).
7. M. G. Jani, R. B. Bossoli, and L. E. Halliburton, Phys. Rev. B 27, 2285 (1983).
8. J. A. Weil, Radiat. Eff. 26, 261 (1975).

9. R. H. D. Nuttall and J. A. Weil, Can. J. Phys. 59, 1696 (1981).
10. R. H. D. Nuttall and J. A. Weil, Can. J. Phys. 59, 1709 (1981).
11. R. H. D. Nuttall and J. A. Weil, Can. J. Phys. 59, 1886 (1981).
12. J. Isoya, J. A. Weil, and P. H. Davis, J. Phys. Chem. Solids 44, 335 (1983).
13. A. Kats, Philips Res. Rep. 17, 133 (1962).
14. R. N. Brown and A. Kahan, J. Phys. Chem. Solids, 36, 467 (1975).
15. H. G. Lipson, F. Euler, and P. A. Ligor, Proceedings of the 33rd Annual Symposium on Frequency Control, 122 (1979). Copies available from the Electronic Industries Association, 2001 Eye Street, N.W., Washington, DC 20006.
16. B. Subramaniam, L. E. Halliburton, and J. J. Martin, J. Phys. Chem. Solids, 45, 575(1984).
17. D. L. Griscom, Proceedings of the 33rd Annual Symposium on Frequency Control, 98 (1979). Copies available from the Electronic Industries Association, 2001 Eye Street, N.W., Washington, DC 20006.
18. D. L. Griscom and W. B. Fowler, in The Physics of MOS Insulators, edited by G. Lucovsky, S. T. Pantelides, and F. L. Galeener (Pergamon Press, New York, 1980), pp. 97-101.
19. E. Sonder and W. A. Sibley, in Point Defects in Solids, edited by James H. Crawford, Jr., and Lawrence M. Slifkin (Plenum, New York, 1972), Vol. 1, Chap. 4, pp. 201-290.

20. G. H. Sigel, J. Non-Cryst. Solids 13, 372 (1973/74).
21. L. W. Hobbs and M. R. Pascucci, J. Phys. (Paris), Colloq. 41, C6-237 (1980).
22. M. R. Pascucci, J. L. Hutchison, and L. W. Hobbs, in The Scientific Basis for Nuclear Waste, edited by S. V. Topp (Elsevier, New York, 1982).
23. K. Tanimura, T. Tanaka, and N. Itoh, Phys. Rev. Lett. 51, 423 (1983).
24. J. C. King and D. B. Fraser, Proceedings of the 16th Annual Symposium on Frequency Control, 7 (1962). National Technical Information Service Accession Nr. AD 285086.
25. T. M. Flanagan and T. F. Wrobel, IEEE Trans. Nuc. Sci. NS-16, 130 (1969).
26. E. P. EerNisse, IEEE Trans. Nuc. Sci. NS-18, 86 (1971).
27. M. E. Markes and L. E. Halliburton, J. Appl. Phys. 50, 8172 (1979).
28. D. L. Griscom, Phys. Rev. B 20, 1823 (1979).
29. D. L. Griscom, Phys. Rev. B 22, 4192 (1980).
30. E. J. Friebele, D. L. Griscom, M. Stapelbroek, and R. A. Weeks, Phys. Rev. Lett. 42, 1364 (1979).
31. N. Koumvakalis, J. Appl. Phys. 51, 5528 (1980).
32. M. G. Jani, L. E. Halliburton, and E. E. Kohnke, J. Appl. Phys. 54, 6321 (1983).
33. E. W. J. Mitchell and E. G. S. Paige, Proc. Phys. Soc. (London) B67, 262 (1954).
34. E. W. J. Mitchell and E. G. S. Paige, Phil. Mag. 1, 1085 (1956).
35. C. M. Nelson and J. H. Crawford, J. Phys. Chem. Solids 13,

296 (1960).

36. C. M. Nelson and R. A. Weeks, J. Am. Ceram. Soc. 43, 396 (1960).
37. G. W. Arnold, Phys. Rev. 139A, 1234 (1965).
38. G. W. Arnold, Phys. Rev. 140A, 176 (1965).
39. R. H. D. Nuttall and J. A. Weil, Solid State Commun. 33, 99 (1980).
40. J. Isoya, W. C. Tennant, Y. Uchida, and J. A. Weil, J. Magn. Res. 49, 489 (1982).

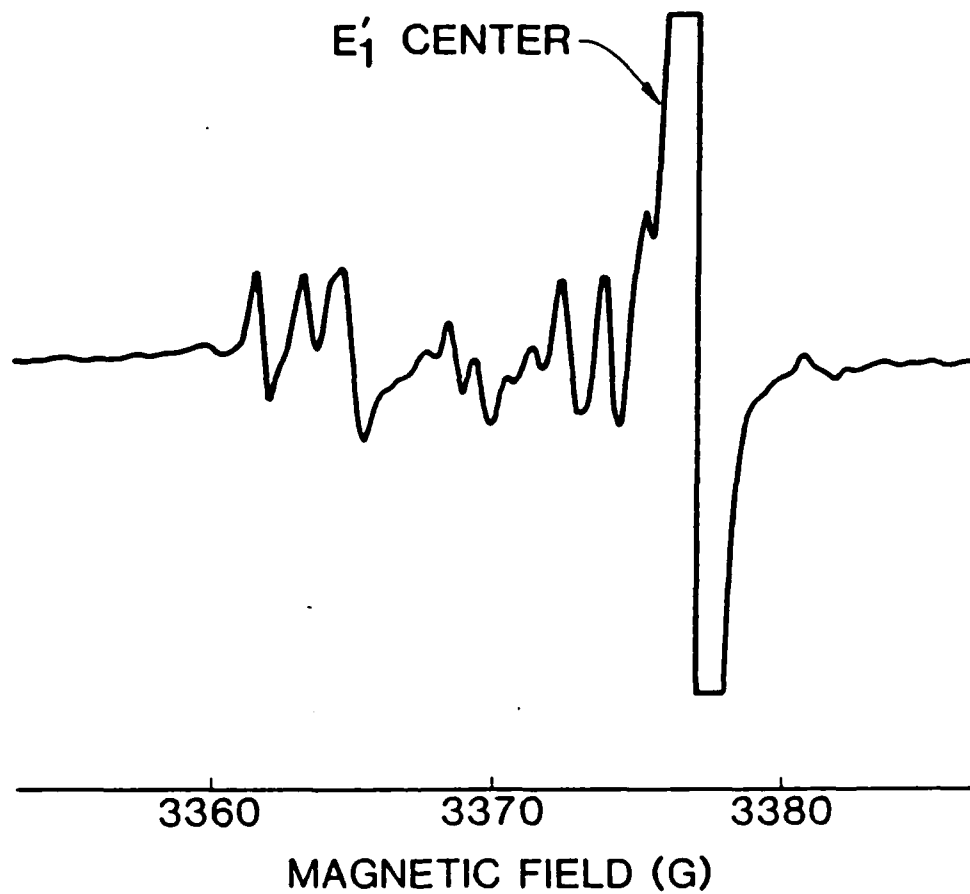


Fig. 1. Electron spin resonance spectrum taken at room temperature of the quartz sample receiving a dose of  $7.5 \times 10^{17}$  neutrons/cm<sup>2</sup>. The magnetic field was parallel to the c axis and the spectrometer was operated in the "normal" mode.



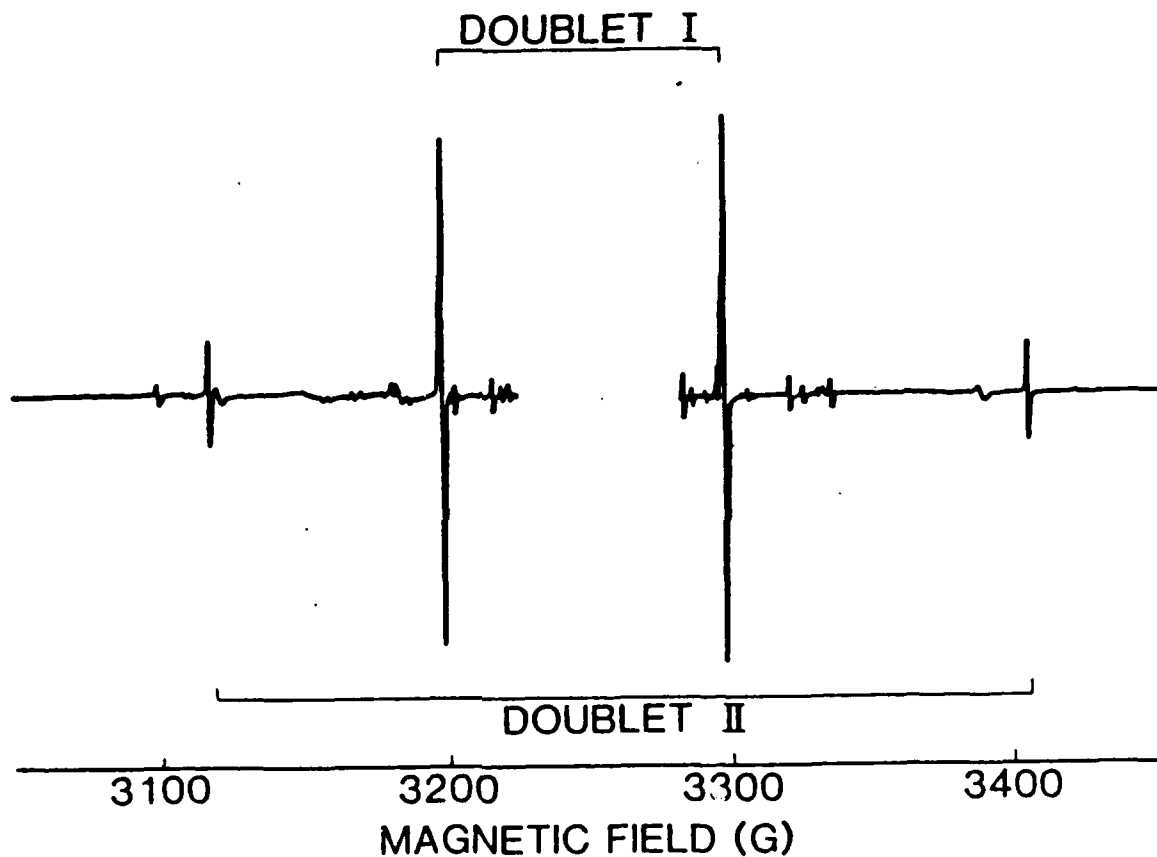


Fig. 2. The c-axis ESR spectrum taken at 77 K from the sample receiving the dose of  $7.5 \times 10^{17}$  neutron/cm<sup>2</sup>. To more clearly illustrate Doublets I and II, the central portion of the spectrum is omitted and is shown separately in Fig. 3.

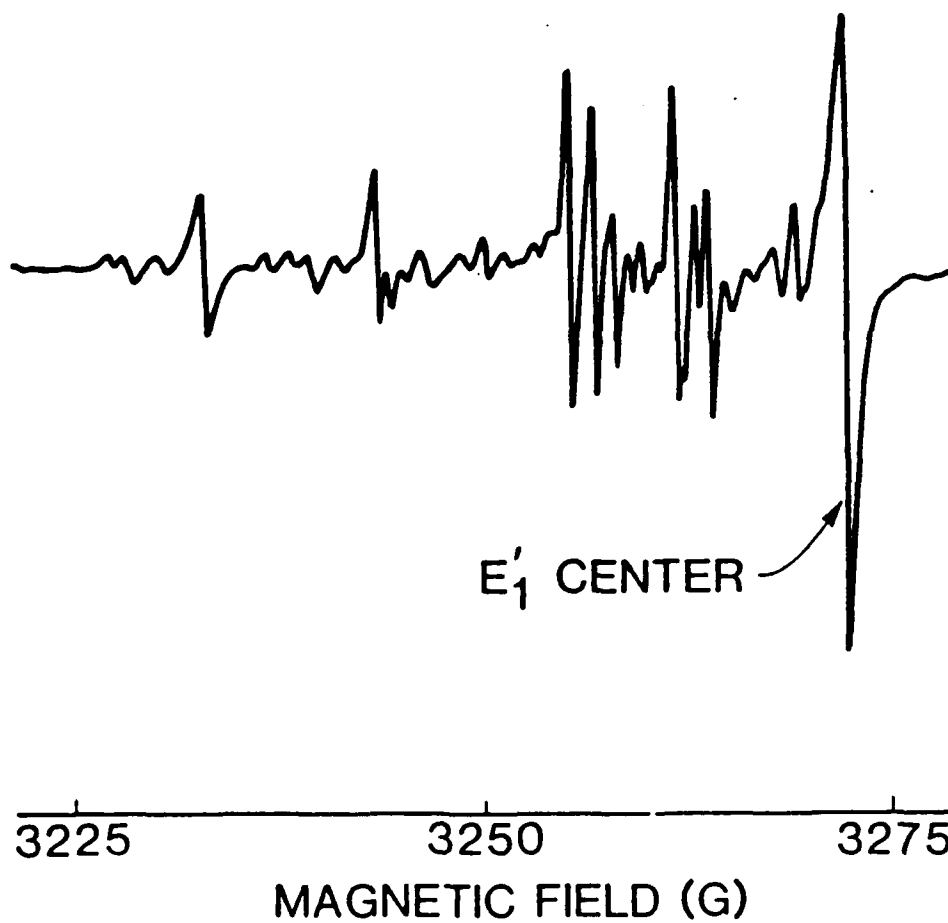


Fig. 3. The c-axis ESR spectrum corresponding to the omitted central portion of Fig. 2.

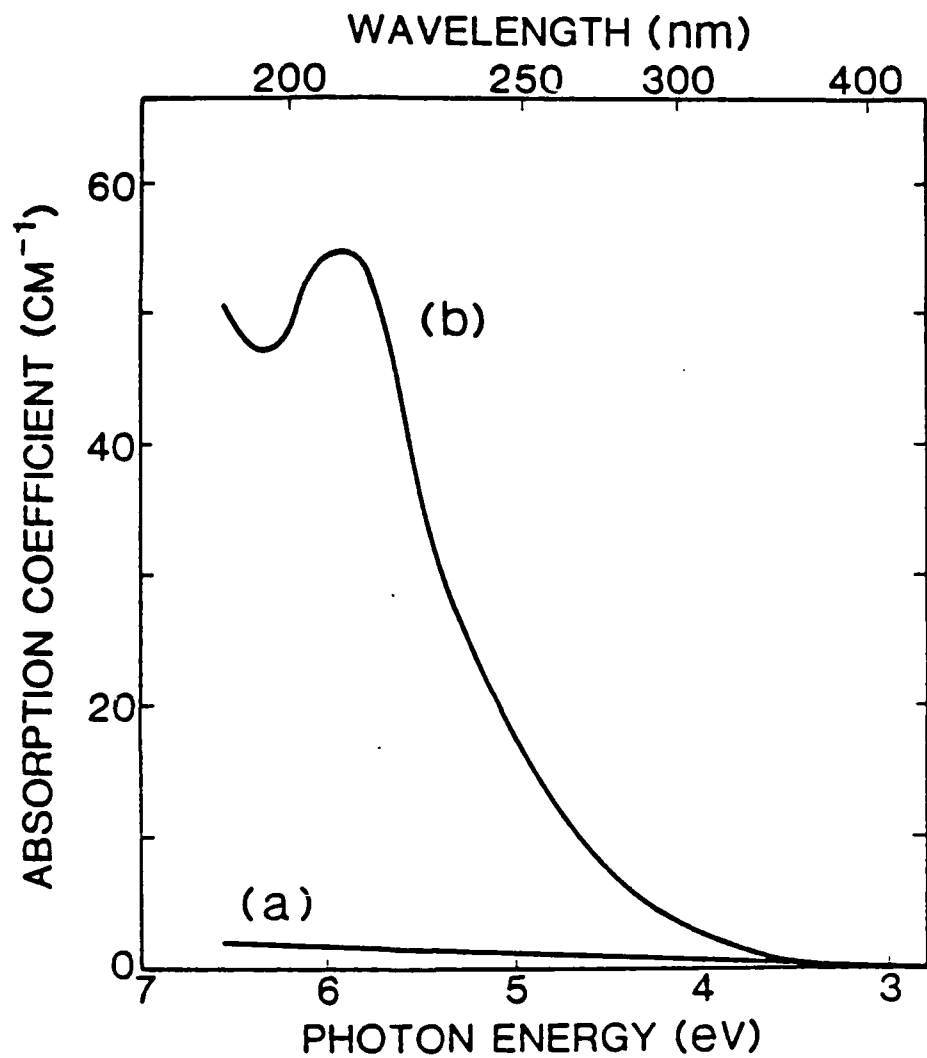


Fig. 4. The ultraviolet absorption spectrum obtained from the unirradiated control sample (trace a) is compared to the spectrum from the sample receiving the dose of  $7.5 \times 10^{17}$  neutron/cm<sup>2</sup> (trace b).

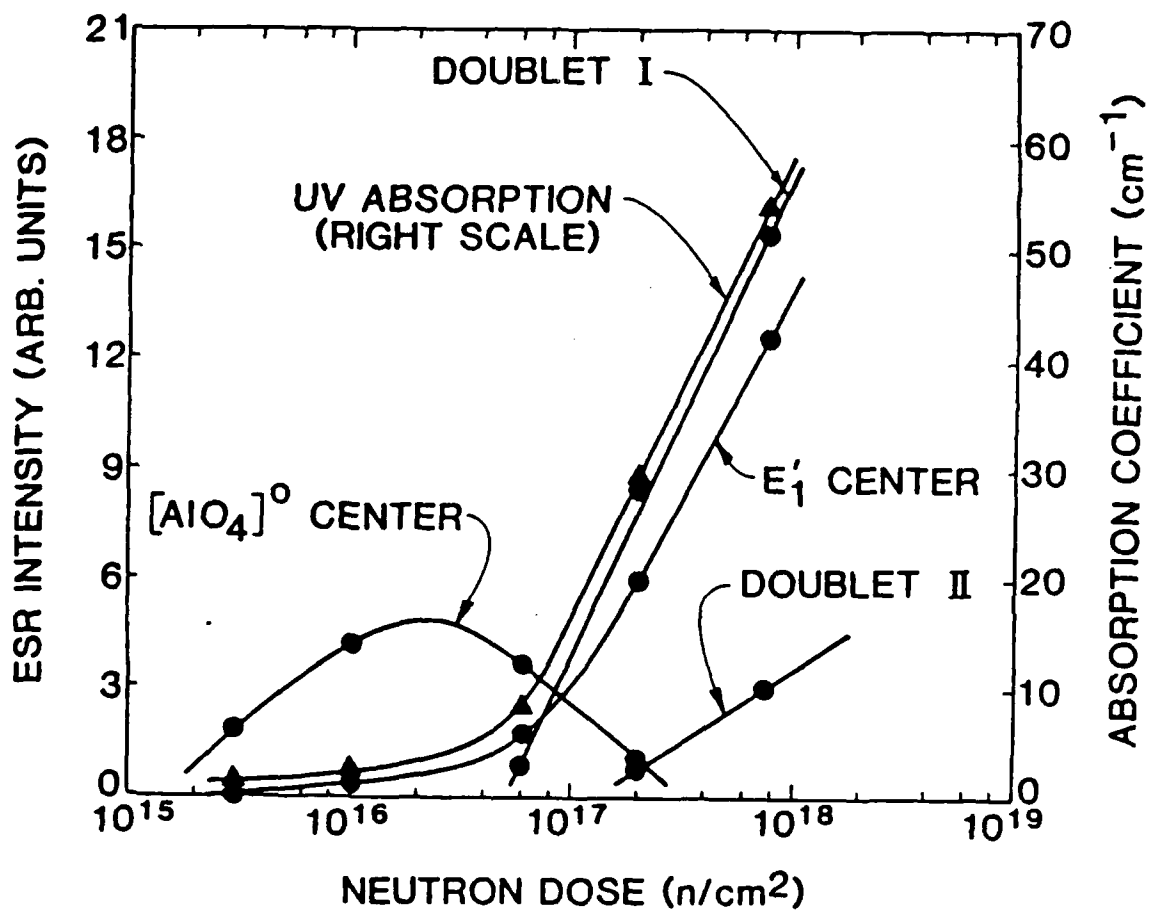


Fig. 5. The intensities of the ESR spectra (filled circles) and the 210-nm ultraviolet absorption peak (filled triangles) are plotted as a function of neutron dose received by the five quartz samples.

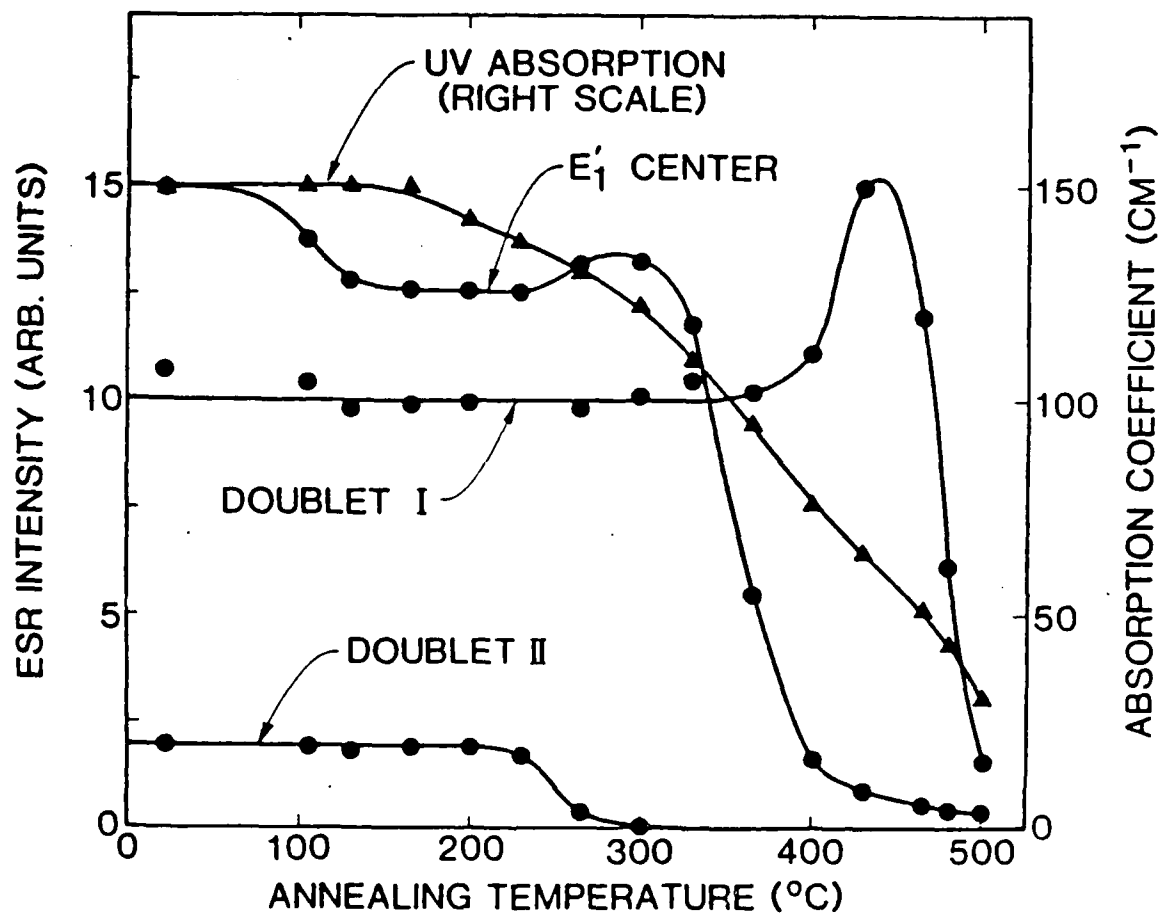


Fig. 6. Thermal anneal results obtained from the sample receiving a dose of  $7.5 \times 10^{17}$  neutron/cm<sup>2</sup>. The ultraviolet absorption scale is on the right and the arbitrary ESR intensity scale is on the left.

E. OBSERVATION OF A SIMPLE LITHIUM-ASSOCIATED ELECTRON TRAP  
IN CRYSTALLINE  $\text{SiO}_2$

Determining the identities of electron trapping centers in the various forms of  $\text{SiO}_2$  has been a long standing problem.<sup>1-3</sup> Electron-spin-resonance (ESR) experiments reveal large concentrations of holelike centers in both silica and single-crystal quartz after room-temperature irradiation; however, there are no corresponding ESR spectra representing equivalent concentrations of trapped electrons. It is possible that paramagnetic electron centers are present but are difficult to observe because of either extremely long or short spin-lattice-relaxation times. It is equally possible that the electrons are trapped in pairs, thus forming diamagnetic electron centers. Alkali ions are often suspected of being a key participant in these unseen electron centers in  $\text{SiO}_2$ , primarily because they have a positive charge and they are nearly always present, either as network modifiers in silica or simply as interstitials in quartz.

The lack of paramagnetism in amorphous chalcogenide semiconductors<sup>4</sup> has led to the concept of negative-U centers<sup>5</sup> and, thus far, the silicon vacancy in crystalline silicon is the best known example of such a defect.<sup>6,7</sup> Extending this concept of a negative-U defect to quartz provides a plausible explanation for the apparent lack of paramagnetic electron traps after room-temperature irradiation. In the conclusion of the present Letter, we suggest that the newly observed defect described herein could combine in pairs during room-temperature irradiation and then decay at higher temperatures by releasing not one but

two electrons.

In this section, we describe the observation of a simple lithium-associated  $S = 1/2$  electron trap in quartz. This defect is thermally stable below 180 K and is formed by radiation whenever isolated interstitial lithium ions drift along the open channels characteristic of the quartz structure. The c-axis ESR spectrum ( $g_c = 1.9995$ ) shows a small hyperfine splitting (0.9 G) due to one  ${}^7\text{Li}$  nucleus and a large hyperfine splitting (404.7 G) due to one  ${}^{29}\text{Si}$  nucleus. Based on these observations, we suggest that the defect consists of an extra electron stabilized by an interstitial lithium ion in the otherwise perfect lattice. The most important and surprising feature of this defect is the localization of the unpaired spin density on one of the adjacent four-coordinated silicon ions instead of on the lithium itself. Thus, contrary to our naive expectation, trapping of an electron by a lithium ion during irradiation at 77 K does not result in a lithium atom analogous to the hydrogen atom<sup>8</sup> found in  $\text{SiO}_2$ . Instead our model is similar to the lithium-compensated germanium centers<sup>9-11</sup> and the silver atom center<sup>12</sup> previously observed in quartz. Following the notation scheme proposed by Weil,<sup>2</sup> we label our new defect the  $[\text{SiO}_4/\text{Li}]^0$  center.

Our data were obtained from an unswept bar of synthetic quartz provided by Thermo-Dynamics, Inc. of Shawnee Mission, Kansas. Samples with dimensions of  $7 \times 3 \times 2 \text{ mm}^3$  in the X, Y, and Z directions, respectively, were cut from the +X-growth region. Defects were produced with x-rays from a Machlett OEG-60 tube (50 KV, 30 mA) positioned five cm from the sample. Each irradiation lasted five min during which time the sample was

either placed in a stream of nitrogen gas precooled to the desired temperature or immersed in a styrofoam container of liquid nitrogen or ice water. The ESR spectrometer was an IBM Instruments (Bruker) Model ER2000 operating at 9.283 GHz with 100-kHz field modulation. All ESR spectra were taken with the sample at 77 K by using a finger Dewar extending into an IBM 4102ST rectangular cavity.

The ESR spectrum shown in Fig. 1 was taken with the magnetic field parallel to the c axis. It consists of a central four-line spectrum, with splittings of 0.9 G, surrounded by a pair of similar, but less intense, four-line spectra located 188.6 G above and 216.1 G below the central set. The four lines within each set are due to a single  ${}^7\text{Li}$  nucleus (93% abundant,  $I = 3/2$ ) while the widely split weaker lines are due to a single  ${}^{29}\text{Si}$  nucleus (4.7% abundant,  $I = 1/2$ ). These two widely split sets of lines are approximately 40 times smaller than the center set, which is in agreement with the natural abundance of  ${}^{29}\text{Si}$ . Because of an extremely long spin-lattice-relaxation time, all ESR data from the  $[\text{SiO}_4/\text{Li}]^0$  center were taken with the spectrometer's lock-in amplifier set "out-of-phase." Similar relaxation behavior has been reported for E and E' centers in quartz.<sup>13,14</sup>

Our assignment of the four-line ESR spectra in Fig. 1 to a lithium nucleus, instead of sodium, was initially based on the relative distribution of alkali ions normally found in synthetic quartz. Martin<sup>15</sup> has shown that this distribution predominantly favors  $\text{Li}^+$  in commercially grown quartz even though the mineralizer is mostly  $\text{Na}_2\text{CO}_3$  with only a small amount of  $\text{Li}_2\text{CO}_3$  added.



To provide more convincing proof for the nuclear identity, an ENDOR experiment was performed.<sup>16</sup> With the static magnetic field parallel to the c axis, a pair of ENDOR lines were observed at 4.271 and 6.700 MHz when sitting on the next-to-lowest line in the central ESR spectrum (i.e., at 3320.4 G and 9.2890 GHz). The average of 5.486 MHz for these two ENDOR lines leaves no doubt that the nucleus is lithium. A second pair of ENDOR lines, thus far unidentified, were at 5.478 and 6.786 MHz.

An angular dependence study of the primary set of ESR lines, arising from defects with no <sup>29</sup>Si nucleus, was made in the plane perpendicular to the crystal's X axis (i.e., about a twofold symmetry axis). These results are shown in Fig. 2. For most paramagnetic defects in quartz, rotation of the magnetic field away from the c axis in the X plane causes each of the ESR lines to split into three components; however, in the case of the [SiO<sub>4</sub>/Li]<sup>0</sup> center, this rotation splits the lines into only two components (the solid curve being doubly degenerate in Fig. 2). This degeneracy requires that the [SiO<sub>4</sub>/Li]<sup>0</sup> center be symmetrical about a twofold axis of the crystal (i.e., the lithium interstitial ion lies on the twofold axis passing through the adjacent silicon ion having the large spin density. The ESR data, represented by the points in Fig. 2, were taken at 13 angles ranging from -67° to +70° and were fit to the following spin-Hamiltonian.

$$H = S g B + I A S - g_N N B I$$

Final values for the g and A matrices, obtained from diagonalizing the 8x8 Hamiltonian matrix, are listed in Table I along

with parameters from analogous germanium-associated centers in quartz. The root-mean-square deviation between the computer-generated and the measured line positions for the 86 lines used in our fitting was 0.068 MHz, which compares favorably with the 1.0-MHz experimental linewidths.

Figure 3 shows the results of a pulse-anneal experiment to determine the thermal stability of the  $[\text{SiO}_4/\text{Li}]^{\circ}$  centers. Each data point was taken at 77 K and represents the amount of ESR signal remaining after the sample was held at the indicated anneal temperature for five min. The defect has two decay steps, one near 109 K and the other near 187 K. We suggest that the lower-temperature step occurs when holes are released from other traps in the crystal and migrate to the  $[\text{SiO}_4/\text{Li}]^{\circ}$  centers. Because none survive the 187-K step, we suggest that it corresponds to the intrinsic decay of the  $[\text{SiO}_4/\text{Li}]^{\circ}$  centers. In a separate investigation, we have observed an intense thermoluminescence peak in the 180-190 K region which correlates with the ESR spectrum of the  $[\text{SiO}_4/\text{Li}]^{\circ}$  center.<sup>17</sup>

Our identification of the  $[\text{SiO}_4/\text{Li}]^{\circ}$  center as an extra electron trapped by an interstitial lithium ion in the otherwise perfect lattice is strongly supported by the unique nature of its formation conditions. We have found that these centers are formed by a two-step irradiation process, first at an intermediate temperature (between 150 and 300 K) and then at 77 K. This double irradiation is needed because of the conflicting requirements imposed by (1) the minimum temperature at which radiation can form "free" lithium ions in quartz and (2) the maximum tem

perature at which the  $[\text{SiO}_4/\text{Li}]^{\circ}$  centers remain stable. Past work has shown that interstitial lithium ions are located adjacent to substitutional aluminum ions in as-grown quartz,<sup>15</sup> and also that the lithium ions can be moved away from these trapping sites by ionizing radiation whenever the sample temperature is near or above 200 K.<sup>18</sup> Thus, the  $[\text{SiO}_4/\text{Li}]^{\circ}$  centers, which are only stable below 180 K, cannot be efficiently formed by the same irradiation that moves lithium ions away from the aluminum sites. In practice, an as-grown sample must be irradiated at the intermediate temperature to release the lithium ions from their aluminum traps, then immediately cooled to 77 K before the lithium ion can diffuse to another impurity or defect site, and finally irradiated at 77 K to form the  $[\text{SiO}_4/\text{Li}]^{\circ}$  center.

The solid curve in Fig. 4 shows how the production of  $[\text{SiO}_4/\text{Li}]^{\circ}$  centers depends on the temperature of the intermediate irradiation. Each data point represents the concentration of these centers after a double irradiation, first at the indicated intermediate temperature and then at 77 K. Following each double-irradiation step, the sample was heated to 300 K before continuing to the next intermediate temperature. For comparison, the dashed curve in Fig. 4 illustrates the temperature dependence of  $[\text{AlO}_4]^{\circ}$  center formation in quartz, which as shown in Reference 18 is directly related to the radiation-induced dissociation of the lithium-aluminum pair. It is clear from Fig. 4 that the phenomena represented by the two curves are related. For example, the formation of  $[\text{SiO}_4/\text{Li}]^{\circ}$  centers reaches a maximum at the maximum slope of the dissociation curve. At temperatures above 250 K, the

lithium ions have sufficient thermal energy to diffuse to more stable trapping sites and the production of  $[\text{SiO}_4/\text{Li}]^0$  centers decreases.

In summary, we have observed a new defect in quartz wherein an extra electron is trapped by an alkali ion. From the production criteria and hyperfine splittings, we show that the extra electron is trapped primarily at a four-coordinated silicon ion with the adjacent interstitial lithium ion providing stability. Furthermore, we suggest that defects of this same type should be formed in silica and in the oxide interface regions of silicon devices, although their stability is not expected to extend to room temperature. Most importantly, the simplicity of this new center in quartz should provide the insight necessary to develop models of the more complex alkali-electron traps present at room temperature in all forms of  $\text{SiO}_2$ . In this latter regard, if two  $[\text{SiO}_4/\text{Li}]^0$  centers were to be formed simultaneously about a common silicon ion during room-temperature irradiation, then a diamagnetic center would result and its thermal stability might be significantly greater than one  $[\text{SiO}_4/\text{Li}]^0$  center alone. This would represent an effective negative-U behavior. Then, when the diamagnetic center thermally decays by releasing an electron, the remaining center would immediately become unstable and release the second electron.

Acknowledgements The authors wish to thank E. E. Kohnke for his encouragement to pursue this problem, T. M. Wilson for helpful discussions, and Thermo-Dynamics for providing the quartz. Dr. A. Halperin was on leave from the Racah Institute of Physics, The

Hebrew University of Jerusalem.

#### References

1. E. J. Friebale and D. L. Griscom, in Treatise on Materials Science and Technology, edited by M. Tomozawa and R. H. Doremus (Academic Press, New York, 1979), Vol. 17, pp. 257-351.
2. J. A. Weil, *Phys. Chem. Minerals* 10, 149 (1984).
3. L. E. Halliburton, *Cryst. Latt. Def. and Amorph. Mat.* 12, 163 (1985).
4. J. Robertson, *Adv. Phys.* 32, 361 (1983).
5. P. W. Anderson, *Phys. Rev. Lett.* 34, 953 (1975).
6. G. D. Watkins and J. R. Troxell, *Phys. Rev. Lett.* 44, 593 (1980).
7. J. Bourgoin and M. Lannoo, Point Defects in Semiconductors II (Springer-Verlag, Berlin, 1983).
8. J. Isoya, J. A. Weil, and P. H. Davis, *J. Phys. Chem. Solids* 44, 335 (1978).
9. J. H. Anderson and J. A. Weil, *J. Chem. Phys.* 31, 427 (1959).
10. J. H. Mackey, *J. Chem. Phys.* 39, 74 (1963).
11. Y. Haven, A. Kats, and J. S. van Wieringen, *Philips Res. Repts.* 21, 446 (1966).
12. P. H. Davis and J. A. Weil, *J. Phys. Chem. Solids* 39, 775 (1978).
13. M. G. Jani, R. B. Bossoli, and L. E. Halliburton, *Phys. Rev. B* 27, 2285 (1983).
14. R. B. Bossoli, M. G. Jani, and L. E. Halliburton, *Solid State Commun.* 44, 213 (1982).

15. J. J. Martin, J. Appl. Phys. 56, 2536 (1984).
16. See Reference 13 for experimental details.
17. A. Halperin, M. G. Jani, and L. E. Halliburton (private communication).
18. M. E. Markes and L. E. Halliburton, J. Appl. Phys. 50, 8172 (1979).

Table I. Spin-Hamiltonian parameters for the  $[\text{SiO}_4/\text{Li}]^{\circ}$  center and related defects in quartz. In specifying the principal axes' directions,  $\Theta$  is the polar angle (relative to +Z) and  $\Phi$  is the azimuthal angle (relative to +X with positive rotation being from +X to +Y). Estimates of errors in the present work are  $g = 0.00003$ ,  $A = 0.05$  MHz, and  $\Theta$  and  $\Phi = 1^{\circ}$ .

Center	Matrix	Principal values	Principal directions		Reference
			$\Theta$	$\Phi$	
$[\text{SiO}_4/\text{Li}]^{\circ}$	$g$	1.99899 2.00074 2.00166	$25^{\circ}$ $90^{\circ}$ $65^{\circ}$	$270^{\circ}$ $0^{\circ}$ $90^{\circ}$	present work
	$A(^7\text{Li})$	2.49 MHz 2.75 MHz 4.11 MHz	$1^{\circ}$ $89^{\circ}$ $90^{\circ}$	$270^{\circ}$ $90^{\circ}$ $0^{\circ}$	present work
$\text{Ge(II)}$	$g$	1.9929 2.0001 2.0007	$159^{\circ}$ $90^{\circ}$ $69^{\circ}$	$90^{\circ}$ $0^{\circ}$ $90^{\circ}$	a
$[\text{GeO}_4(\text{A})/\text{Li}^+]^{\circ}$	$g$	1.9907 2.0003 2.0019	$25^{\circ}$ $90^{\circ}$ $65^{\circ}$	$90^{\circ}$ $0^{\circ}$ $270^{\circ}$	b

<sup>a</sup>J. Isoya, J. A. Weil, and R. F. C. Claridge, J. Chem. Phys. 69, 4876 ((1978).

<sup>b</sup>Reference 10.

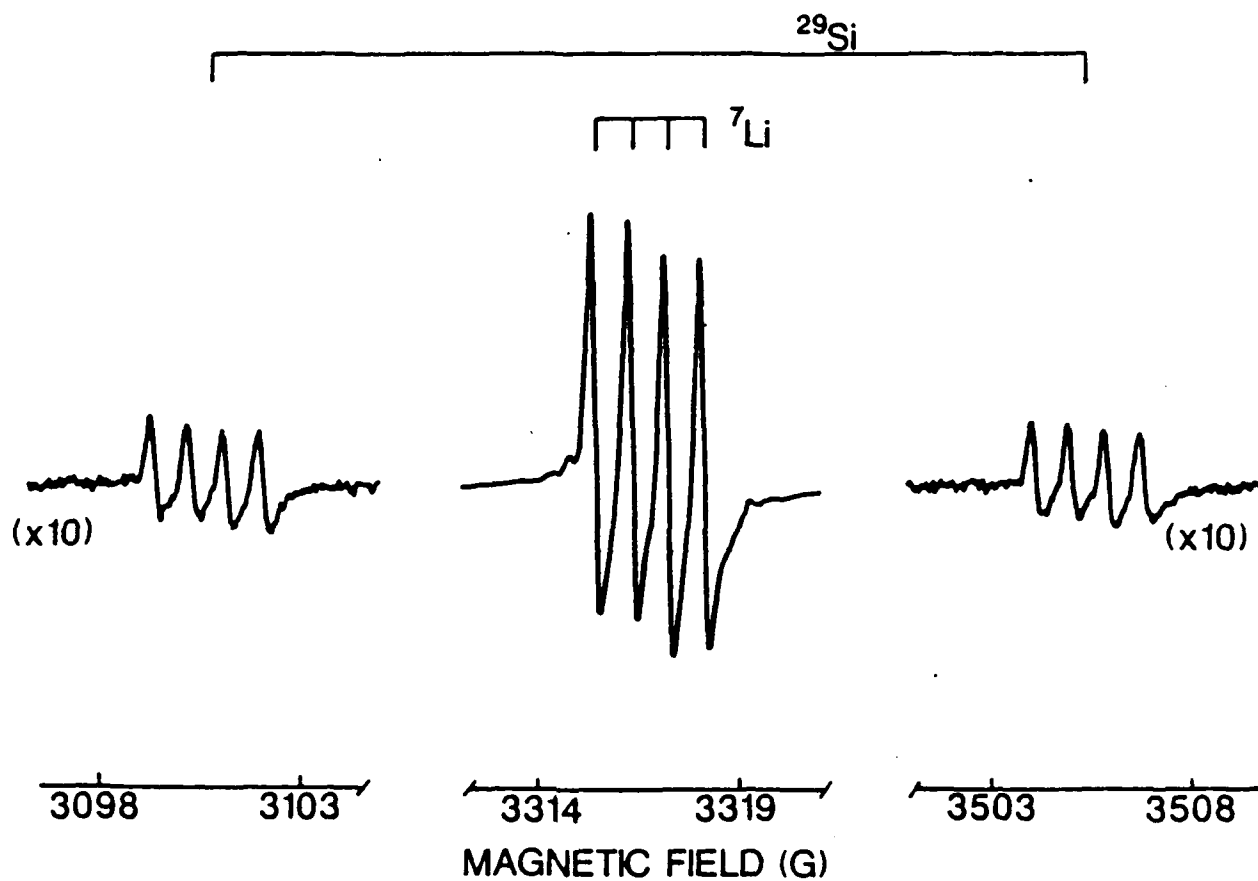


Figure 1. ESR spectrum of the  $[\text{SiO}_4/\text{Li}]^0$  center. These data were taken at 77 K with the magnetic field parallel to the crystal's c axis. The gain was increased by a factor of ten when recording the two outer sets of four lines.

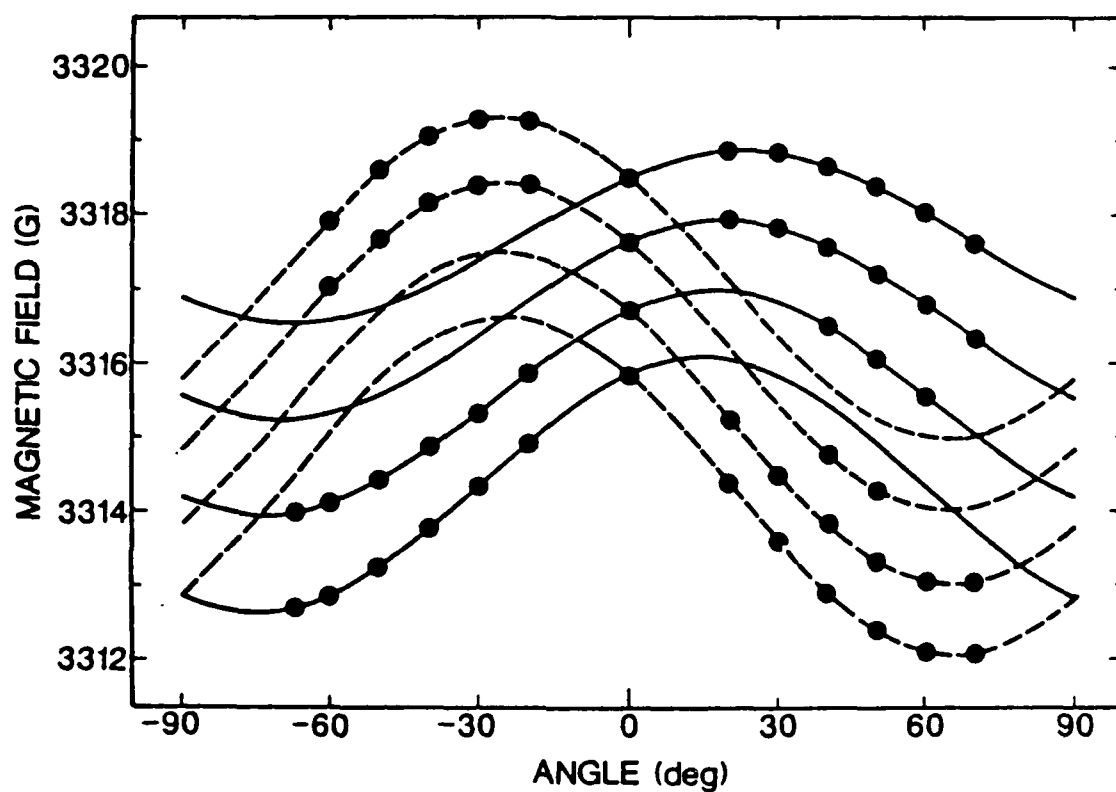


Figure 2. Angular dependence of the central ESR spectrum for rotation of the magnetic field in the X plane. The points are experimental data, while the dashed and solid (doubly degenerate) curves were computer-generated from the parameters given in Table I.



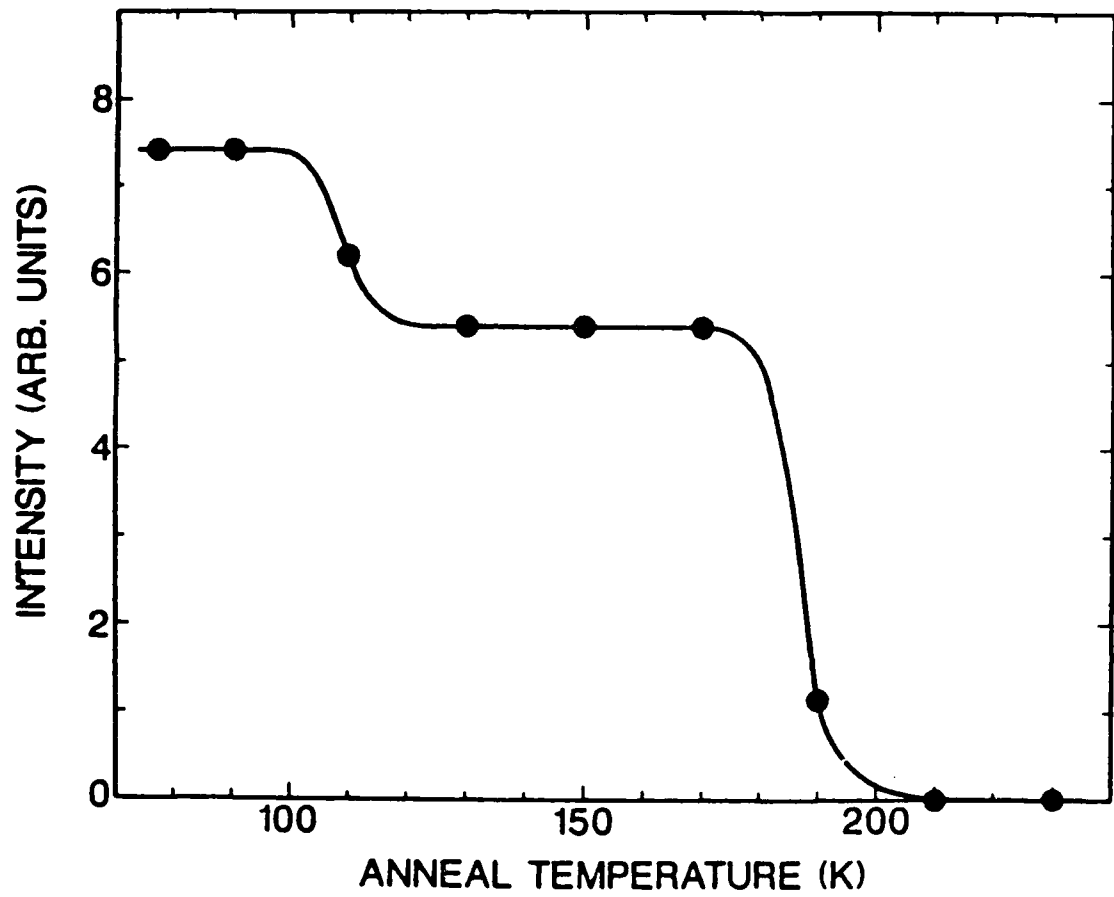


Figure 3. Thermal anneal behavior of the  $[\text{SiO}_4/\text{Li}]^0$  center. Each data point was taken at 77 K after holding the sample at the indicated anneal temperature for five min.

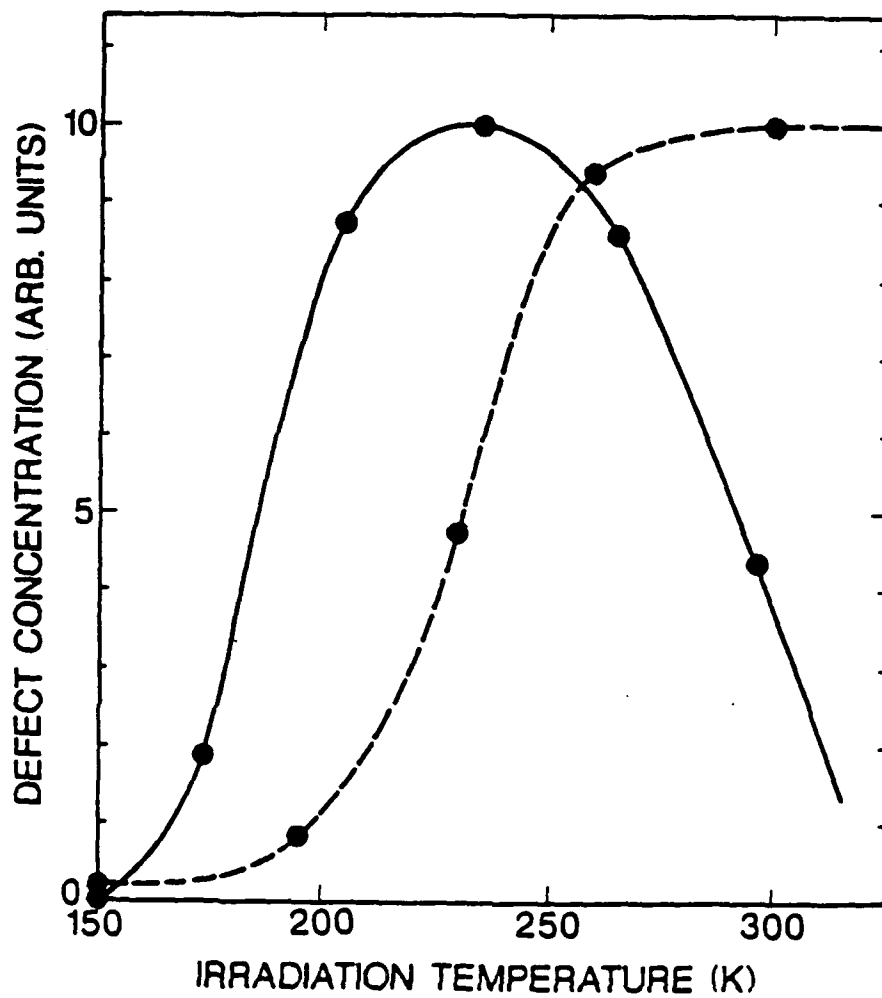


Figure 4. The formation curve (solid line) for the  $[\text{SiO}_4/\text{Li}]^0$  center illustrates the dependence on the temperature of the intermediate irradiation. The dashed curve, consisting of normalized data taken from Fig. 9 in Reference 18, shows the temperature dependence of the radiation-induced dissociation of alkali ions from aluminum.

## F. Evaluation of RADC Grown Material

We have completed the project of measuring the room temperature mechanical  $Q$  of nominal 5 MHz 5th overtone AT-cut "Warner design"<sup>1</sup> resonator blanks grown for RADC by Motorola. The original samples were seven sets of unfinished discs nominally cut to the AT-angle sent to us by RADC. Initially two sets were sequentially sent to KW Mfg. (Prague, OK) for fabrication into contoured-polished blanks. Since delivery was slow and the finish was not as good as their previous work the remaining sets were sent sequentially to Piezo Crystal Co. (Carlisle, PA). The mechanical  $Q$  at room temperature was measured using the log-decrement method with the sample mounted in a gap holder. The gap holder was located in a small test chamber that was held under vacuum. We do not expect that the  $Q$  was limited by the measuring technique since we use the same method for many of our temperature dependent measurements and we routinely observe mechanical  $Q$  values greater than 10 million at low temperatures. Table 1 gives the average room temperature mechanical  $Q$  values for the seven sets of samples. Most of the averages were obtained by using five or more samples. Only three blanks were available for GC24S, the swept material. Only two and three of the five blanks in the GC6 and GC7 sets respectively worked well. The table also gives the average resonant frequency the angle at which the blank had been cut by the original fabricator. It should be noted that several of the sets were cut near  $34^\circ$  rather than the  $35^\circ + AT$  angle. It is not known if this angular deviation affects the  $Q$  value; these "off-angle" blanks did show some interfering mode problems.

Table 1. Room temperature mechanical Q's.

Sample	f(MHz)	Q(x10 <sup>6</sup> )	Angle	Q'(x10 <sup>6</sup> )	Q(opt)	Al(ppm)
GC2-48(7)	5.326	1.94	35°31'	2.18	2.84	
GC6-21(2)	5.632	1.34	34°01'	1.51	1.94	
GC7-48(3)	5.190	1.31	35°34'	1.31	1.31	
GC9 (5)	5.667	1.20	34°01'	1.36	2.57	
GC18(5)	5.629	2.31	-----	2.60	2.13	0.5
GC24(5)	5.624	2.05	35°34'	2.31	2.52	0.9
GC24S(3)	5.627	2.32	-----	2.61	3.40	
PQ-E(5)	4.675	2.22	-----	2.08	----	

The numbers in parentheses give the number of blanks tested.

The mechanical Q of blanks taken from our own Sawyer Premium Q bar designated PQ-E are included for comparison. The optical Q is for the GC-series blanks; and the Al content is given for the GC-18 and GC-24 blanks<sup>1</sup>.

The mechanical Q of a crystal at a given temperature is determined by the various loss mechanism that are operating. At room temperature we expect that the mechanisms are the intrinsic loss due to the interaction between the AT-thickness shear vibration and the thermal phonons plus Debye-like anharmonic losses due to point defects. Since the losses are assumed to be additive we should be able to write

$$1/Q = 1/Q_i + 1/Q_d$$

where  $1/Q_i$  stands for the intrinsic loss and  $1/Q_d$  stands for the loss due to defects. The intrinsic loss is proportional to the frequency<sup>2,3</sup>; consequently if it is the only mechanism present we can scale the Q values to the "standard" 5 MHz frequency. The Q' values given in Table 1 are the "scaled" Q values obtained by multiplying the Q by the ratio  $f(\text{MHz})/5$ . This operation is probably reasonable for the high Q samples but is not valid for the lower Q samples. We believe that most likely a "defect" mechanism such as the 340 K Na-related and 305 K Li-related loss

peaks reported by Martin, Hwang and Bahadur<sup>4</sup> is present in the lower Q crystals. Temperature dependent measurements are necessary to determine if the room temperature mechanical Q is limited by such point defects.

IR absorption spectra were taken on one blank from each of the seven sets of samples. The polished-contoured blanks were mounted in our optical dewar with the X-axis in the vertical direction. Figures 1 and 2 show the resulting spectra along with one of our own blanks taken from Premium Q bar PQ-E. The samples GC18, GC24, and GC24S which have the highest mechanical Q show the cleanest IR spectra while GC9 which has the lowest Q shows the dirtiest spectrum. The curve for GC24S shows a very small Al-OH band indicating that this sample has a very low Al content.

As part of this project we have performed evaluation tests for the aluminum content in quartz grown by RADC. Aluminum is a pervasive and active impurity in all quartz, and its content is a good indicator of the quality of a quartz bar. The aluminum content was measured by the method described by Markes and Halliburton<sup>5</sup>. Table 2 summarizes these aluminum determinations.

1. A. F. Armington, private communication, (1985).
2. A. W. Warner, Bell Syst. Tech. J. 40, 1193(1960).
3. D. B. Fraser, Physical Acoustics, edited by W. P. Mason (Academic Press, New York, 1968), Vol. V. Chap. 2.
4. J. J. Martin, Ho. B. Hwang, and H. Bahadur, Proc. of the 39th Annual Symposium on Frequency Control, p266 (1985).
5. M. Markes and L. E. Halliburton, J. Appl. Phys. 50, 8172 (1979).

TABLE 2. Summary of Quartz Analyses done at Oklahoma State University for RADC during 1984 and 1985.

SAMPLE	AL CONTENT (ppm)	COMMENTS
X46A	0.3	
X49	1.9	
X51X	19.2	one end (25%) black
X52X	0.13	
X54Z	2.8	
X55B	0.03	
X55T	0.05	
X61B	3.8	
X61B (2nd attempt)	0.22	
X64T	0.06	
X66	1.6	
X67B	0.11	
X70	15.1	25% x-growth
X71B	0.28	
X72	4.01	no indication of vanadium
X76	1.01	
X78	0.19	
X79	2.30	
QA30X	2.4	
QA31X	5.9	one end (25%) black
QA32	32.0	totally black
QA33Z	0.42	
QA34	1.75	
QA35Z	8.1	
QA36X	2.5	
QA36Z	16.6	one end (10%) black
QA37T	0.6	
QA38B	8.7	
QA39B	0.05	
QA40B	0.2	
QA46M	0.19	
QA48	0.96	
QA49B	0.15	
QA50B	0.07	
QA51B	0.077	
QA52T	0.64	
QC 13-19 (T3-1)	11.0	
QC 12-7 (T1-2)	7.2	
QP19	1.7	
QP20	10.9	one end (10%) black
QP22	1.0	
QP24	0.70	
QP25	0.51	no indication of iron
QP26	29.7	
T-1-7	30.2	

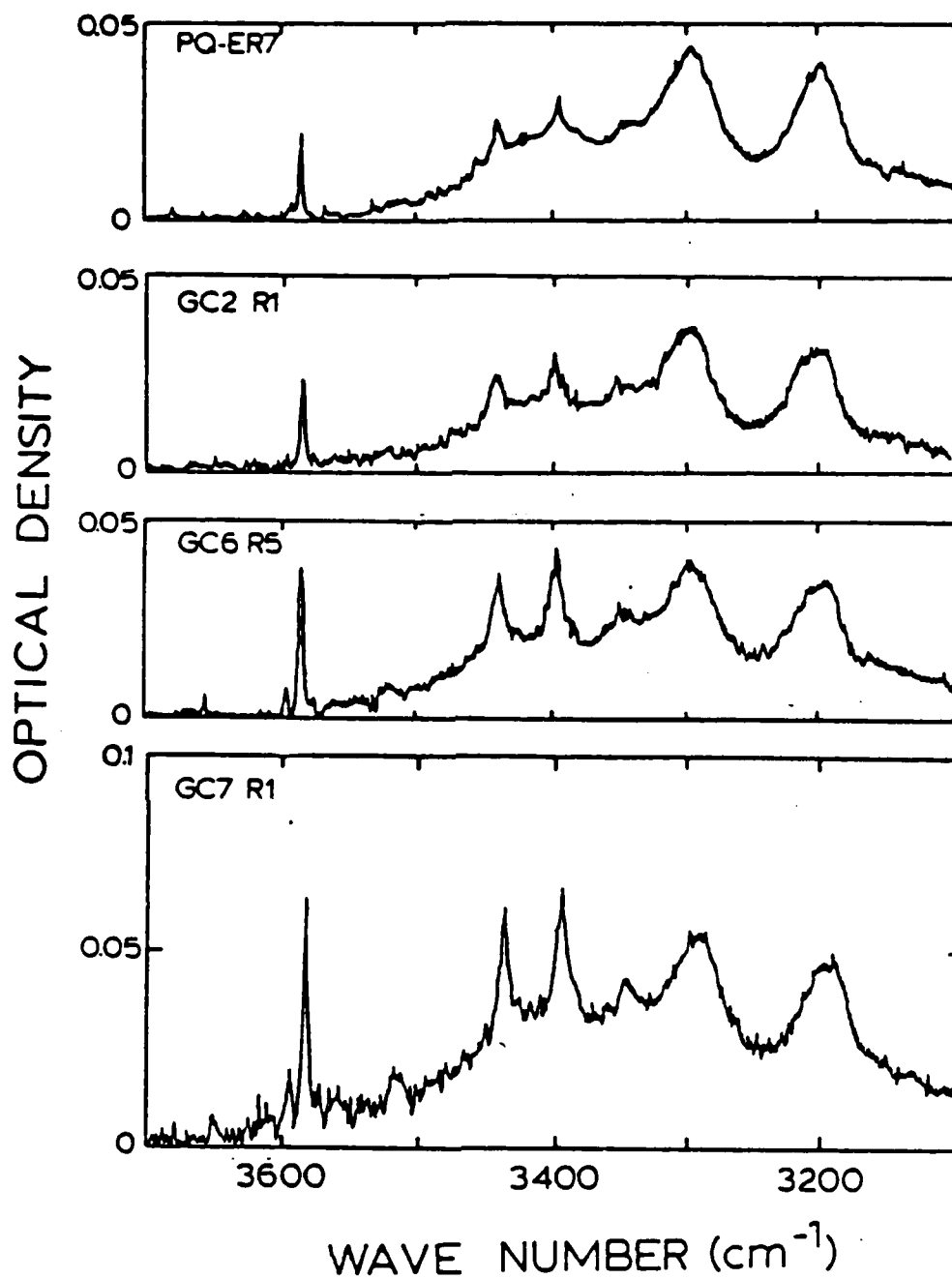


Fig. 1. The low temperature IR absorption spectra of three of the seven sets of blanks are shown. The spectrum of our own PQ-E sample is included for comparison.

## G. LIST OF PAPERS, PRESENTATIONS, AND THESES

The following quartz-related papers, and theses resulted from the research performed at Oklahoma State University under this contract.

### 1. Papers (in journals).

J. J. Martin, ALUMINUM RELATED ACOUSTIC LOSS IN AT-CUT QUARTZ CRYSTALS, J. Appl. Phys., 56, 2536 (1984).

L. E. Halliburton, M. G. Jani, and R. B. Bossoli, ELECTRON SPIN RESONANCE AND OPTICAL STUDIES OF OXYGEN VACANCY CENTERS IN QUARTZ, Nucl. Instrum. Methods B1, 344 (1984).

B. Subramaniam, L. E. Halliburton, and J. J. Martin, RADIATION EFFECTS IN CRYSTALLINE SiO<sub>2</sub>: INFRARED ABSORPTION FROM OH<sup>-</sup>-RELATED DEFECTS, J. Phys. Chem. Solids 45, 575 (1984).

M. G. Jani and L. E. Halliburton, POINT DEFECTS IN NEUTRON-IRRADIATED QUARTZ, J. Appl. Phys. 56, 942 (1984).

L. E. Halliburton, DEFECT MODELS AND RADIATION DAMAGE MECHANISMS IN ALPHA-QUARTZ, Cryst. Latt. Def. and Amorph. Mat. 12, 163 (1985).

### 2. Conference Proceedings.

Augusto R. Lopez, J. D. West, and J. J. Martin, ELECTRODIFFUSION OF IONS IN ALPHA-QUARTZ in MRS Proceedings: Defect Properties and Processing of High-Technology Non-Metallic Materials, Vol. 24, in press.

J. J. Martin, Ho B. Hwang, and H. Bahadur, RADIATION EFFECTS IN THE ACOUSTIC LOSS SPECTRA OF AT-CUT QUARTZ CRYSTALS, Proc. 39th Annual Symposium on Frequency Control, p266 (1985).

J. J. Martin, ALUMINUM-RELATED ACOUSTIC LOSS IN AT-CUT QUARTZ CRYSTALS, Proc. 38th Annual Symposium on Frequency Control, p16 (1984).

### 3. Theses (at Oklahoma State University).

Ho B. Hwang, "Radiation Effects in the Acoustic Loss Spectra of AT-Cut Toyo Quartz Crystals," M. S. May, 1985.

Jerry Doug West, "Electrodifffusion of Lithium, Sodium and Hydrogen Ions in Synthetic Quartz," M. S. July, 1984.

Gary E. A. Berman, "Radiation-Induced Acoustic Loss in Quartz Crystals," M. S. May, 1984.

B. L. Mihura, "Oxygen Divacancy Model for the 'E' Centers in



Crystalline SiO<sub>2</sub>," M. S. May 1984.

C. Y. Chen, "Electron Spin Resonance of Point Defects in Quartz,"

Ph. D. Dec. 1985.

# I. PROPERTIES OF FLUORIDE GLASS MATERIALS USEFUL FOR FIBERS AND LASER HOSTS

by

William A. Sibley and Richard C. Powell

## A. Introduction

The research on optical properties of heavy metal fluoride glasses and oxide glasses with an eye toward their use in optical communications and laser hosts has made remarkable progress over the last several years. The work has involved very practical aspects such as the production of new laser systems and important fundamental research on the site positions and the bonding of impurity ions in these glasses. The heavy metal fluoride glass materials containing zirconium fluoride, hafnium fluoride and barium/thorium fluoride have been investigated. All of these materials have excellent properties. There are, of course, some areas of concern such as radiation effects. There are also some areas of great excitement such as the possibility as using them for up-conversion. In each case, progress has been made. We are looking forward to continuing progress on the upconversion project. Perhaps the area of greatest importance is holographic gratings produced by four wave mixing techniques in these materials. Professor Powell has made a study of oxide materials which has been extremely fruitful. This work continues on a selected list of fluoride glasses. In the area of optical impurity research and radiation damage work it is been known for some time the optical properties of glasses have been an important topic of continuing interest.

## B. Heavy Metal Fluoride Glasses

### 1. Introduction

The optical properties of glasses have been an important topic of continuing interest. Considerable literature has recently emerged concerning the structure, optical, mechanical, thermal, and electrical properties of these materials. [1-10] Several excellent review papers have been written on heavy metal fluoride glasses. [7-9] The high optical transparency which stretches from  $0.25\mu\text{m}$  in the ultraviolet to  $8\mu\text{m}$  in the mid-infrared and the easy incorporation of various impurities such as rare earth and transition metal ions make heavy metal fluoride glass of interest for potential use

as multi-spectral optical components, IR fiber optics materials, IR laser windows and laser host materials. [10-11] Much of the work on the optical and physical characteristics of these heavy metal fluoride glasses has centered on fluorozirconate and fluorohafnate glasses in which  $ZrF_4$  or  $HfF_4$  is the primary constituent. Recently, however, the synthesis of multicomponent composition glass based on fluorides of Th, Ba, Zn and heavy metals such as Yb or Lu has been reported. [12,13] Table I provides the composition of the glasses of interest in this paper.

Table I  
Batch compositions (mole%) of some heavy-metal fluoride glasses.

Glass	BaF <sub>2</sub>	ZnF <sub>2</sub>	YbF <sub>3</sub>	ThF <sub>4</sub>	NaF	LuF <sub>3</sub>	ZrF <sub>4</sub>	LaF <sub>3</sub>	AlF <sub>3</sub>	HfF <sub>4</sub>
BZYT	19	27	27	27						
BZYTn	14	27	27	27	5					
BZYTL	19	27	10	27		17				
BZYTLN	14	27	10	27	5	17				
ZBL	33						62	5		
ZBLA	36						57	3	4	
HBL	33							9		58

These new materials are of special interest because they offer extended infrared transmission and improved chemical durability. The purpose of this paper is to review the feasibility of utilizing these materials in light guide applications. Special emphasis will be given to radiation damage properties and the utilization of heavy metal fluoride glasses as optical device materials.

## II. LIGHT GUIDE MATERIALS

Long distance transmission of optical information has been made possible by the production of optical fibers with very low impurity concentrations which operate in the mid infrared range from 2-10  $\mu\text{m}$ . In the case of high power transmission for distances of only a few hundred meters losses of tenths of db/km can be tolerated. On the other hand for long distance communication ultra low losses of the order of  $10^{-2}$  db/km are desired. Figure 1 illustrates some of the constraints on the materials of choice. Notice that Rayleigh scattering is the loss mechanism in the visible region of the spectrum but decreases rapidly in importance in the infrared. Rayleigh scattering is proportional to  $\lambda^{-4}$  and losses below  $10^{-3}$  db/km are predicted for the 3-10  $\mu\text{m}$  region. Similarly, electronic transitions can be avoided by utilizing materials which have a large band gap.

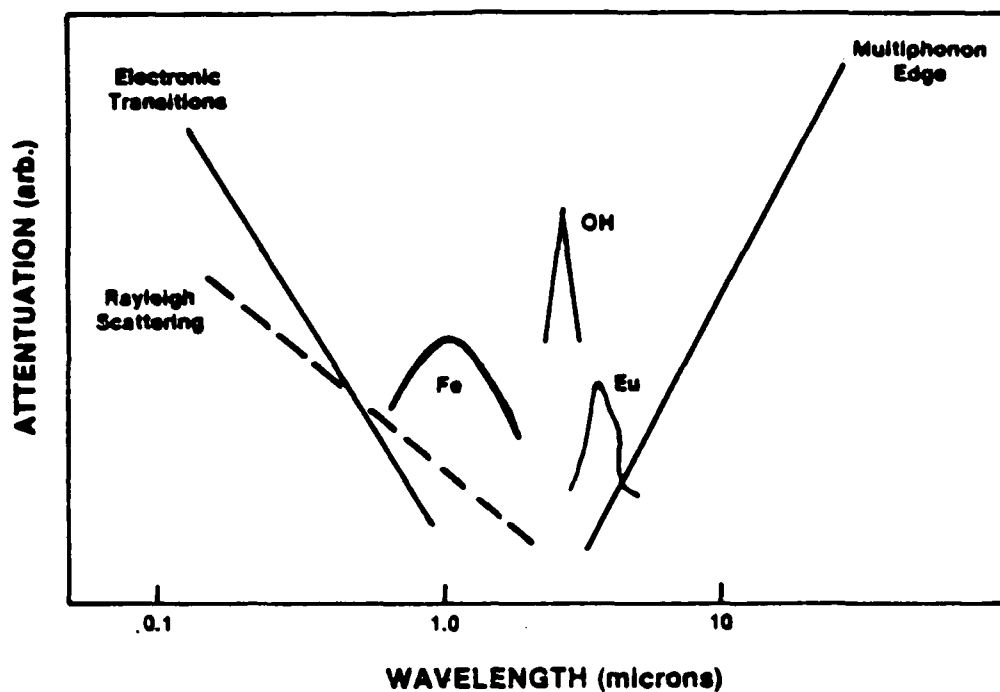


Figure 1

Loss mechanisms for infrared transmission.[8]

Optical absorption by impurities such as Fe, Eu or  $\text{OH}^-$  can also be reduced through the reduction of impurities or special treatment. The multiphonon edge in the infrared is particularly important. Of course, in the mid infrared Rayleigh scattering is low and transition metal ion impurity absorption decreases; therefore, materials with long wavelength multiphonon transitions are more ideally suited for long range communication. Figure 2, which is schematic of the optical transparency of materials such as halide glasses or single crystal KCl, illustrates this point. It is evident that the heavy metal halide glasses with an intrinsic loss of  $10^{-3}$  db/km at  $3\mu\text{m}$  are an excellent choice for long range optical transmission.[7,8]

One possible negative aspect of this type of material for optical transmission is radiation damage. Previous work by Halliburton, Griscom, Friebele, Tanimura and their collaborators [14-19], has shown that these materials damage much like alkali halide materials. That is the photochemical damage mechanism is prevalent and the materials are highly sensitive to ionizing radiation. The optical absorption induced by a dose of  $10^{16}$  MeV/cm<sup>3</sup> ionizing radiation in two types of heavy metal fluoride glasses is portrayed in Figure 3. The long tail associated with the zirconium base fluoride glass which extends from 500 nm into the infrared is due to the production of  $\text{Zr}^{3+}$  defects in this material by radiation. This absorption extends to  $2\mu\text{m}$  and can be as high as  $10^3$  db/km.

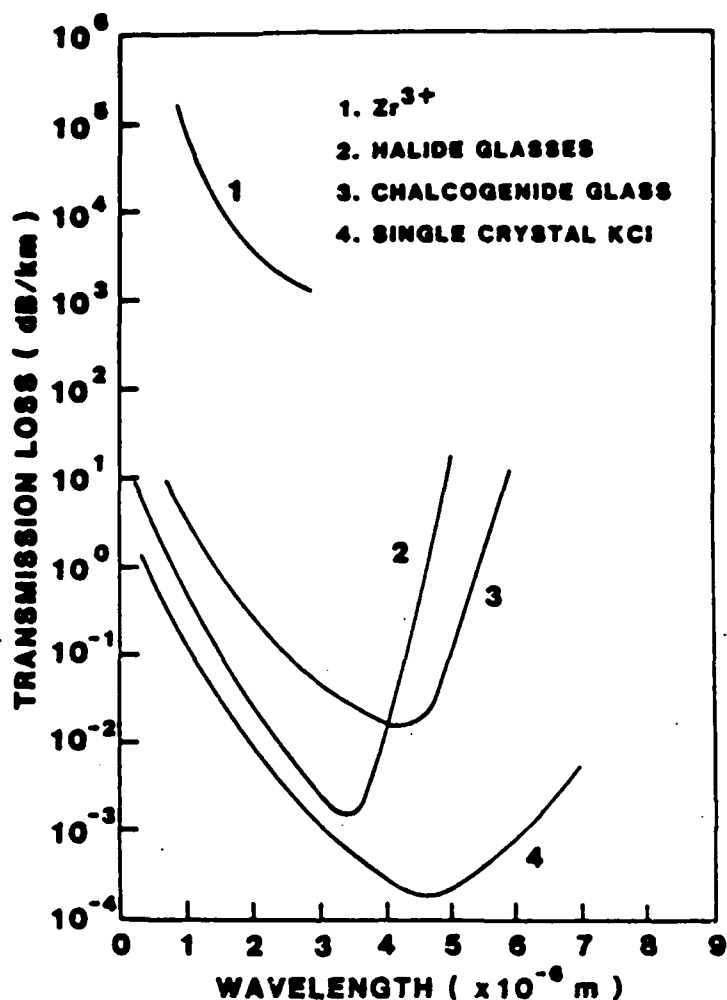


Figure 2

Predicted IR loss spectrum for various glasses and KCl single crystal.

The  $\text{BaF}_2/\text{ThF}_4$  base glass seems to be much less affected by radiation and the absence of zirconium or hafnium means that there is no deleterious radiation induced infrared absorption in this glass. Annealing of the radiation damage occurs in both types of materials. This is shown in Figure 4. Notice that the  $\text{BaF}_2/\text{ThF}_4$  glass recovers from radiation damage at a much lower temperature than the fluorozirconate glass. For low temperature radiation, both types of glasses are sensitive to ionizing radiation and considerable absorption is produced. Nonetheless, it does appear that both types of glasses are very useful for long range data transmission with the  $\text{BaF}_2/\text{ThF}_2$  base glass having an advantage as far as radiation damage is concerned.

These glasses are in many cases grown in or treated with Cl vapor in order to reduce the OH<sup>-</sup> absorption in the infrared. Cases et.al. [15] and Griscom and Tran [16] were the first to discover that such a treatment resulted in chlorine being present in

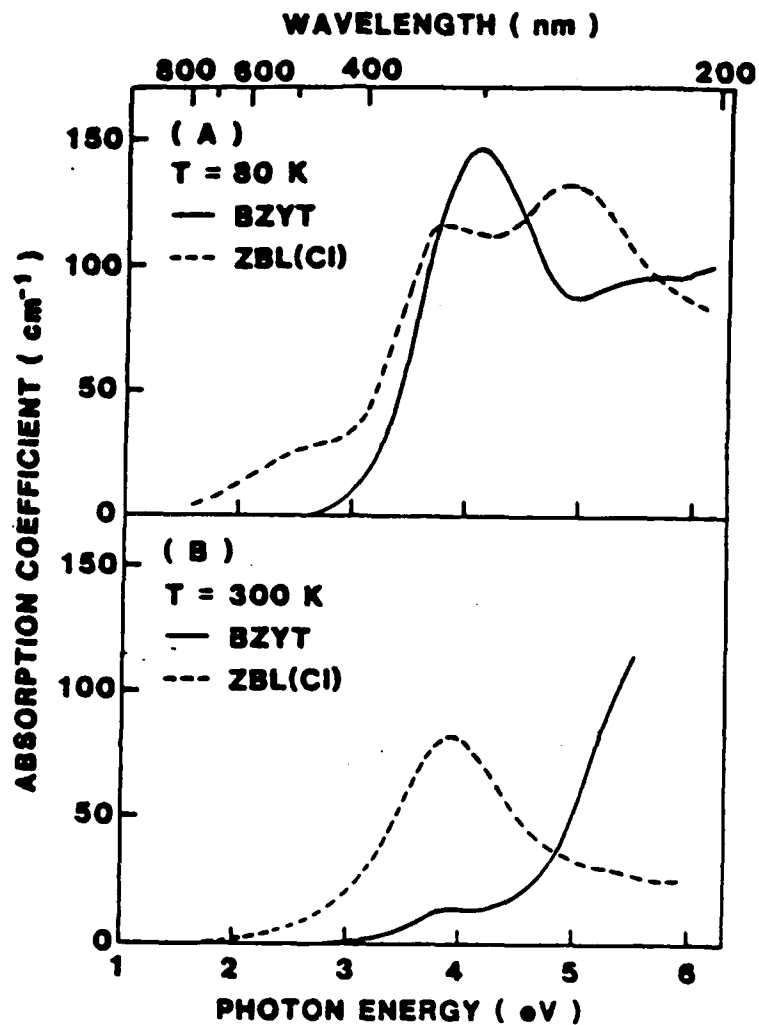


Figure 3  
Optical absorption spectra of BZYT and ZBL(Cl) glasses after 1.7 MeV electron irradiation ( $10^{16} \text{MeV/cm}^3$ ) at 80K and 300K.

the glass in high concentration and Tanimura, et. al. [19] by combining electron spin resonance measurements and optical measurements with chemical analysis were able to show that as much as 2-5 weight percent of chlorine could be incorporated in the fluorozirconate glasses. Figure 5 illustrates the ESR spectrum of  $\text{Cl}_2^-$  centers produced by radiation in the fluorozirconate glass. Since this was discovered it has been possible for Drexhage and Suscavage at the Rome Air Development Center at Hanscom field to produce glass which is essentially chlorine free.

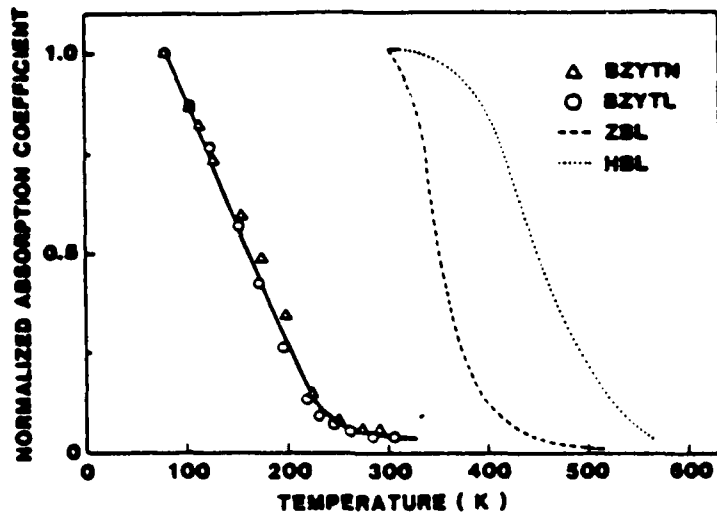


Figure 4

Annealing of the radiation induced 302 nm absorption band in BZYTn and BZYTL and the 325 nm band in ZBL and HBL. The samples were held at the desired temperature for 10 min. and then rapidly cooled to 80K for BZYTn and BZYTL and to 300K for HBL and ZBL.

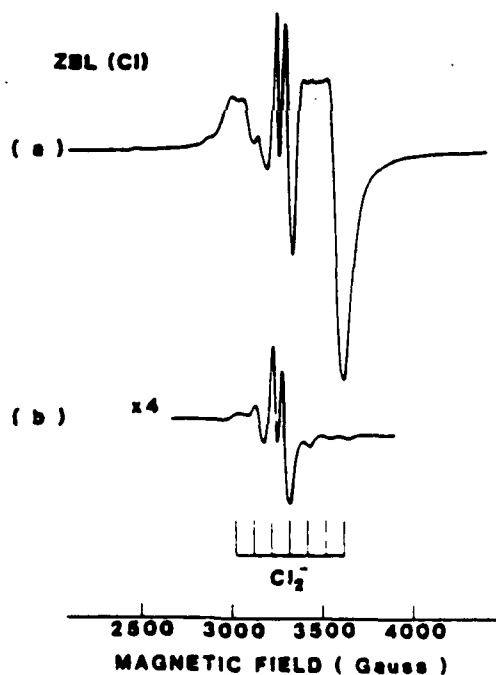


Figure 5

Radiation induced ESR spectra for ZBL(Cl) irradiated and measured at 77K (a), and annealed at 420K (b). The vertical lines are the theoretical peak positions for  $\text{Cl}_2^-$  centers obtained by Griscom and Tran [16, 19]

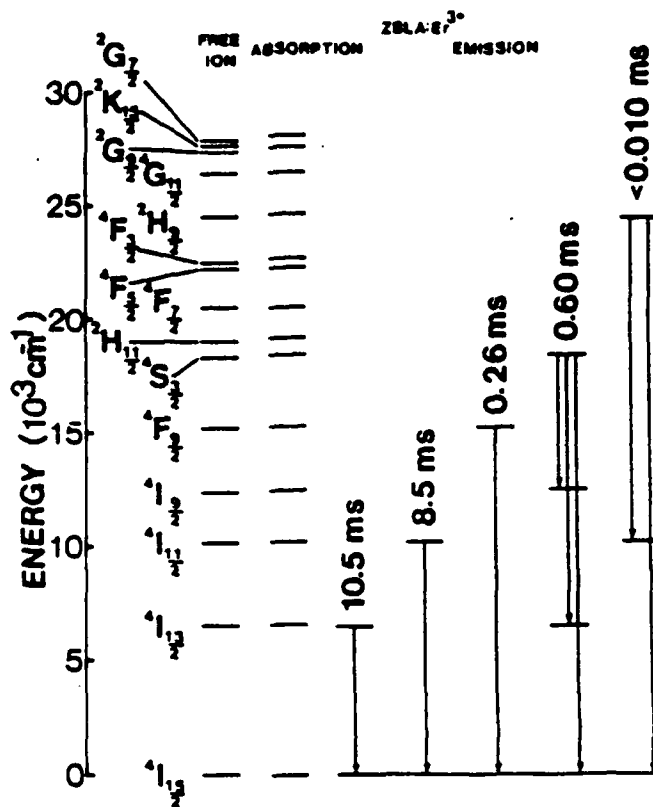


Figure 6  
Energy levels and transitions for  $\text{Er}^{3+}$ .

### III. DEVICE MATERIALS

Glass has always been a favorite device material. It is easily fabricated and reasonably inexpensive. In particular, the properties of fluoride glass, because of the wide range of transparency and easy incorporation of impurities make this glass a great possibility for future communication devices. If it were possible to develop glasses compatible with light guides which can sustain optical gratings and act as laser sources, then an excellent monolithic system would be available. Therefore, it is important to investigate the optical properties of various impurity ions such as the rare earth and transitional metal ions in these glass hosts.

In order to investigate the optical properties of these materials, a series of rare earth ions have been incorporated into the material. [1,3,20,21,22,23] Figures 5,7 and 8 illustrate the energy level diagrams for the impurities of  $\text{Er}^{3+}$ ,  $\text{Pr}^{3+}$  [20], and  $\text{Nd}^{3+}$  and the optical transitions that occur between these energy levels.



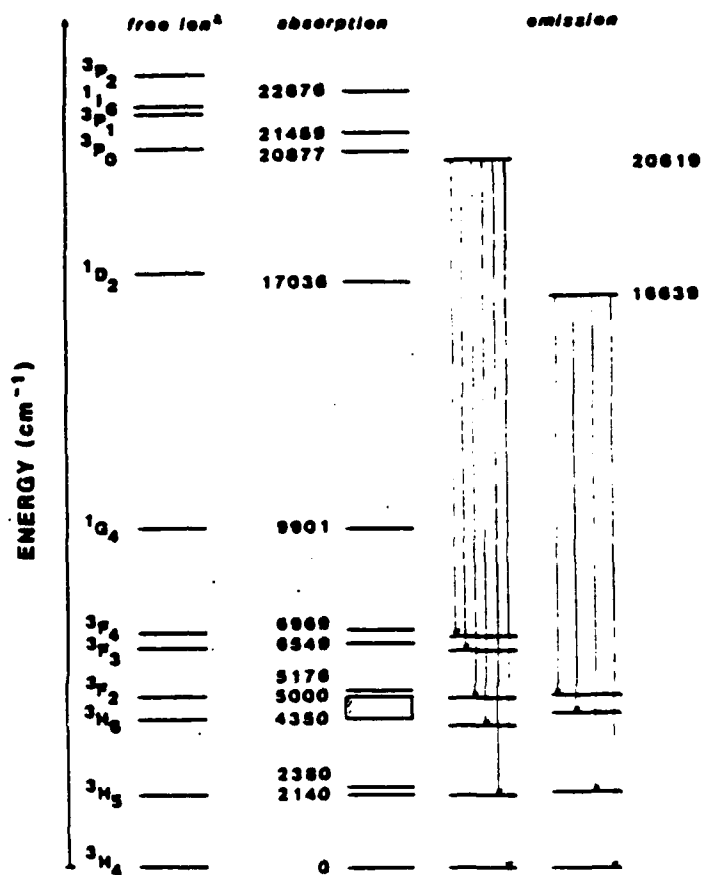


Figure 7  
Energy levels and transitions for Pr<sup>3+</sup>.

Of course for practical applications, room temperature operation of a system is necessary and it is important to evaluate the various loss mechanisms for optical transitions as a function of temperature. Weber showed that optical absorption and emission data can be utilized to calculate, using the Judd-Ofelt technique, the forced electric dipole transitions which occur due to the admixing of odd parity terms of higher energy configurations and by perturbations due to the host stark field [9]. The data and calculations are then used to examine the radiative and nonradiative rates under the assumption of no energy transfer. In particular we have investigated the optical properties of the rare earth ions, Er<sup>3+</sup> [3, 22], Ho<sup>3+</sup> [21] and Pr<sup>3+</sup> [20] in this manner. For example, in the case of Er<sup>3+</sup> in fluorozirconate glass, Figure 9 provides information from which the calculation of multiphonon transitions can be made.

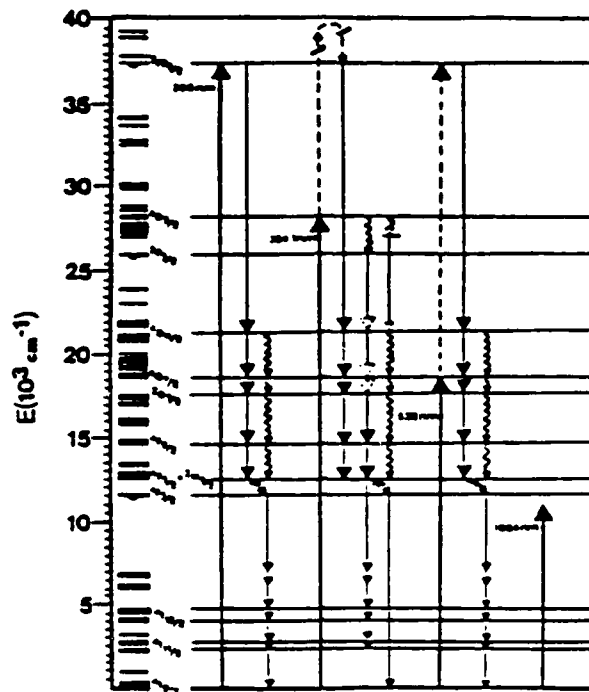


Figure 8  
Energy levels and transitions for Nd<sup>3+</sup>.

This figure illustrates the temperature dependence of the emission lifetime for the various Er<sup>3+</sup> transitions in Figure 6. The circles are for data taken on a material with 0.5 mole % ErF<sub>3</sub>, whereas the x's represent data taken for materials with 2 mole % ErF<sub>3</sub>. Notice that energy transfer does occur for the 2 mole % case which is why the emission lifetime from the <sup>4</sup>I<sub>13/2</sub> level to the <sup>4</sup>I<sub>15/2</sub> level is much shorter than that for the 0.5 mole % glass. The decrease in lifetime and intensity with increasing temperature for the sample containing 0.5 mole % ErF<sub>3</sub> is due to multiphonon transitions since energy transfer does not occur and can be fit by a theory as shown by the solid line. Subtracting the radiative rate as calculated from Judd-Ofelt from the lifetime at any particular temperature yields the non-radiative rate or the multiphonon transitions. Figure 10 is a plot of the multiphonon transition rate as a function of energy gap between energy levels for a series of materials.

AD-A184 754

DEFECT CHARACTERIZATION IN QUARTZ AND RELATED MATERIALS 2/2

(U) OKLAHOMA STATE UNIV STILLWATER DEPT OF PHYSICS

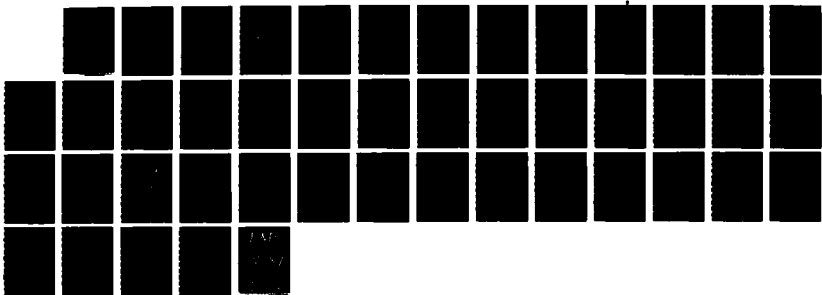
L E HALLIBURTON ET AL JUN 87 RADC-TR-87-66

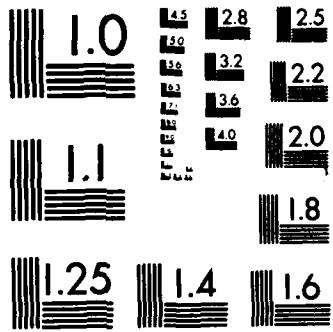
UNCLASSIFIED

F19628-83-K-0007

F/G 20/3

NL





MICROCOPY RESOLUTION TEST CHART  
NATIONAL BUREAU OF STANDARDS-1963-A

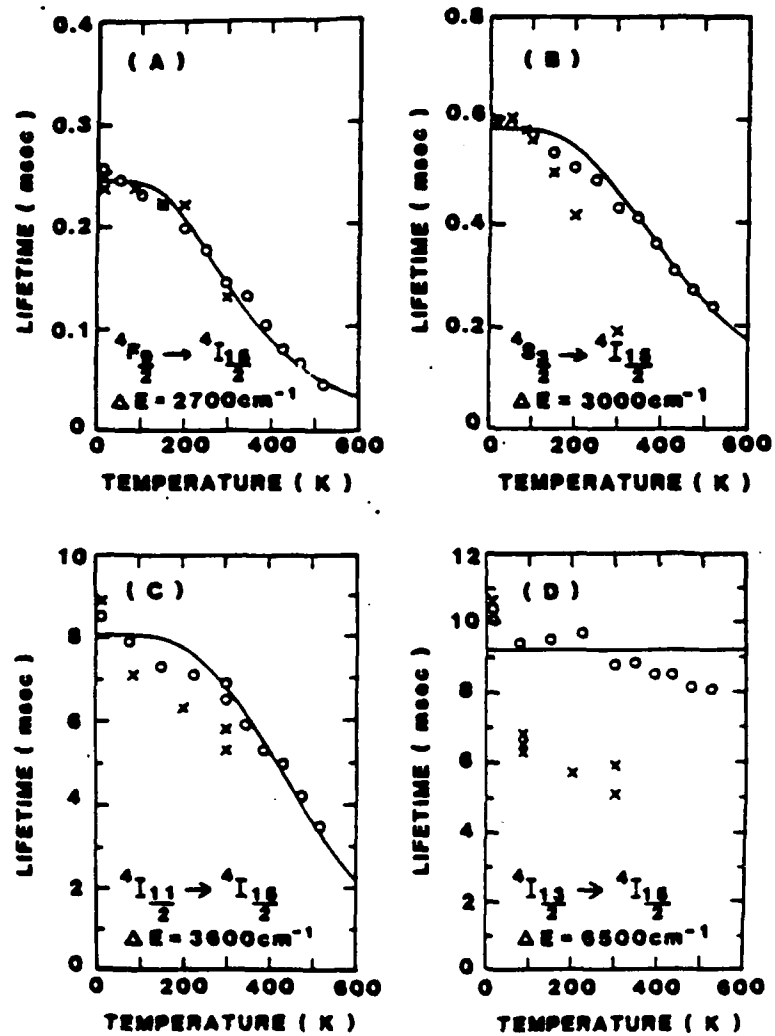


Figure 9  
 Temperature dependence of the (a)  ${}^4F_{9/2}$  (b)  ${}^4S_{3/2}$  (c)  ${}^4I_{11/2}$  (d)  ${}^4I_{13/2}$  emission lifetimes.

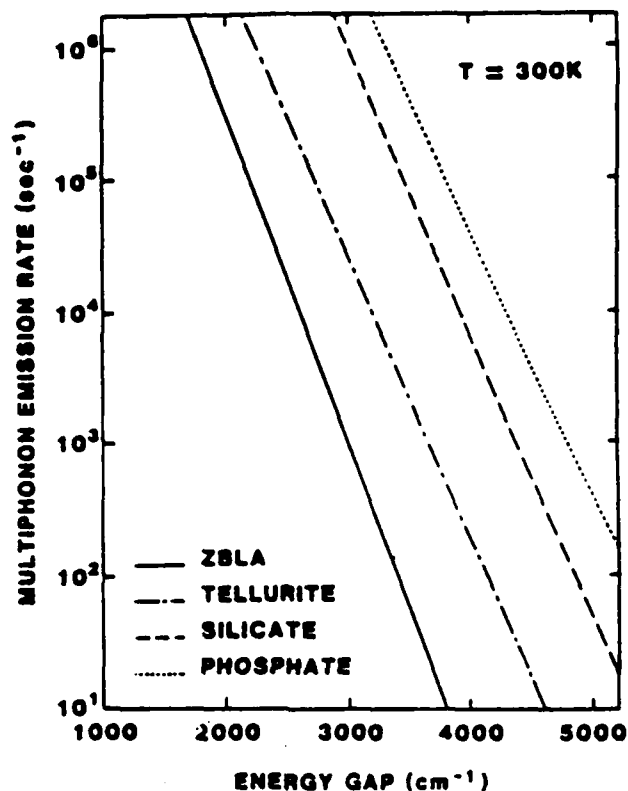


Figure 10

Multiphonon transition rate as a function of the energy gap between energy levels for various materials.

Notice that the fluorozirconate material, ZBLA, shows a much lower multiphonon emission rate than the other materials. Since the multiphonon emission rate is low, the radiative rate is high and the materials should operate more efficiently at a higher temperature than the other materials. This suggests the fluorozirconate materials and other heavy metal fluoride glasses should be excellent for optical devices. The question, of course is, is it possible to produce a laser using this glass host material? It would be highly desirable to have a  $\text{Nd}^{3+}$  laser in this host. In the evaluation the cross section

$$\sigma \text{ (cm}^2\text{)} = \frac{(\lambda_{\text{probe}})^2 \eta}{4\pi^2 n^2 \Delta\nu \tau_s} \quad (1)$$

where  $\eta$  is the quantum efficiency,  $n$  the index of refractions,  $\Delta\nu$  the frequency half width of the transition,  $\lambda$  the probe wavelength and  $\tau_s$  the lifetime of the stimulated emission.

The gain coefficient  $\gamma$  is defined as

$$\gamma \text{ (cm}^{-1}\text{)} = \frac{\ln [G+1]}{d} \quad (2)$$

where the gain  $G = \frac{I_{\text{probe}} - I_0}{I_0}$  and  $d$  is the sample thickness must be evaluated.

In order to investigate the possibility of stimulated emission in ZBLA:Nd<sup>3+</sup> the experimental configuration shown in Figure 11 was employed.

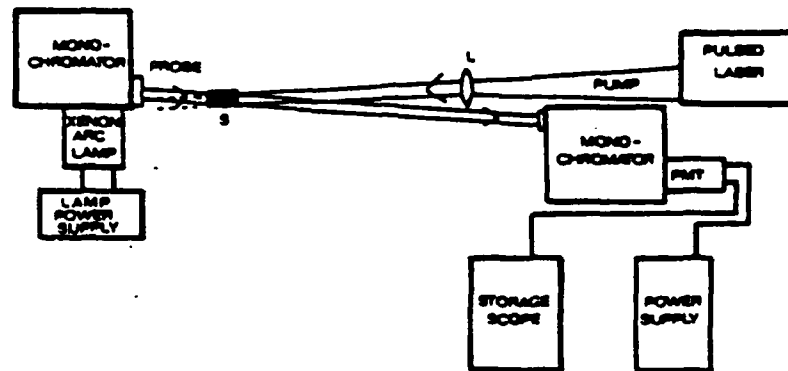


Figure 11  
Experimental system for single pass gain measurements.

The measurement of gain was easily made with this system. For ZBLA:Nd the threshold power (mJ/pulse) is 4.8 whereas it is 3.8 for ED-2 silicate:Nd according to Weber. [9] The cross section for ED-2 silicate:Nd is  $2.6 \times 10^{-20} \text{ cm}^2$  and  $8.5 \times 10^{-20}$  for ZBLA:Nd. The onset of laser action is also shown in Figure 12. This suggests that laser operation is possible in these materials and since the multiphonon interactions are so low an efficient laser system should be possible.

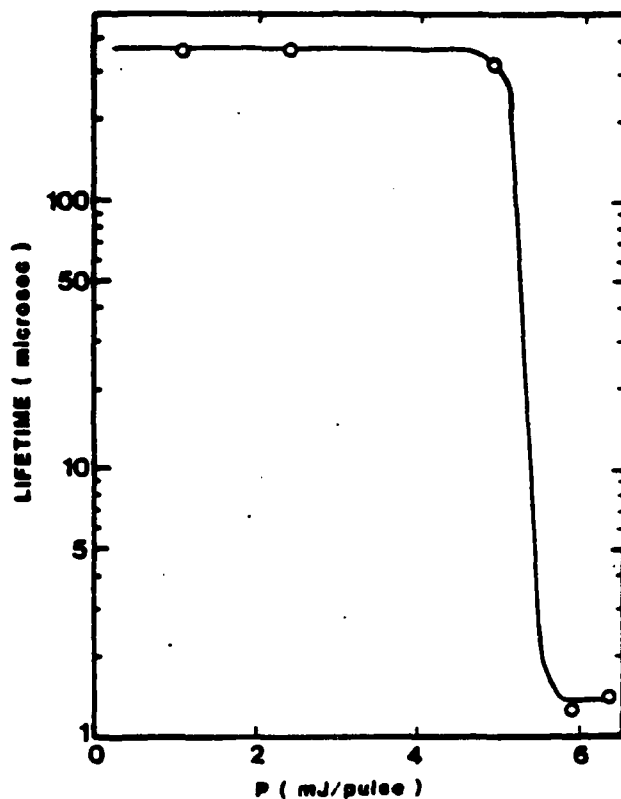


Figure 12  
The onset of stimulated emission for ZBLA:Nd.

Other impurities such as the transition metal ions are also of great importance in these materials for device applications such as electroluminescence or upconversion. [22,23] Figures 13, 14, 15 illustrate the optical absorption or excitation spectra of impurities such as  $Mn^{2+}$ ,  $Co^{2+}$ , and  $Ni^{2+}$  when embedded in  $MgF_2$  single crystals or ZBLA glass at 86K. In the figures the notation for  $O_h$  crystal field is used for simplicity and reference to Tanabe-Sugano diagrams [26]. In actuality the crystal field symmetry is much lower.



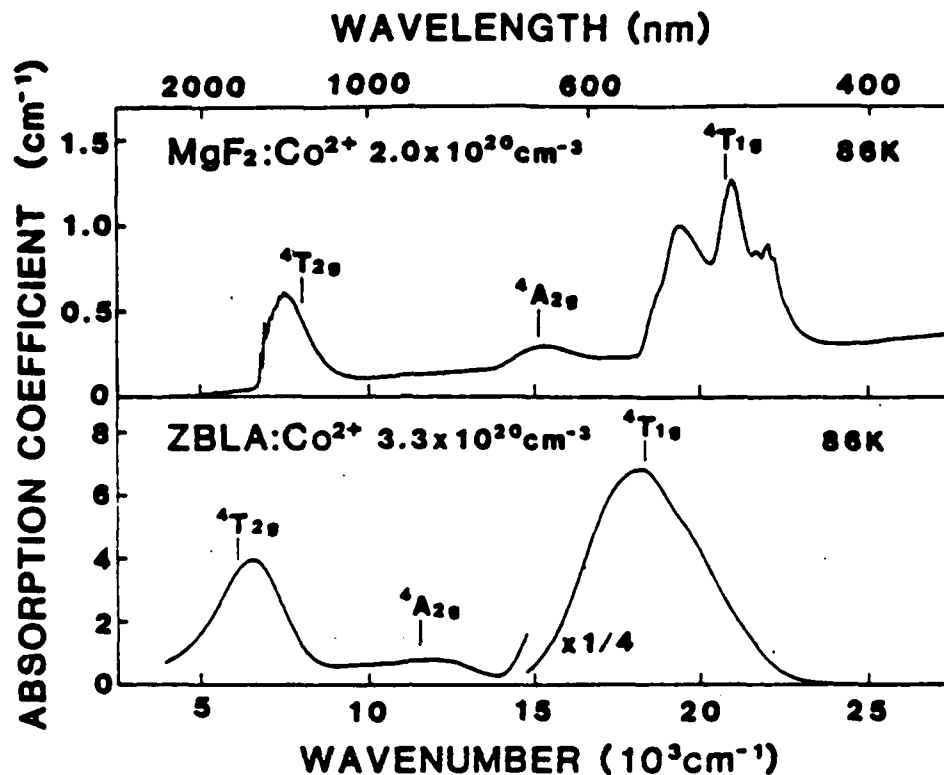


Figure 13  
Absorption spectra of  $\text{Co}^{2+}$  ( $2.0 \times 10^{20}$  ions  $\text{cm}^{-3}$ ) in  $\text{MgF}_2$  crystal (upper frame), and  $\text{Co}^{2+}$  ( $3.3 \times 10^{20}$   $\text{cm}^{-3}$ ) in ZBLA glass (lower frame) at 86K.

Notice that there is a shift in the optical absorption between the glass and the crystals. It is evident that the lowest energy  $\text{Mn}^{2+}$  absorption shifts to higher energies, whereas all the  $\text{Co}^{2+}$  and  $\text{Ni}^{2+}$  absorption shift to lower energies. It should also be noted that for the same impurity concentrations the glass has a stronger optical absorption indicating larger oscillator strengths for the glass. This may be caused by the asymmetric crystal field around the impurities in the glass, which aids (d - d) parity - forbidden electric - dipole transitions. The shift in absorption as noted above can be explained by utilization of Tanabe-Sugano diagrams for crystal field effects. [26] This is shown in Figures 16, 17, and 18 for  $\text{Mn}^{2+}$ ,  $\text{Co}^{2+}$  and  $\text{Ni}^{2+}$  respectively.

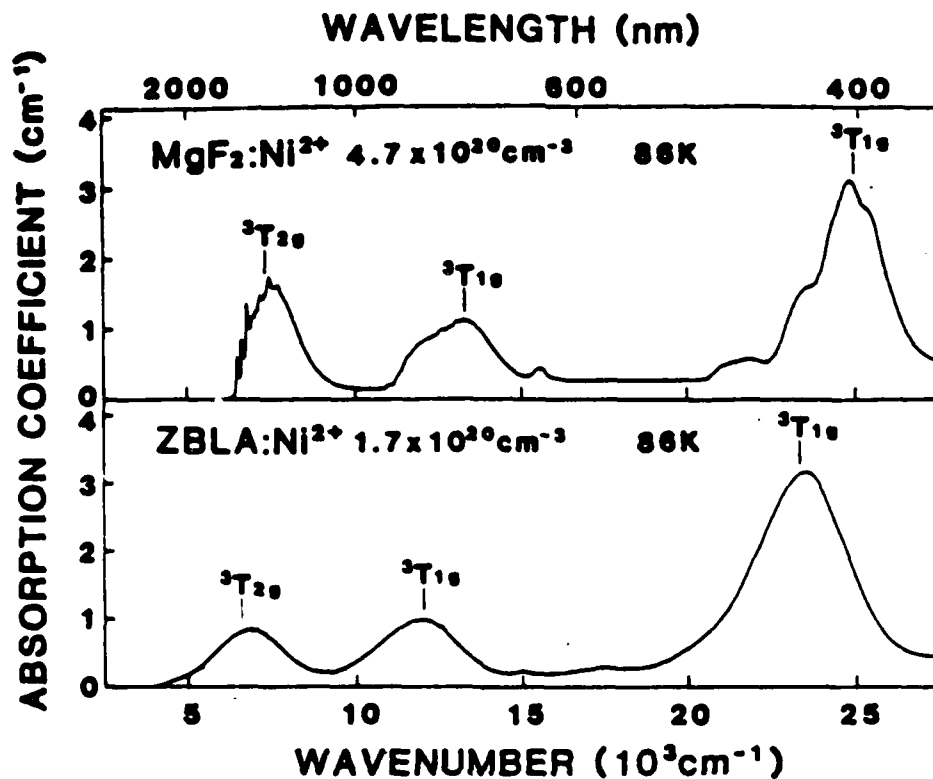


Figure 14

Unpolarized absorption spectra of Ni<sup>2+</sup> ( $4.7 \times 10^{20}$  ions cm<sup>-3</sup>) in MgF<sub>2</sub> crystal (upper frame), and Ni<sup>2+</sup> ( $1.7 \times 10^{20}$  ions cm<sup>-3</sup>) in ZBLA glass (lower frame) at 86K. The transition energies estimated from Tanabe-Sugano diagrams [26] are shown by vertical lines.

Notice that in the case of Mn<sup>2+</sup> an increasing crystal field moves the absorption or emission energies to longer wavelengths whereas the opposite is the case for Co<sup>2+</sup> and Ni<sup>2+</sup> just as is observed in Figures 13 and 14. This can have a detrimental effect for infrared transitions since the multiphonon rate increases when levels are closer together. Therefore, in the case of Co<sup>2+</sup>, which has shifted further into the infrared, no optical luminescence is noted even at 15 K. In Ni<sup>2+</sup> only a weak emission is observed at 2 μm. For Mn<sup>2+</sup> the emission is present and has a temperature independent lifetime as might be expected for multiphonon transitions. [27]

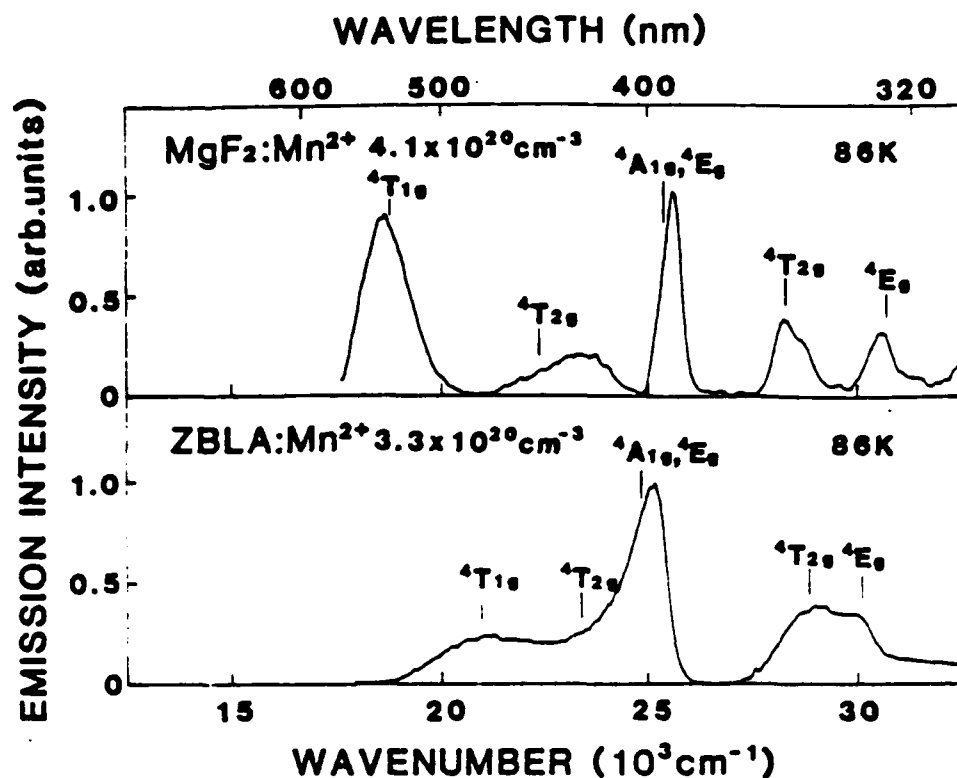


Figure 15

Unpolarized excitation spectra of  $\text{Mn}^{2+}$  ( $4.1 \times 10^{20}$  ions  $\text{cm}^{-3}$ ) in  $\text{MgF}_2$  crystal (upper frame), and  $\text{Mn}^{2+}$  ( $3.3 \times 10^{20}$  ions  $\text{cm}^{-3}$ ) in ZBLA glass (lower frame) at 86K. Emission has been detected at  $16840 \text{ cm}^{-1}$  for  $\text{MgF}_2$ , and at  $17450 \text{ cm}^{-1}$  for ZBLA.

#### IV. SUMMARY

In summary, it appears that heavy metal fluoride glass materials are attractive for optical communication systems. They can be used both as long range transmission light guides and as device materials. The room temperature operation of these optical devices is extremely important and the low multiphonon rates for the heavy metal fluoride glasses make them especially useful for this type of system. The possibility of using them to change infrared light to visible light through two photon processes known as upconversion is also possible because of the low multi phonon rates. Radiation damage can be a problem in some instances but it appears that it is not a major problem and that the utilization of the  $\text{BaF}_2/\text{ThF}_4$  base glasses would circumvent the problem. Therefore, it is evident that these materials are highly promising for future research and potential applications.

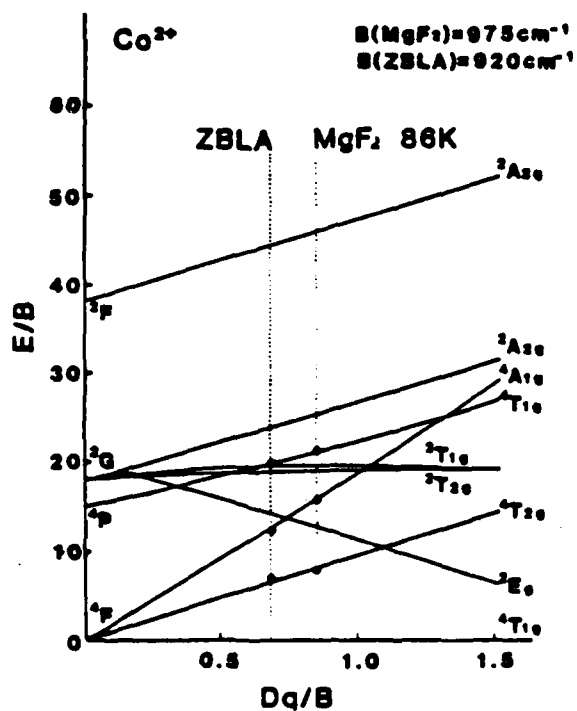


Figure 16  
Tanabe-Sugano diagram for  $\text{Co}^{2+}$ .  
Vertical dotted lines show the crystal  
fields for  $\text{MgF}_2$  and ZBLA glass at 86K.  
The values of  $Dq$  and  $B$  are  $825 \text{ cm}^{-1}$   
and  $975 \text{ cm}^{-1}$  for  $\text{MgF}_2$ ,  $630 \text{ cm}^{-1}$   
and  $920 \text{ cm}^{-1}$  for ZBLA. The value  
of  $(C/B)$  has been fixed at 4.63.

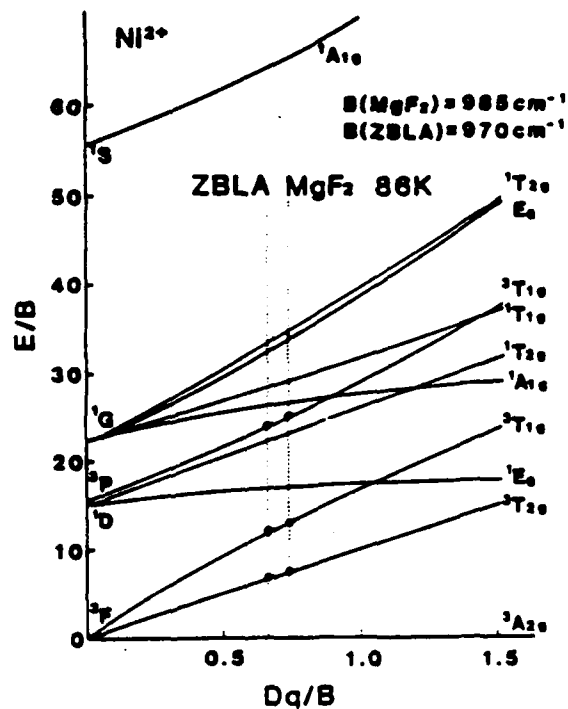


Figure 17  
Tanabe-Sugano diagram for  
 $\text{Ni}^{2+}$  vertical dotted lines  
show the crystal fields in  $\text{MgF}_2$   
crystals and ZBLA glass at 86K. The  
values of  $Dq$  and  $B$  are  $725 \text{ cm}^{-1}$  and  
 $985 \text{ cm}^{-1}$  for  $\text{MgF}_2$  and  $640 \text{ cm}^{-1}$   
and  $970 \text{ cm}^{-1}$  for ZBLA. The value of  
 $(C/B)$  has been fixed at 4.71.

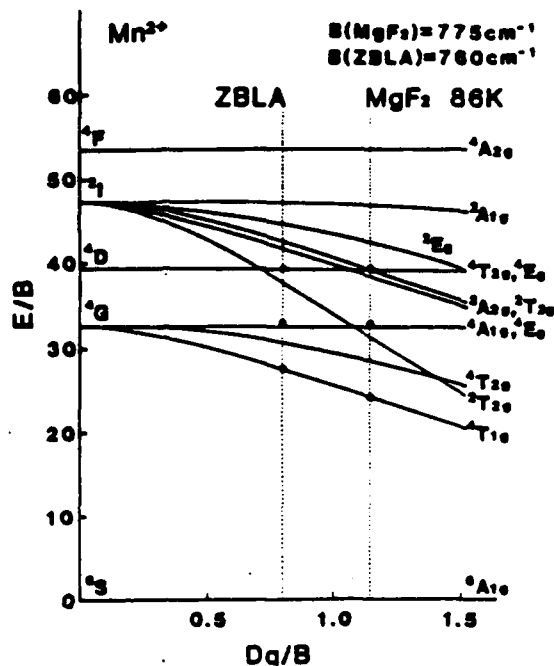


Figure 18

Tanabe-Sugano diagram for Mn<sup>2+</sup>. Vertical dotted lines show the crystal fields in MgF<sub>2</sub> crystal and ZBLA glass at 86K. The values of Dq and B are 890 cm<sup>-1</sup> and 775 cm<sup>-1</sup> for MgF<sub>2</sub>, 610 cm<sup>-1</sup> and 760 cm<sup>-1</sup> for ZBLA. The value of (C/B) has been fixed at 4.48.

#### V. ACKNOWLEDGEMENTS

This work was supported by NSF - DMR 84-06476 and F-19628-83-K0007 Rome Air Development Center Hanscom AFB. We gratefully acknowledge the assistance of M.G. Drexhage, M. Suscavage, B. Bendow and O. H. El Bayoumi for helpful discussion and the glass samples.

#### VI. REFERENCES

1. J. Lucas, M. Chanthanashin, M. Poulain, M. Poulain, P. B. Brun, and M. J. Weber. *J. Non-Cryst. Solids* **27**, 273 (1978).
2. A. Lecoq and M. Poulain, *Verres Refract* **34**, 333 (1980).
3. M. D. Shinn, W. A. Sibley, M. G. Drexhage, and R. N. Brown, *Phys. Rev.* **827**, 6635 (1983).
4. M. P. Brassington, T. Hailing, A. J. Miller, and G. A. Saunders. *Mater. Res. Bull.* **16**, 631 (1981).
5. D. L. Gavin, K.-H. Chung, A. J. Bruce, C. T. Moynihan, M. G. Drexhage, and O. H. El-Bayoumi, *J. Am. Ceram. Soc.* **65**, C-182 (1982).
6. D. Leroy, J. Lucas, M. Poulain, and D. Ravaine, *Mater. Res. Bull.* **13**, 1125 (1978).

7. D. C. Tran, G. H. Sigel, and B. Bendow, *J. Lightwave Technology* LT-2, 566 (1984).
8. M. G. Drexhage, in: *Treatise on Material Science and Technology*. Vol. 26, eds. M. Tomazawa and R. H. Doremus (Academic Press, New York, 1985), p. 151-243.
9. L. A. Riseberg and M. J. Weber in: *Progress in Optics*, Vol. XIV, ed. by E. Wolf (North Holland, Amsterdam, 1976), p. 89 and *Handbook of Laser Science & Tech.* Vol. 1 ed. Marvin J. Weber, CRC Press, Fla. (1982).
10. M. G. Drexhage, B. Bendow, and C. T. Moynihan, *Laser Focus* 10, 62 (1980).
11. B. Bendow and M. G. Drexhage. *Proc. Soc. Photo-Opt. Instrum. Eng.* 266, 16 (1981); *Opt. Eng.* 21, 118 (1982).
12. H. Slim, Ph.D. Thesis. University Rennes, Rennes, France (1981).
13. M. G. Drexhage, O. H. El-Bayoumi, C. T. Moynihan, A. J. Bruce, K.-H. Chung, D. L. Gavin, and T. J. Lovetz, *J. Am. Ceram. Soc.* 65, C-168 (1982).
14. P. E. Fisanich, L. E. Halliburton, L. N. Feuerhelm, and S. M. Sibley, *J. Non-Cryst. Solids* 70, 37 (1985).
15. R. Cases, D. L. Griscom, and D. C. Tran, *J. Non-Cryst. Solids* 72, 51 (1985).
16. D. L. Griscom and D. C. Tran, *J. Non-Cryst. Solids* 72, 159 (1985).
17. K. Tanimura, M. Ali, L. N. Feuerhelm, S. M. Sibley, and W. A. Sibley, *J. Non-Cryst. Solids* 70, 397 (1985).
18. E. J. Friebele and D. C. Tran, *J. Non-Cryst. Solids* 72, 221 (1985); *Commun. Am. Cer. Soc.*, 68, C-279 (1985).
19. K. Tanimura, W. A. Sibley, M. Suscavage, and M. G. Drexhage, *J. Appl. Phys.* To be published.
20. J. L. Adam and W. A. Sibley, *J. Non-Crystalline Solids*. To be published.
21. K. Tanimura, M. D. Shinn, W. A. Sibley, M. G. Drexhage, and R. N. Brown, *Phys. Rev.* B30, 2429 (1984).
22. R. Reisfeld, G. Katz, N. Spector, C. K. Jorgensen, C. Jacoboni, and R. DePape, *J. Solid State Chem.* 41, 253 (1982).
23. C. K. Jorgensen and R. Reisfeld, *J. of Less-Common Metals* 73, 107 (1982).
24. F. E. Auzel, *Proc. IEEE* 61, 758 (1973).
25. J. C. Wright in *Topics in Appl. Phys.* Vol. 15, ed. F. K. Fong, (Springer-Verlag, New York, 1976), p. 237.
26. Y. Tanabe and S. Suigano, *J. Phys. Soc. Japan* 9, 753 (1959).
27. L. N. Feuerhelm, S. M. Sibley, and W. A. Sibley, *J. Solid State Chem.* 54, 164 (1984).

## C. Fracton Linebroadening in Doped Glasses

### I. INTRODUCTION

Physical properties such as thermal conductivity, heat capacity, and ultrasonic attenuation are known to be quite different at low temperatures in glasses as compared to crystals.<sup>1</sup> This has been attributed to additional degrees of freedom in amorphous solids that are not present in crystals. These are described by a phenomenological model consisting of two possible local atomic or bonding equilibrium arrangements separated by a potential barrier.<sup>2,3</sup> The local system can vibrate within one potential well or tunnel between the two wells. These localized "two-level systems" (TLS) provide the additional density of states necessary to interpret many of the observed experimental results. However there are still many unanswered questions concerning the fundamental nature of these TLS and the role they play in determining other properties of amorphous solids. Thus, this is still a very active area of research.

One method of probing the properties of additional degrees of freedom of solids has been to study the temperature dependence of the homogeneous linewidth of an optical transition of an impurity ion in the solid. This has become an especially powerful tool with the use of high resolution lasers to selectively excite subsets of ions within an inhomogeneously broadened spectral profile so homogeneous linewidths can be measured even in the presence of significant static strain broadening. Hole-burning in absorption and fluorescence linewidth narrowing (FLN) in emission

make use of this technique. FLN experiments on  $\text{Eu}^{3+}$  ions in a silicate glass host have shown a  $T^2$  dependence for the homogeneous linewidth at low temperatures.<sup>4</sup> This has been interpreted in terms of contributions to the linebroadening due to the interaction between the impurity ion and the local TLS.<sup>5-7</sup> Further experimental data are required to increase our understanding of this type of linebroadening mechanism.

We report here the results of FLN measurements on  $\text{Eu}^{3+}$  in three different types of glass hosts at temperatures ranging from 10 to 300 K. The residual inhomogeneous linewidth at 10 K is found to increase linearly with energy across the inhomogeneously broadened band. The homogeneous linewidth at both the high and low energy sides of the inhomogeneously broadened band is found to obey a  $T^2$  dependence over the entire temperature range investigated for all three glasses.

It was first suggested by Stapleton and co-workers<sup>8</sup> that fractal structures might have an anomalous phonon density of states that would affect electron-phonon relaxation processes. Using the fracton concept of Alexander and Orbach<sup>9</sup> we consider the coupling of the impurity ion to the vibrational degrees of freedom of the amorphous host. Both the temperature dependence and the magnitude of the observed linewidths are consistent with Raman broadening by the localized vibrations (fractons).

## II. EXPERIMENTAL

The laser-narrowed fluorescence linewidth was measured with the apparatus shown schematically in Fig. 1. The 10 ns excitation pulse from the nitrogen laser-pumped tunable dye laser



Passed through an extra-cavity etalon reducing its linewidth to  $0.15 \text{ cm}^{-1}$ . Coumarin dye was used to produce resonant excitation of the  $\text{Eu}^{3+} 7\text{F}_0-5\text{D}_0$  transition of interest. The samples were mounted on the coldfinger of a closed-cycle helium cryostat permitting measurements between 10 and 300 K. The fluorescence was focused on the entrance slit of a Spex 1-m spectrometer set for a resolution of  $0.08 \text{ \AA}$ . A shutter placed between the sample and the spectrometer was opened 0.6 ms after the excitation pulse to eliminate the possibility of contamination of the signal by scattered laser light after resonant excitation. The window of the boxcar integrator was set to look at the spectrum 1.0 ms after the excitation pulse. It is shown elsewhere that energy transfer does not broaden the fluorescence on this time scale.<sup>10</sup>

Three europium doped glass samples were investigated. These had the following composition in mole per cent: lithium silicate glass (LS), 57.0  $\text{SiO}_2$ , 27.5  $\text{Li}_2\text{O}$ , 10.0  $\text{CaO}$ , 2.5  $\text{Al}_2\text{O}_3$ , 3.0  $\text{Eu}_2\text{O}_3$ ; sodium silicate glass (NS), 72.0  $\text{SiO}_2$ , 15.0  $\text{Na}_2\text{O}$ , 5.0  $\text{BaO}$ , 5.0  $\text{ZrO}$ , 3.0  $\text{Eu}_2\text{O}_3$ ; and potassium germanate glass (KG), 65.3  $\text{GeO}_2$ , 17.0  $\text{K}_2\text{O}$ , 17.0  $\text{BaO}$ , 0.7  $\text{Eu}_2\text{O}_3$ . The spectral properties of these samples have been reported previously.<sup>10</sup>

### III. HOMOGENEOUS AND INHOMOGENEOUS CONTRIBUTIONS TO THE LASER-NARROWED FLUORESCENCE LINEWIDTH

For resonant excitation of a transition, such as that studied here, the transition linewidth is given using the approximation of Kushida and Takushi,<sup>11</sup>

$$2\Delta\nu = \Delta\nu_{\text{obs}} - \Delta\nu_{\text{res}} \quad (1)$$

where  $\Delta\nu$  is the linewidth of the transition,  $\Delta\nu_{\text{obs}}$  is the

observed fluorescence linewidth, and  $\Delta\nu_{res}$  is the instrumental resolution. Fig. 2 displays the temperature dependence of the narrowed fluorescence linewidth for excitation on the high energy and low energy sides of the inhomogeneously broadened band for the lithium silicate glass (LS), the sodium silicate glass (NS), and the potassium germanate glass (KB). In each case the linewidth has an approximately quadratic temperature-dependence at high temperatures, but is seen to approach a temperature-independent limit at low temperatures. This differs from previously reported results in glasses<sup>4</sup> where the quadratic temperature dependence was seen to extend to 10 K. Note that the limiting values of the linewidths in Fig. 2 are about an order of magnitude larger than the instrumental resolution. However, because we have used an extra-cavity etalon rather than an intra-cavity etalon, as employed by Yen and co-workers,<sup>4,11</sup> the linewidth of our excitation pulse is an order of magnitude larger. This suggests that the temperature-independent contribution to the linewidth is residual inhomogeneous broadening due to imperfect site selection. Because the inhomogeneous contribution has been reduced to about  $1\text{ cm}^{-1}$  from the several hundred  $\text{cm}^{-1}$  width before site selective excitation,<sup>10</sup> it can be deconvoluted from the homogeneous linewidth using the same techniques employed for crystalline hosts. The results of this procedure are shown in Fig. 3. They are consistent with a quadratic temperature dependence for the homogeneous linewidth from 10 K to the highest temperatures measured for all of the samples.

The dependence of the linewidth on the excitation frequency

was also measured at 10 K. These results are shown in Fig. 4. It can be seen that the linewidth increases monotonically in a roughly linear fashion as the excitation frequency is scanned from the low to the high frequency side of the inhomogeneously broadened band. This is the behavior to be expected of the residual inhomogeneous linewidth. The inhomogeneous broadening arises from variations in the crystal field from site to site in the glass. The residual broadening is a measure of the number of different local environments that have crystal fields similar enough that the energy difference in their electronic transitions is within the excitation linewidth. One naively expects this density of site distributions to be greater on the high energy side of the inhomogeneously broadened band where the crystal field splitting is strongest due to the larger number of ligands involved. It is noteworthy that the homogeneous linewidth does not behave in this way in one of the glasses studied. Figures 2 and 3 show that for the LS glass the measured linewidth is smaller on the high frequency side of the band than on the low at temperatures above 60 K. The homogeneous linewidth which we extract from the measurements is smaller on the high frequency side at all temperatures covered in these experiments. This behavior of the homogeneous linewidth is opposite to that of the other two glasses studied and to the observations of Morgan, et al.<sup>7</sup> on the linewidth of a variety of glasses at room temperature.

#### IV. FRACTON MODEL FOR THE HOMOGENEOUS LINEWIDTH

In crystals the electron-phonon interactions control the

temperature dependent linewidth, with direct processes producing an exponential dependence and Raman processes leading to a  $T^7$  dependence for  $T \ll \theta_D$  and a  $T^2$  dependence for  $T \gg \theta_D$ .<sup>12,13</sup> This is quite different from glasses which exhibit a universal quadratic temperature dependence for the homogeneous linewidth. Lyo and Orbach<sup>5</sup> have shown that the TLS that have been invoked to explain the anomalous thermal properties of glasses below 1 K can lead to a quadratic dependence of the homogeneous linewidth. However, this result holds as a low temperature approximation only and requires a uniform density of states for the TLS. At high temperatures this model produces a linear temperature dependence. It is difficult to accept that the low temperature limit would be valid at 300 K. Although the TLS is a very successful model in accounting for thermal properties at very low temperatures and acoustic properties at low frequencies, the nature of these TLS has not been determined. While it is generally accepted that they involve tunneling between neighboring sites of local equilibria in the glass structure, it is not known whether the entities involved in the tunneling are individual ions or such larger clusters. If the latter were the case, their effect on the local environment of the optically active ions might be negligible.

In this section we develop a simple model of the homogeneous linewidth based on the "fracton" concept of Alexander and Orbach.<sup>9</sup> This differs from the TLS model in that the impurity ion interacts with the vibrational excitations of the host rather than the TLS modes. The quadratic temperature dependence is shown to be a natural result of Raman processes involving these

non-Debye-like atomic vibrations and the magnitudes of the electron-phonon (or electron-fracton) coupling constants needed to obtain the observed linewidths are found to be consistent with those found in crystals.

The Raman contribution to the homogeneous linewidth is given by

$$\Delta\nu_R = (4\pi^2/\hbar) |\langle f|V_R|i\rangle|^2 \int_0^{\omega_{\max}} |\langle f|e^2|i\rangle|^2 g(\omega)^2 d\omega \quad (2)$$

where  $\langle f|e^2|i\rangle$  is a matrix element of the average local strain,  $g(\omega)$  is the vibrational density of states, and  $\langle f|V_R|i\rangle$  is the electrostatic matrix element for the Raman process. With the strains and the density of states treated in the Debye approximation this leads to the conventional McCumber and Sturge result for crystals.<sup>12</sup> The expression shown in Eq. (2) is based on a perturbation theory approach to the problem. Recently a nonperturbative theory has been developed by Hsu and Skinner<sup>13</sup> which gives the same result as the perturbative approach in the weak coupling limit. At low temperatures both theories have the same form of the expression describing the linewidth with a different meaning for the coupling coefficients. Since no exact values are known for parameters such as the Debye temperature and electron-phonon coupling parameters for the samples used in this work, we use the form of the expression consistent with weak coupling and treat the Debye temperature and coupling parameters as adjustable parameters.

In glasses the Debye approximation is not a good representation of the vibrational states except at very long wavelengths. Orbach and co-workers<sup>9,14</sup> have shown that for shorter wave-

lengths, still much larger than atomic dimensions, plane waves are no longer a good representation of the normal modes; instead, they are localized in the disordered structures of the glass network. By modeling the glass structure as a self-similar fractal, Alexander and Orbach<sup>9</sup> have been able to obtain the vibrational density of states and dispersion without recourse to the usual reciprocal space transformations. In a series of papers<sup>14</sup> Orbach and co-workers have shown that this model can explain the thermal properties of amorphous solids above 1 K. Below this temperature it is still necessary to invoke the elusive TLS. In their model the vibrations at long wavelengths are treated in the Debye approximation but at some critical length scale  $L$  the disorder in the network causes the vibrations to become localized. The resulting vibrational density of states is

$$\begin{aligned} g_p(\omega) &= d(d/L^d)\omega^{d-1}/\omega_D^d & l > L \\ g_f(\omega) &= \tilde{d}(d/L^d)\omega^{\tilde{d}-1}/\omega_L^{\tilde{d}} & l < L \end{aligned} \quad (3)$$

where  $\omega_D$  is the effective "Debye frequency" for the phonons at  $l=L$ ,  $\omega_L$  is the fracton frequency at  $l=L$ , and  $d$ ,  $\bar{d}$ ,  $\tilde{d}$  are respectively the Euclidean, Hausdorff, and fracton dimensionalities. The characteristic length  $l$  of the vibration is its wavelength in the plane wave regime and its localization length in the fracton regime. For the fractons the dispersion is no longer Debye-like. Assuming only a single kind of self-similarity

$$\omega \propto l^{-\tilde{d}/\tilde{d}} \quad (4)$$

One expects rather generally that the average local strain associated with a normal mode of amplitude  $Q$  should scale as  $Q/l$ .

With this, the dispersion relationship, and density of states given above, the Raman contribution to the linewidth becomes

$$\Delta\nu_R = q(T/\theta_D)^7 \int_0^{\theta_D/T} x^6 e^x (e^x - 1)^{-2} dx + A(T/\theta_L)^{p+1} \int_0^{\theta_F/T} x^p e^x (e^x - 1)^{-2} dx \quad (5)$$

where each  $\theta_i$  is  $\hbar/k$  times the corresponding  $\omega_i$  and the exponent  $p = 4(\bar{d}/\tilde{d}) + 2\tilde{d} - 4$ . The  $q$  and  $A$  parameters contain the same  $|<f|V_R|i>|^2$  electron-phonon coupling parameter as in the conventional treatment for crystals. For the glasses studied here  $d = 3$ . The Hausdorff dimensionality  $\bar{d}$  must lie between 3 and 2.5 which is the value found for a critically percolating structure. The fracton dimensionality  $\tilde{d}$  was first conjectured by Alexander and Orbach<sup>9</sup> to be universally  $4/3$ . Recent calculations in the effective medium approximation by Derrida, et al.<sup>14</sup> give  $\tilde{d} \approx 1$ ; however, this technique frequently does not give trustworthy estimates of exponents.  $\theta_D$  will now be much smaller than crystalline Debye temperatures. It is well known that for  $T > \theta_D/2$  the Debye-phonon term in Eq. (5) becomes quadratic in  $T$ . In Fig. 4 we show the results of a numerical evaluation of the fracton contribution to the linewidth. This can be seen to approach  $T^2$  for any of the dimensionalities in the expected range provided  $T > 2\theta_L$ .

The structure of the host glass enters this model through the Hausdorff dimensionality  $\bar{d}$ . If  $\bar{d} \geq d$ , the structure is compact and has essentially the same atomic connectivity as would a crystal. An open structure for the glass will have a smaller value for  $\bar{d}$ , limited of course by  $\bar{d} = 2.5$  for a critically percolating cluster. The results in Fig. 5 are not especially sensi-

tive to  $\bar{d}$ . Thus assuming a nearly universal value for  $\bar{d}$  as conjectured by Alexander and Orbach,<sup>8</sup> the linewidth should not depend strongly on the glass structure.

In order to fit the specific heat data above 1 K, Tsa, et al.<sup>13</sup> find  $\theta_L=14$  K,  $\theta_D=29$  K and  $\bar{d} = 1.3$ . Assuming similar values for the glasses studied here, an essentially quadratic temperature dependence for the homogeneous linewidth is predicted throughout the range covered by these experiments. The fracton contribution will dominate the Debye-phonon contribution at all temperatures in this range.

A first principles calculation of the electron-phonon coupling  $|\langle f|V_R|i\rangle|^2$  is not presently possible even for crystals. One can, however, calculate the A parameter required to produce the experimentally observed linewidth and use this to estimate the  $\epsilon$  parameter that would be observed in a crystal with a Debye phonon spectrum and the same average sound velocity and density as the glass. This equivalent  $\epsilon$  is given by

$$\epsilon \approx A\theta_D^{10}/(\theta_L^3\theta_x^7) \quad (6)$$

where  $\theta_x$  is the Debye temperature of this equivalent crystal. Using our observation that the homogeneous linewidth in the glass is about  $10^{-4}\text{T}^2 \text{ cm}^{-1}$ , one obtains  $\epsilon \approx 10^2 \text{ cm}^{-1}$  which is of the same order as observed for rare earth transitions in crystals.<sup>15</sup> This justifies the use of the weak coupling approximation.

Physically, the reason that the fractons produce a larger Raman contribution to the linewidth than found in crystals is that the density of states for the fractons at low frequency is substantially larger than would be found for Debye phonons. This can readily be seen from Eq. (3) since  $\omega_L$  is comparable to  $\omega_D$ ,



but  $d=3$  while  $\tilde{d}=1$ . The quadratic temperature dependence results from the non-Debye-like frequency dependence of the density of states and dispersion.

Implicit in the integration of the linewidth over the whole fracton spectrum is the assumption that the excited ions can in fact sample all of these excitations. With the localized nature of the fractons and the site-selection of an FLN experiment it is not obvious that this will be the case in all conceivable structures at all temperatures. For a glass whose structure is a single self-similar fractal every site in the glass will sample many scales of length and essentially all scales of large  $l$ . The quadratic linewidth which we calculate is determined almost exclusively by fractons with  $\hbar\omega < kT$  leading to the expectation that all the important fractons will be available at each site. Nevertheless, the various fractons may couple to the electronic states with different strengths. By using the average local strain in Eq. (2), the electronic matrix element  $|\langle f|V_R|i\rangle|$  becomes an average over the mode couplings as well. This is also true of electron-phonon coupling in crystals in the equivalent approximation. The fact that our experiments show the same temperature dependence on both sides of the inhomogeneous profile supports the validity of this approximation for these glasses. However, since the magnitudes of the high and low frequency linewidths are different, this average must be taken with different weights in these two parts of the inhomogeneously broadened band. The gross difference between the LS and NS glasses suggests that the frequency dependence of this effective coupling

constant is a structural property that might be predictable from the connectivity of the fractals in a more detailed model. For  $T \ll \theta_L$  the spatial distribution of fractons may become dominant and destroy the validity of this approximation.

Liu<sup>16</sup> has recently developed a model for the localized modes in which the glass structure is taken to have three dimensional connectivity, but the strengths of the interatomic bonds are fractal, giving  $\tilde{d}=1.5$  and  $p=1$ . The number of modes at low frequency is reduced relative to that obtained when the connectivity is fractal. Because of this, the homogeneous linewidth does not follow a simple power law dependence in the temperature range of our experiments.

For  $\text{Eu}^{3+}$  with the resonant pumping conditions used the experiments described here, the only possible direct phonon process which can contribute to the broadening of the spectral line is between the  ${}^7F_0$  ground state and the components of the  ${}^7F_1$  manifold which are split by  $250 \text{ cm}^{-1}$  in these glasses. The increased density of states for the fractons at low frequencies must come at the expense of their high frequency density of states. Using the data reported by Selzer, et al.<sup>4</sup> for  $\text{YAlO}_3:\text{Eu}^{3+}$  we infer a direct process contribution to the linewidth of  $\approx 10^{-2} \text{ cm}^{-1}$  at 100 K, leading to the conclusion that the direct process will be unimportant in these glasses at all temperatures studied here.

## V. SUMMARY AND CONCLUSIONS

We have presented measurements on three structurally different glasses showing the homogeneous linewidth of the  ${}^5D_0$ -

${}^7F_0$  transition to have a quadratic temperature dependence between 10 and 300 K and the residual inhomogeneous broadening in the narrowed fluorescence to increase with increasing excitation frequency across the inhomogeneously broadened band. Using resonant pumping techniques eliminated contributions to the data from overlapping Stark components and direct phonon processes. The results cannot be interpreted in terms of conventional processes involving electron-phonon interactions with Debye-like phonons. The observed behavior appears to be independent of host structure since it is qualitatively the same for all three of the glasses whereas other details of the optical spectra are known to be quite different for these three materials due to structural differences of the glasses.<sup>10</sup>

A simple model based on the fracton concept has been introduced to explain the behavior of the homogeneous linewidth. The increased linewidth and its quadratic temperature dependence are shown to be consequences of Raman broadening by the localized vibrational modes of the glass and their non-Debye-like dispersion and density of states. This model involves fractal behavior of the local structure, as opposed to bonding, and involves electron-phonon coupling modified by the fractal behavior as opposed to direct electron-TLS coupling. The tunneling modes of TLS do not appear to contribute to the line-broadening at the high temperature range investigated here.

The experimental data and theoretical model presented here provide new information concerning the effects of local vibrations on the widths of spectral lines of impurity ions in amorphous host materials. Tests of the universality of the

observed behavior of the temperature dependence of the homogeneous linewidth and the applicability of the model must await further experiments on different types of materials.

ACKNOWLEDGMENTS: This research was supported by Rome Air Development Center and the National Science Foundation under grant number DMR-82-16351.

## REFERENCES

1. For an extensive review of this field see "Amorphous Solids, Low-Temperature Properties", edited by W.A. Phillips (Springer-Verlag, Berlin, 1981).
2. P.W. Anderson, B.I. Halperin, and C. M. Varma, *Phil. Mag.* **25**, 1 (1972).
3. W.A. Phillips, *J. Low Temp. Phys.* **7**, 351 (1972).
4. P.M. Selzer, D.L. Huber, D.B. Hamilton, W.M. Yen, and M.J. Weber, *Phys. Rev. Lett.* **36**, 813 (1976); J. Hagerty and W.M. Yen, *Phys. Rev. Lett.* **43**, 1126 (1979)
5. S.K. Lyo and R. Orbach, *Phys. Rev. B* **22**, 4223 (1980).
6. T.L. Reinecke, *Solid State Commun.* **32**, 1103 (1979).
7. J.R. Morgan, E.P. Chock, W.D. Hopewell, M.A. El-Sayed, and R. Orbach, *J. Phys. Chem.* **85**, 747 (1981).
8. H.J. Stapleton, J.P. Allen, C.P. Flynn, D.B. Stinton, and S.R. Kurtz, *Phys. Rev. Lett.* **45**, 1456 (1980).
9. S. Alexander and R. Orbach, *J. Phys. (Paris) Lett.* **43**, L-625 (1982).
10. X. Gang and R.C. Powell, *J. Appl. Phys.* **57**, 1299 (1985); X. Gang, G. Boulon, and R.C. Powell, *J. Chem. Phys.* **78**, 4374 (1983).
11. T. Kushida and E. Takushi, *Phys. Rev. B* **12**, 824 (1975)
12. D.E. McCumber and M.D. Sturge, *J. Appl. Phys.* **34**, 1682 (1963).
13. D. Hsu and J.L. Skinner *J. Chem. Phys.* **81**, 5471 (1984).
14. S. Alexander, C. Laermans, R. Orbach, and H.M. Rosenberg, *Phys. Rev. B* **28**, 4615 (1983); P.F. Tua, S.J. Putterman, and

R. Orbach, Phys. Lett. 98A, 357 (1983); O. Entin-Wohlman, S. Alexander, R. Orbach, and K.W. Yu, Phys. Rev. B 29, 4588 (1984); B. Derrida, R. Orbach, and K.W. Yu, Phys. Rev. B 29, 6645 (1984).

15. T. Kushida, Phys. Rev. B 185, 500 (1969).

16. S. Liu, unpublished results.

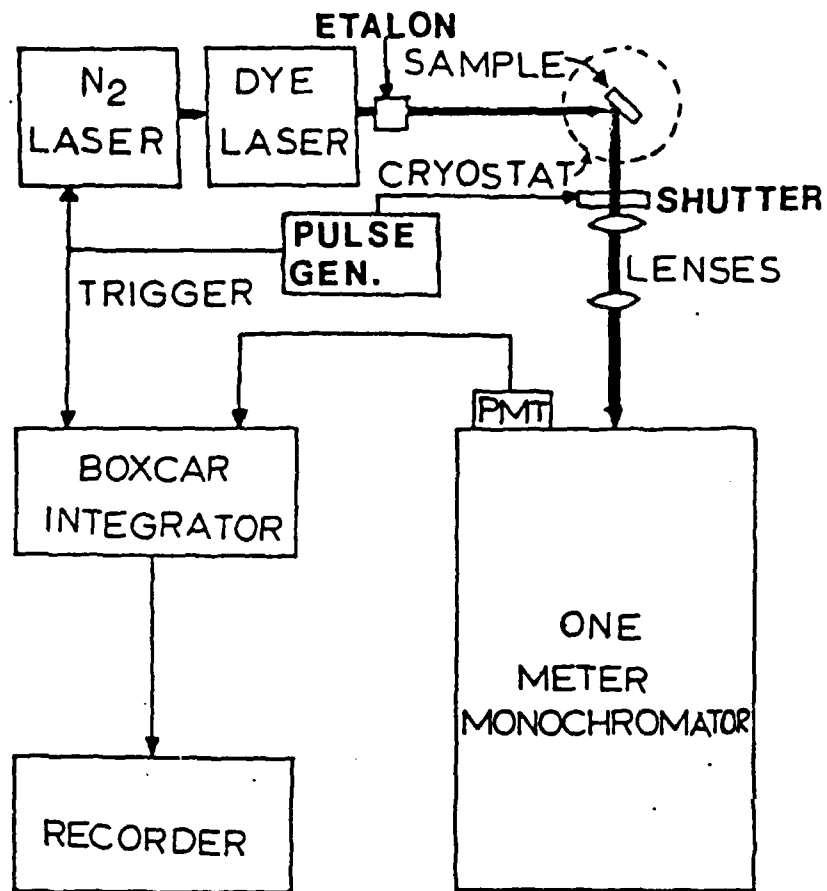


Fig. 1. Block diagram of experimental setup.

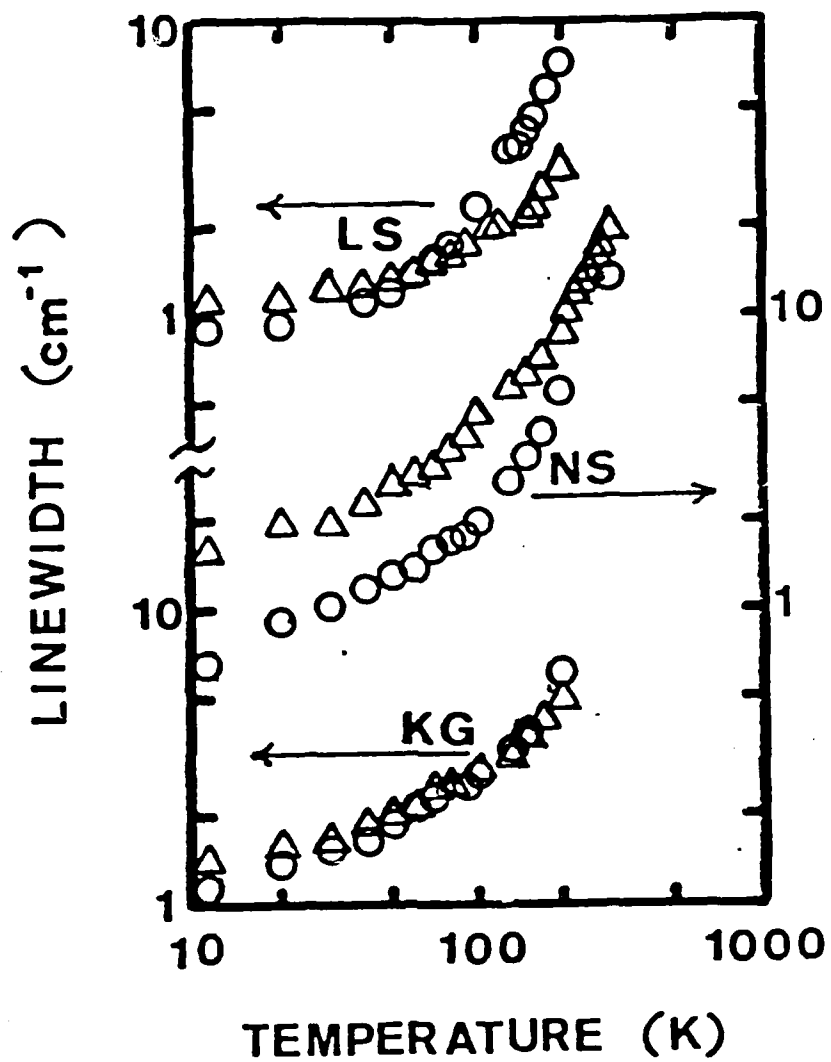


Fig. 2. Temperature dependence of the laser-narrowed linewidths of the  $^5D_0-^7F_0$  transition of  $\text{Eu}^{3+}$  in LS, NS, and KG glasses excited on the high energy ( $\lambda=577.5$  nm, triangles) and low energy ( $\lambda=580.0$  nm, circles) sides of the inhomogeneously broadened band.



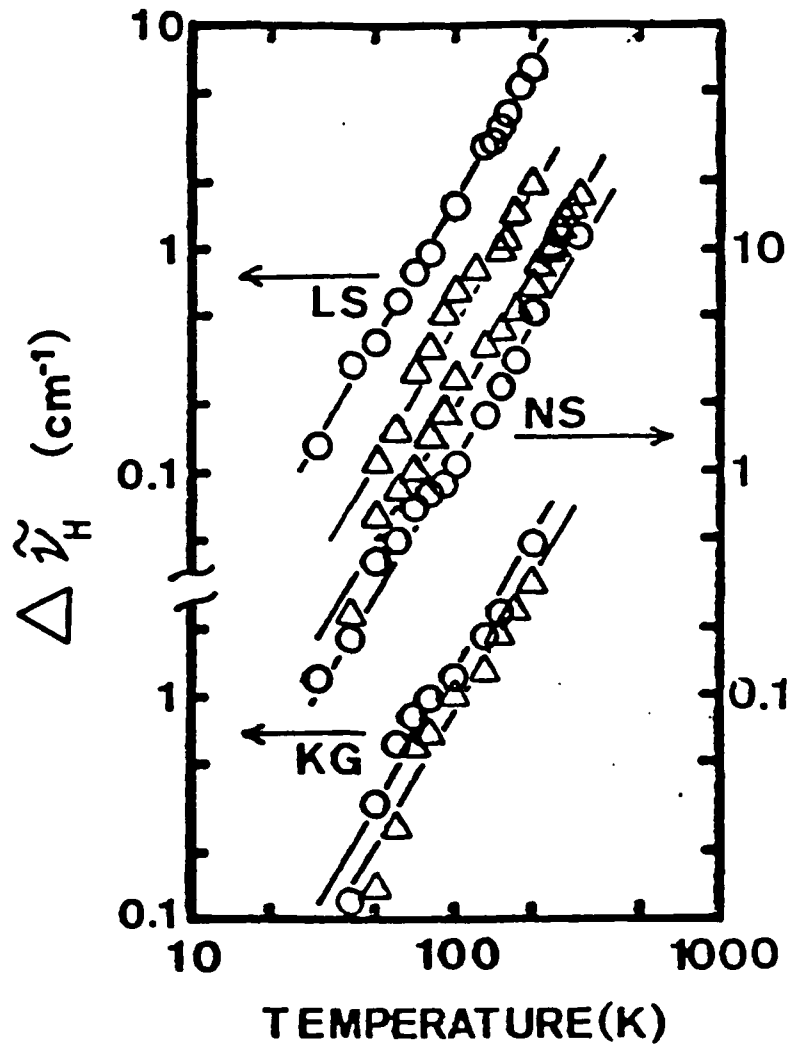


Fig. 3. Temperature dependences of the homogeneous linewidths of the  $^5D_0-^7F_0$  transition of  $\text{Eu}^{3+}$  in LS, NS, and KG glasses excited on the high energy ( $\lambda=577.5$  nm, triangles) and low energy ( $\lambda=580.0$  nm, circles) sides of the inhomogeneously broadened band.

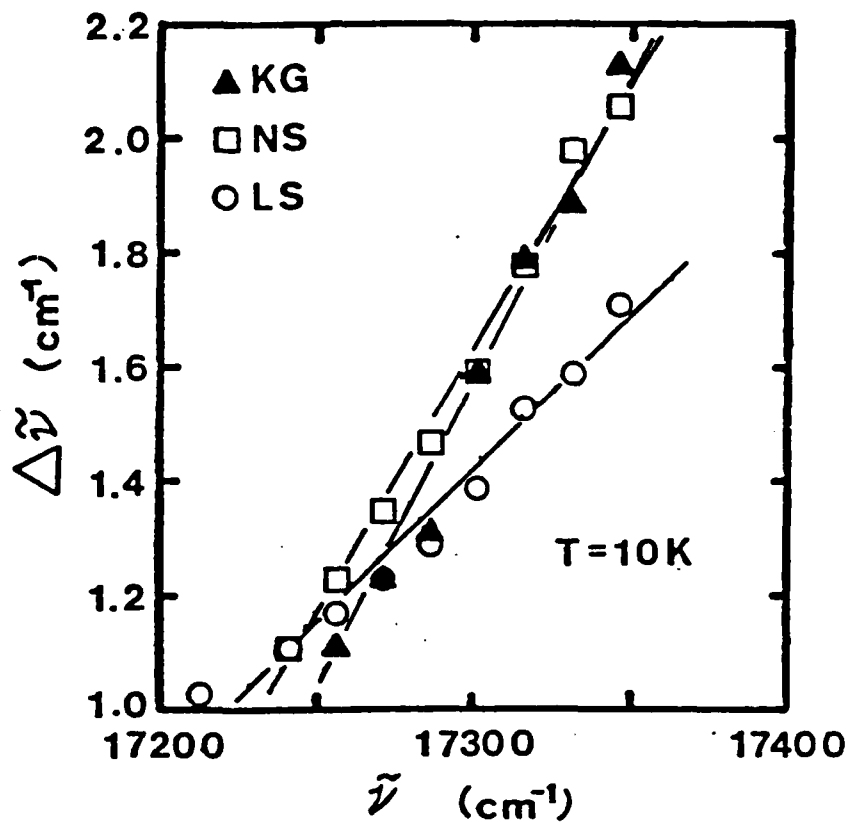


Fig. 4. Residual inhomogeneous broadening of the  $5D_0-7F_0$  transition of  $\text{Eu}^{3+}$  in LS, NS, and KG glass at 10 K as a function of excitation wavenumber across the inhomogeneously broadened band.

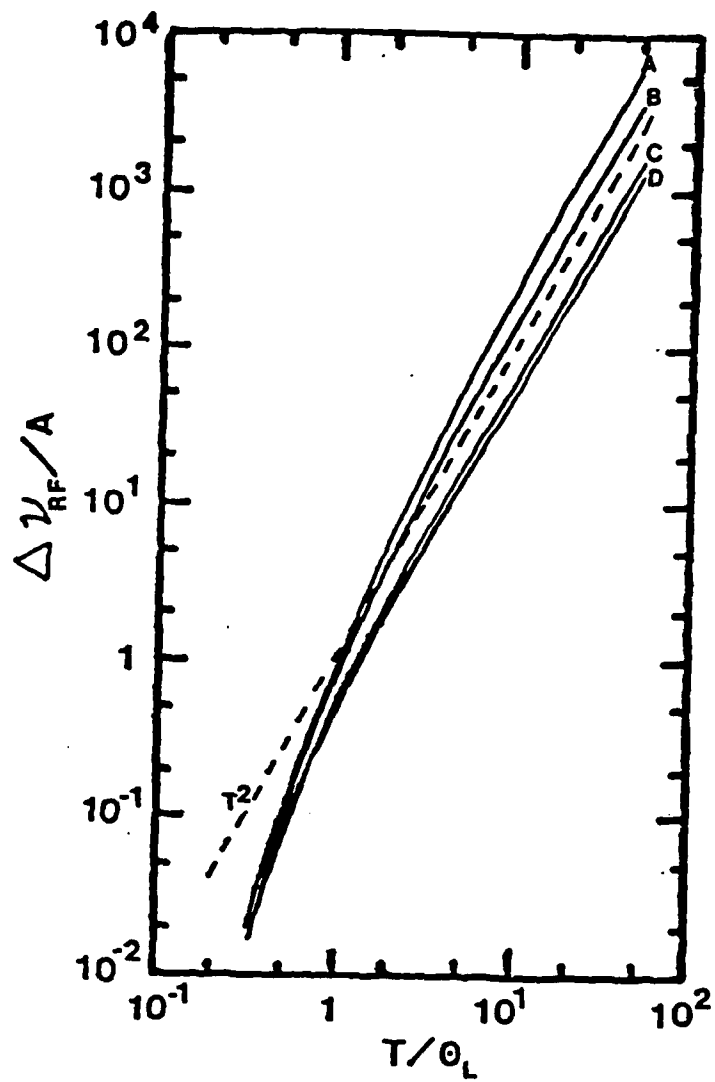


Fig. 5. Temperature dependence of the fraction contribution to the Raman broadening of spectral lines. The curves are numerical evaluations of the linewidth given by the second term in Eq. (5). In curve A:  $\tilde{d}=4/3$ ,  $\bar{d}=3$ ; curve B:  $\tilde{d}=4/3$ ,  $\bar{d}=2.5$ ; curve C:  $\tilde{d}=1$ ,  $\bar{d}=3$ ; curve D:  $\tilde{d}=1$ ,  $\bar{d}=2.5$ . In each case we have taken  $\theta_F \gg T$ . The quadratic dependence shown by the dashed line is included for reference.

#### D. Four-Wave Mixing in Doped Glasses

Four-wave mixing (FWM) processes are currently of significant interest in science and technology due to their importance in modern optics applications such as phase conjugation, and the fact that they provide a powerful spectroscopic tool for probing the properties of the interaction of light and matter. The physical processes underlying the laser-induced gratings that give rise to FWM signals can be placed in two categories according to their decay times after the laser write beams have been turned off. The first category is that of "transient gratings" with fast decay times. This category includes thermal gratings, population gratings, and nonlinear mixing due to the third order susceptibility. The second category is "permanent gratings" which remain for a long time after the laser write beams have been turned off. The most common cause of this type of grating is the photorefractive effect involving ionization of a defect, charge migration and trapping. Permanent gratings are also referred to as "holographic gratings" due to their potential use in holographic information storage applications. We report here the first observation of superimposed transient and holographic gratings leading to a FWM signal with enhanced scattering efficiency and the capability of fast amplitude modulation. These results have been obtained on several different types of  $\text{Eu}^{3+}$ -doped glass samples where the transient signal is associated with a population grating of the  $\text{Eu}^{3+}$  ions and the holographic grating is attributed to local structural modifications.

Seven different types of oxide and fluoride glasses doped with several mole per cent  $\text{Eu}_2\text{O}_3$  were investigated and strong signals were observed in three of these. In this letter, we present some of the results obtained  $\text{EuP}_5\text{O}_{14}$  (EPP) glass. This contains 16.7 mole %  $\text{Eu}_2\text{O}_3$  and its spectroscopic properties have been reported previously.<sup>1</sup>

The experimental setup used to establish and probe population gratings has been described previously.<sup>2</sup> The output of a Spectra Physics cw argon laser operating at 465.8 nm with a total power of 80 mW was split into two beams which were crossed inside the sample to form the gratings. A 2 mW He-Ne laser was used as a probe beam, and the diffracted signal beam was detected by a Hamamatsu R1547 photomultiplier tube after passing through a 0.25-m monochromator to eliminate sample fluorescence. An EG&G/PAR signal averager was used to process the signal before reading it out on a strip chart recorder.

Figure 1 shows the time dependences of the buildup and decay of the FWM signal in  $\text{EuP}_5\text{O}_{14}$  glass at room temperature. The time to reach the maximum FWM signal intensity is of the order of tens of minutes with the exact time depending on the laser power and wavelength. If the laser wavelength is not in resonance with a  $\text{Eu}^{3+}$  absorption transition, no signal is observed under these experimental conditions. This is consistent with the small values of the third order susceptibility tensor components measured by other techniques<sup>3,4</sup> and demonstrates the significant

enhancement of the nonlinear optical properties of the material which can be realized by resonantly pumping a rare earth ion absorption transition. When the write beams are chopped off, the FWM signal decays exponentially with a decay time of 2.6 ms, independent of the grating spacing. This is the same as the fluorescence decay time of 2.7 ms measured for the transitions from the  $^5D_0$  metastable state of  $\text{Eu}^{3+}$  in this sample.<sup>1</sup> However, the signal does not decay back to zero but rather to a constant level representing about seventy per cent of the maximum signal.

The permanent FWM signal remains at the same high level for days. It can be erased by focusing a single laser beam on the same region of the sample. The erasure time is of the order of minutes with the exact time depending on laser power and temperature and independent of write beam crossing angle. As seen in Fig. 1, the time dependence of the permanent signal erasure is highly nonexponential. However, a characteristic decay time equal to the  $e^{-1}$  value for the signal can be defined to describe the speed of the erasure under specific experimental conditions. Figure. 2 shows the variation of the erasure decay rate versus temperature in the range 294 to 345 K. The erasure decay rate decreases exponentially as temperature is raised. This dependence can be described by an expression of the form

$$K \exp[-\Delta E/k_B T] \quad (1)$$

where  $\Delta E$  is the activation energy for the process and  $k_B$  is Boltzmann's constant. The slope of the curve in Fig. 2 gives an activation energy of  $3,720 \text{ cm}^{-1}$  for this case. Furthermore, the intensity of the FWM signal decreases as the temperature is raised above room temperature and the permanent grating can be

thermally erased by heating the sample to about 380 K. The temperature dependence of the scattering efficiency is consistent with a thermal activation energy of about  $2,286 \text{ cm}^{-1}$ .

The signal intensity, expressed in terms of the scattering efficiency of the probe beam  $\eta$ , also varies with the crossing angle of the write beams as shown in Fig. 3. For both the permanent and transient signals, the scattering efficiency is largest at small crossing angles. This is typical behavior for FWM signals with the exact form of the curve depending on the coupling mechanism for the beams.<sup>5</sup> The broken lines in Fig. 3 represent best fits to the data points since the physical mechanism providing the beam coupling in this case is not well enough understood to allow true theoretical predictions to be developed.

The results presented above show that resonant excitation of  $\text{Eu}^{3+}$  ions in this glass host results in a transient population grating of the  $\text{Eu}^{3+}$  ions in the  $^5\text{D}_0$  metastable state and a permanent grating associated with local structural modifications of the glass host. The FWM signal is proportional to the square of the effective electric field induced in the material by the crossed laser beams.<sup>5</sup> This can be expressed as the sum of the induced fields due to the population grating and the host grating,  $E_{\text{eff}} \propto E_{\text{pop}} + E_{\text{host}}$ . Since the first term decays with the fluorescence decay time of the  $^5\text{D}_0$  level,  $\tau$ , and the second term is a constant, the time dependence of the signal when the write beams are chopped off is given by

$$I_{\text{sig}} \propto E_{\text{pop}}^2 e^{-2t/\tau} + 2E_{\text{pop}}E_{\text{host}} e^{-t/\tau} + E_{\text{host}}^2 \quad (2)$$

For this case the first term is much smaller than the last two

and can be neglected. Equation (2) then predicts a signal that decays with the  $\text{Eu}^{3+}$  fluorescence decay time down to a constant value proportional to  $E_{\text{host}}^2$  which is precisely the observed dependence shown in Fig. 1. Note that in the absence of the permanent grating, the signal due to the transient population grating will decay as  $e^{-2t/\tau}$  as observed in other resonantly pumped doped materials.<sup>2,6-8</sup>

One important question concerns the physical mechanism producing the laser-induced modification of the glass host giving rise to the permanent grating. The set of results acquired thus far on the properties of the FWM signal strength and erasure rate for different glass samples, temperatures, and excitation conditions allows us to rule out mechanisms such as photoionization,<sup>9,10</sup> and bond rearrangements associated with trapped exciton effects.<sup>11</sup> The most likely mechanism is thermally induced structural changes. This can be described schematically by the configuration coordinate diagram in Fig. 4. It is assumed that the network forming and modifier ions of the glass host can arrange themselves in two possible configurations in the local environment of the  $\text{Eu}^{3+}$  ions, each configuration resulting in a different local index of refraction for the material. This results in double minima potential wells for the electronic states of the  $\text{Eu}^{3+}$  ions as shown in Fig. 4. Under normal conditions of optical excitation and decay, the ions remain in the configuration represented by the lower energy potential curves. However, in the presence of the sinusoidal intensity pattern created by the crossed laser write beams, a thermal gradient is



generated with the same shape due to the phonons emitted by the  $\text{Eu}^{3+}$  ions after they are optically excited. The low thermal conductivity of the glass allows significant local heating around the  $\text{Eu}^{3+}$  ions which can result in ionic motion to new local configurations. Using the standard expression for heat flow

$$dQ/dt = KA\nabla T \quad (3)$$

estimates of local temperatures of over 1000 K are obtained for typical experimental conditions used here. This can easily result in diffusion of ions to form different local structural configurations. The facts that the refractive index changes are found to occur only when the  $\text{Eu}^{3+}$  are directly excited and when crossed laser beams are used are consistent with the proposed model. Erasure occurs thermally by activation over the potential barrier of about  $2,286 \text{ cm}^{-1}$  in the ground state. Since higher multiplets of the  ${}^7F$  term are located within this energy above the  ${}^7F_0$  ground state, they may play some role in the thermal erasure process. Erasure with a laser beam occurs through uniform heating which allows the ions to return to their original distribution. The activation potential barrier for this is  $3,720 \text{ cm}^{-1}$  in the excited state and the process can be thermally enhanced by raising the temperature. This energy barrier is large enough that  ${}^5D_1$  levels may take part in the spectral dynamics of the optical erasure process.

The mechanism described above provides one viable explanation of the data presently available on laser-induced holographic gratings in doped glasses. In order to verify this model and extend our knowledge of the details of physical processes taking place, further investigations must be made on a wider variety of

types of glass hosts and doping ions. It is interesting to note that out of the set of  $\text{Eu}^{3+}$ -doped glasses categorized previously in terms of their spectral structure,<sup>1</sup> only those exhibiting the smallest amount of spectral structure (i.e., greatest amount of local disorder) produce a strong holographic grating signal.

This observation of the superposition of transient and holographic gratings in doped glasses is important for several reasons: it represents the first observation of a new mechanism for producing a FWM signal in a solid; it demonstrates a new experimental technique for investigating local structural properties of glasses; and it shows that doped glasses may be useful in applications based on FWM such as phase conjugation, beam switching, or optical storage. The technological applications are especially interesting because of the use of a holographic "carrier" grating that can be amplitude modulated by a fast transient grating.

## REFERENCES

1. X. Gang and R.C. Powell, J. Appl. Phys. 57 1299 (1985).
2. J.K. Tyminski, R.C. Powell, and W.K. Zwicker, Phys. Rev. B 29 6074 (1984).
3. M.J. Weber, D. Milam, and W.L. Smith, Opt. Eng. 17, 463 (1978); M.J. Weber, C.F. Cline, W.L. Smith, D. Milam, D. Heiman, and R.W. Hellwarth, Appl. Phys. Lett. 32 403 (1978).
4. I. Thomazeau, J. Etchepare, G. Grillon, and A. Migus, Opt. Lett. 10, 223 (1985).
5. J. Feinberg, in "Optical Phase Conjugation", edited by R.A. Fisher (Academic, New York, 1983), p. 417.
6. A.M. Ghazzawi, J.K. Tyminski, R.C. Powell, and J.C. Walling, Phys. Rev. B 30, 7182 (1984).
7. P.F. Liao, L.M. Humphrey, D.M. Bloom, and S. Gewschwind, Phys. Rev. B 20, 4145 (1979); P.F. Liao and D. M. Bloom, Opt. Lett. 3, 4 (1978).
8. H.J. Eichler, J. Eichler, J. Knof, and Ch. Noack, Phys. Status Solidi A 52, 481 (1979).
9. A. Winnacker, R.M. Shelby, and R.M. Macfarlane, Opt. Lett. 10, 350 (1985).
10. P. Gunter, Phys. Rep. 92, 199 (1982).
11. R.A. Street, Solid State Commun. 24, 363 (1977).

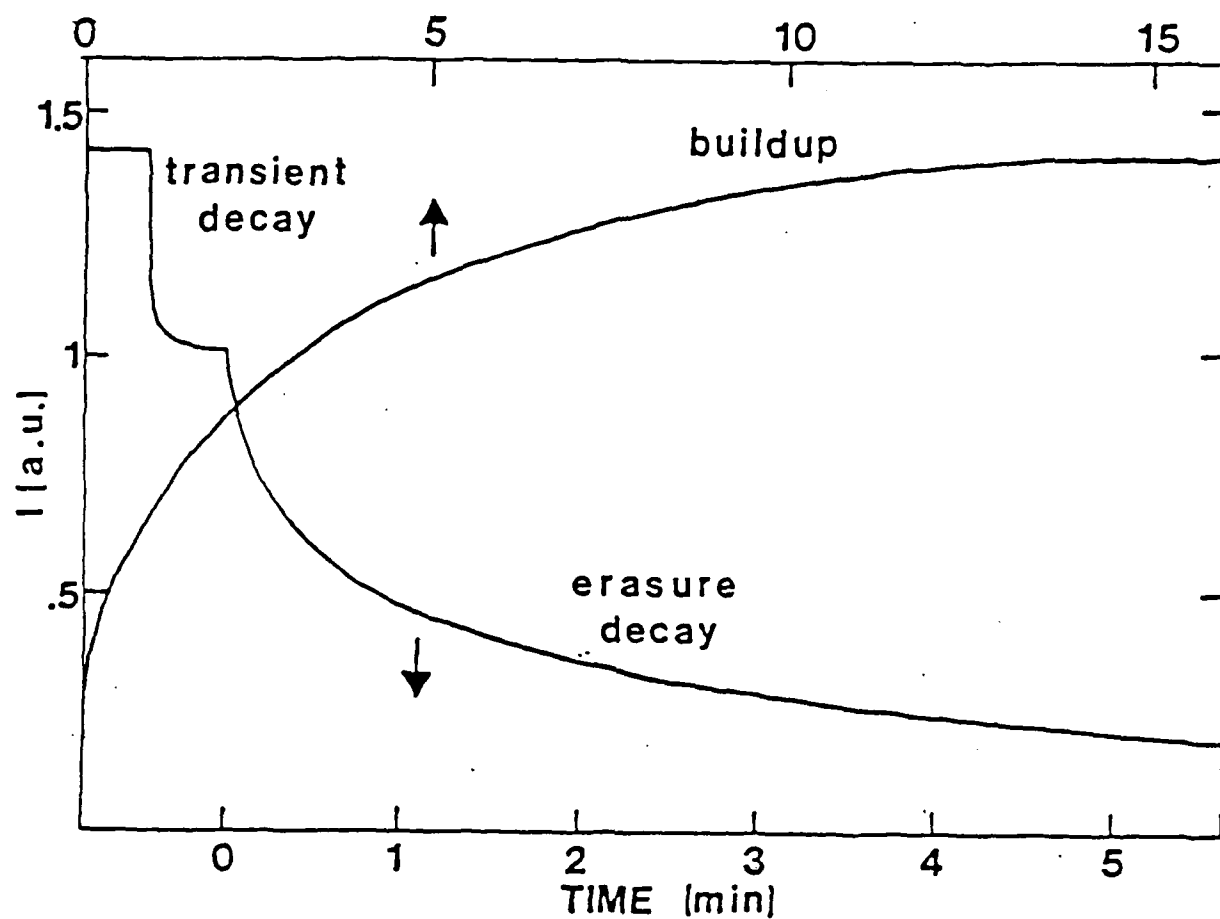


FIG. 1. Time dependences of the buildup, transient decay, and erasure of FWM signals in EPP glass at 300 K. The total power of the laser write beams is 80 mW and the erase beam power is 40 mW.

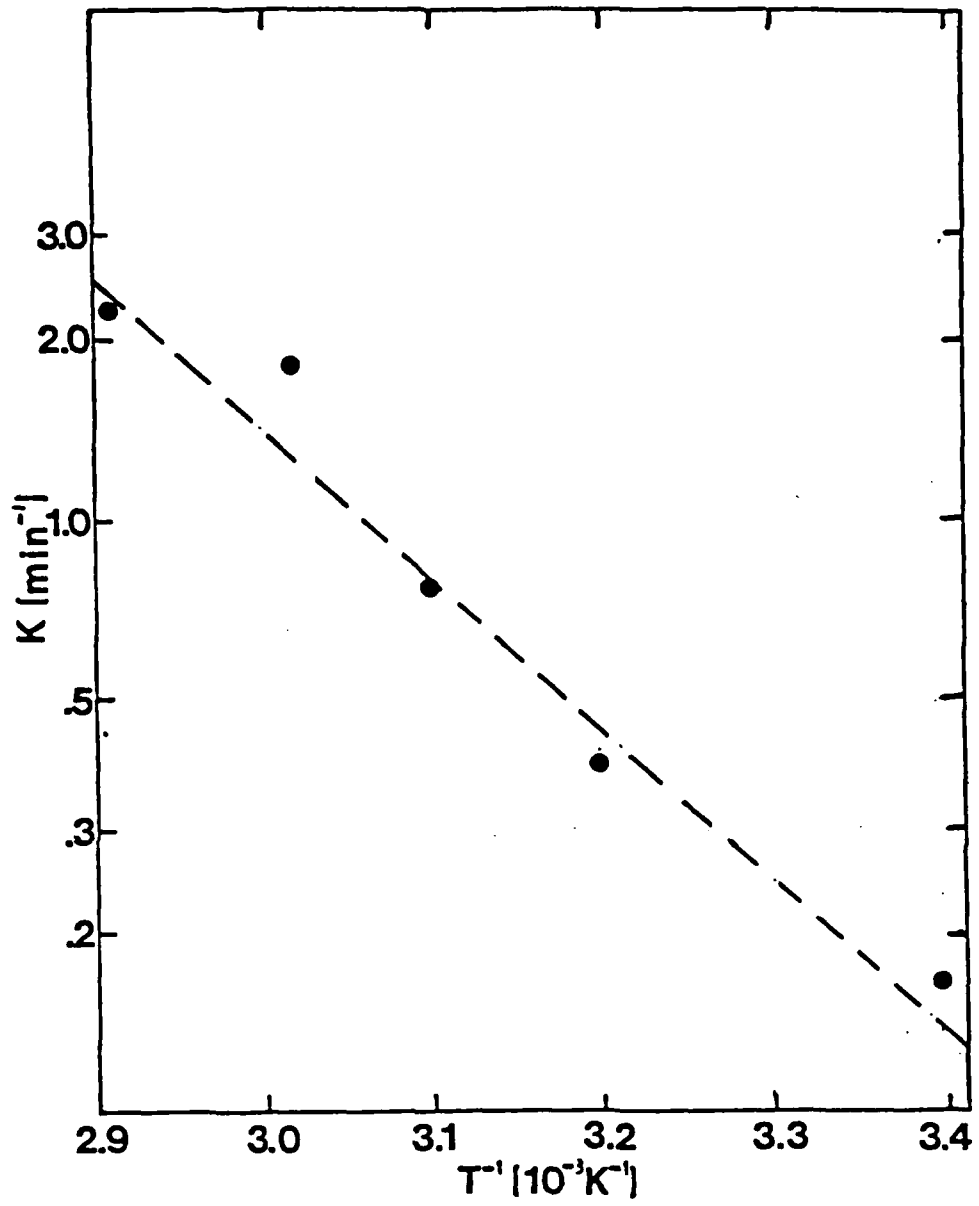


Fig. 2. Temperature dependence of the holographic grating erasure decay rate in EPP for an erase beam power of 40 mW.

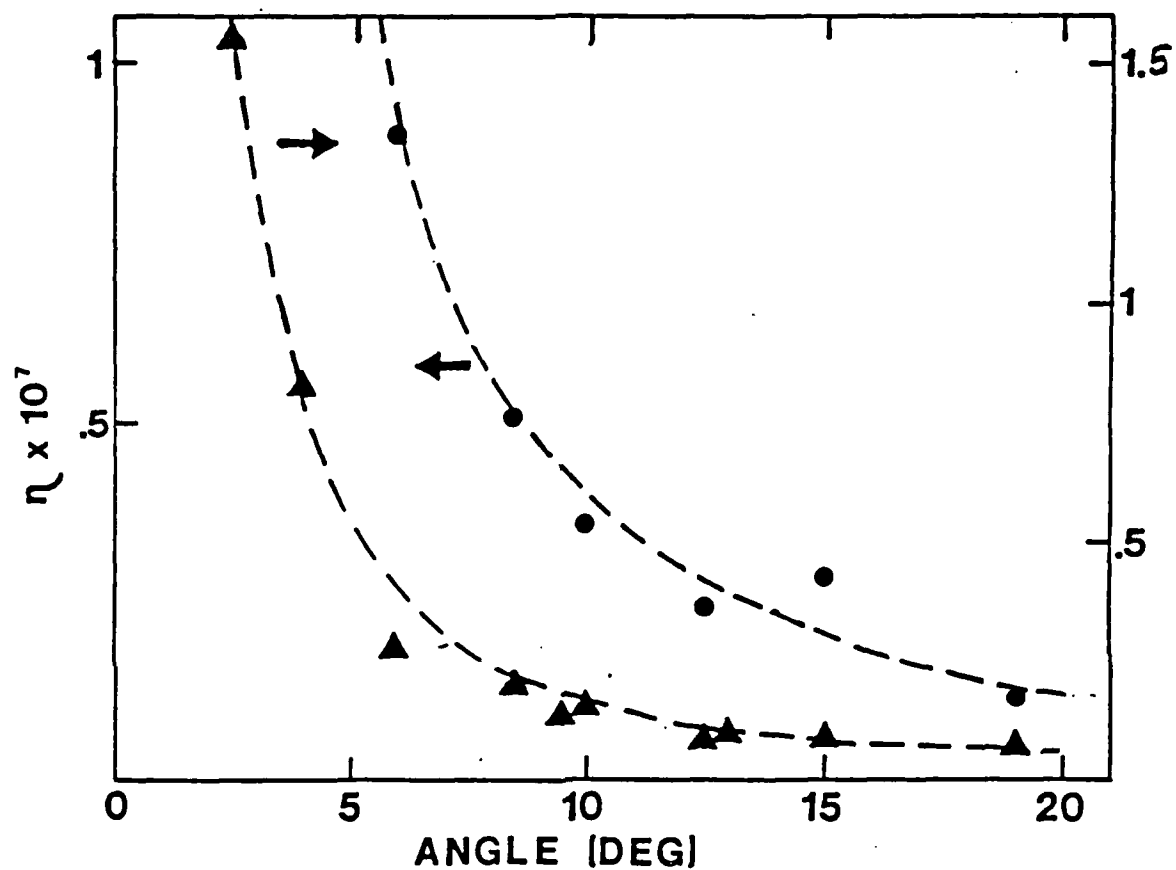


Fig. 3. Dependence of the FWM scattering efficiency for EPP on the crossing angle of the write beams at 300 K. The triangles represent the scattering efficiency from the holographic grating while the circles represent the scattering efficiency from the transient grating.

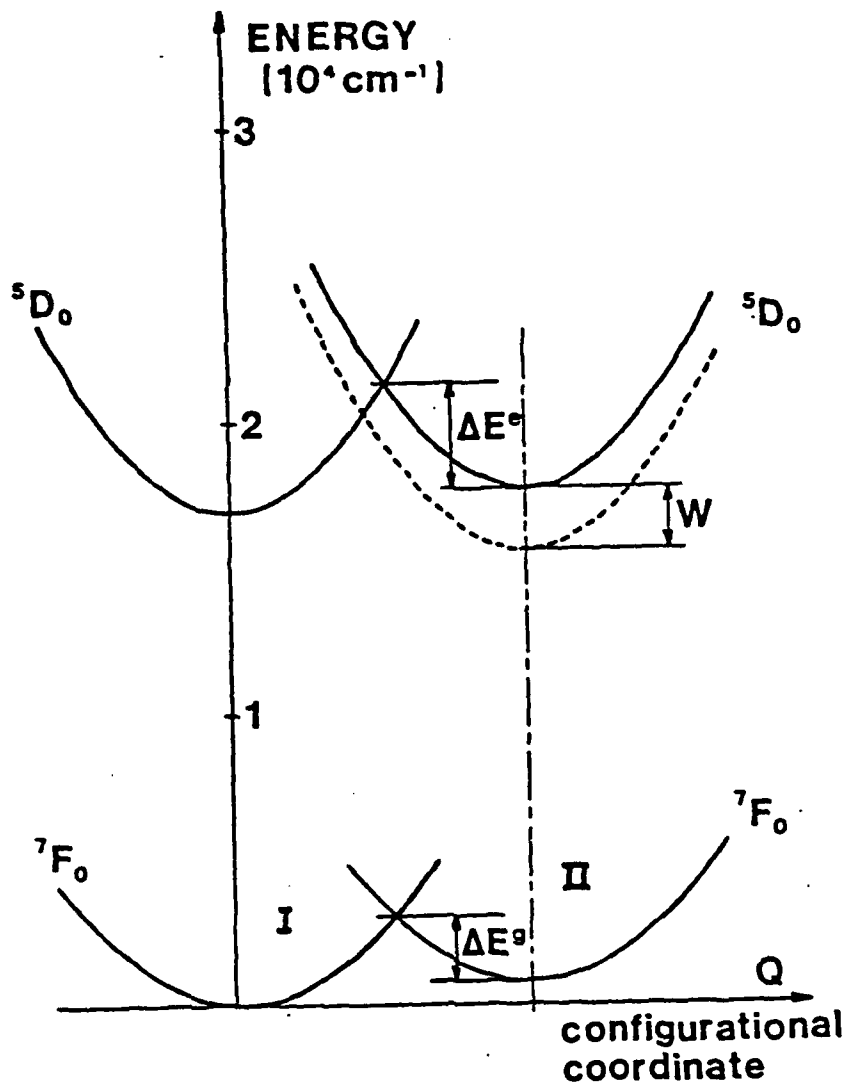


Fig. 4. Configuration coordinate diagram for  $\text{Eu}^{3+}$  energy levels in EPP glass with two possible local configurations. The broken curve represents the stabilization effect of the radiation pressure force on the dipole created by the excited  $\text{Eu}^{3+}$  ion.



*MISSION  
of  
Rome Air Development Center*

RADC plans and executes research, development, test and selected acquisition programs in support of Command, Control, Communications and Intelligence (C<sup>3</sup>I) activities. Technical and engineering support within areas of competence is provided to ESD Program Offices (POs) and other ESD elements to perform effective acquisition of C<sup>3</sup>I systems. The areas of technical competence include communications, command and control, battle management, information processing, surveillance sensors, intelligence data collection and handling, solid state sciences, electromagnetics, and propagation, and electronic, maintainability, and compatibility.



END

10-87

DTIC